1-1-2012

Predicting Vision Loss In Healthy Aging With Manganese-Enhanced Mri Of The Rat Eye

David Bissig
Wayne State University,

PREDICTING VISION LOSS IN HEALTHY AGING WITH MANGANESE-ENHANCED MRI OF THE RAT EYE

by

DAVID BISSIG

DISSERTATION

Submitted to the Graduate School

of Wayne State University,

Detroit, Michigan

in partial fulfillment of the requirements

for the degree of

DOCTOR OF PHILOSOPHY

2014

MAJOR: ANATOMY AND CELL BIOLOGY

Approved by:

_____

Advisor Date

_____

_____

_____

ACKNOWLEDGEMENTS

First, I'd like to thank my advisor, Dr. Bruce Berkowitz, for his exemplary mentorship. This work would not have been possible without his patient guidance, and gift for communicating his accumulated knowledge to his students. I thank Robin Roberts for her help collecting MRI data, caring for our animals, keeping the lab running, and teaching me enough of those skills to complete this work. I would also like to thank my committee members, Dr. Cindy Lustig, Dr. Paul Walker, and Dr. Dennis Goebel, for their guidance and support. Special thanks go to Cindy, who first got me interested in aging research, and Dennis, who generously donated his time and expertise towards collecting the Western blot data featured in this work.

Many others members of Wayne State University deserve recognition: I'm grateful for the support of both Wayne State's MD/PhD program, headed by Dr. Ambika Mathur, and the Anatomy and Cell Biology Department, chaired by Dr. Linda Hazlett. I've received excellent instruction from the Anatomy and Cell Biology faculty during my time here, including the first year of medical school, and have had the pleasure of publishing manuscripts with Dr. Rodney Braun, Dr. Avril Genene Holt, Dr. Zhuo-Hua Pan, and the staff and scientists associated with each.

TABLE OF CONTENTS

LIST OF TABLES

LIST OF FIGURES

CHAPTER 1

INTRODUCTION

In humans, visual function diminishes throughout healthy aging, with roughly linear declines in contrast sensitivity and best-corrected visual acuity beginning in young adulthood (<30 yrs; Owsely et al., 1983; Elliott et al., 1995; Rubin et al., 1997). In old age, these vision declines are linked to impairments in activities of daily living, memory declines, and increases in depressive symptoms (Anstey et al., 2001; Carabellese et al., 1993). Age-related vision loss is also associated with the choice to cease driving (Freeman et al., 2005), which itself results in decreased participation in out-of-the-house activities and increases in depressive symptoms (Marottoli et al., 2000; Ragland et al., 2005). In health care settings, poor visual acuity increases elderly patients' likelihood of developing delirium (Inouye, 2000). For these reasons, substantial improvements in quality of life would be expected from an intervention against vision loss in healthy aging. Any such intervention would be based on knowledge of the anatomical and physiological contributions to vision loss in healthy aging, which remain poorly understood. The association between aging and several diseases of the visual system — including glaucoma, diabetic retinopathy, and age-related macular degeneration — offers another incentive for studying normal aging: Identifying the physiological changes that predict and explain normal vision decline may help clarify how aging increases the risk of disease.

Concurrent with vision loss in healthy aging, the retinas of healthy aging humans undergo several anatomical and physiological changes: Declines in dark-adaptation rates (Jackson et al., 1999) and electroretinogram (ERG) a-wave amplitude, with associated increases in a-wave latency (Wright et al., 1985; Freund et al., 2011), begin in young adulthood and continue through old age. Decreases in retinal neuron density and retinal thickness follow a similar time-course

(Alamouti & Funk, 2003; Curcio et al., 1993; Harman et al., 2000), though total neuron numbers may be reasonably well-preserved: Retinal surface area increases with age (Harman et al., 2000) — an effect which would decrease thickness and neuron density merely through isovolumic 'stretching' of the retina — consistent with continued modest growth of the eye and optical components throughout adulthood (Atchison et al., 2008; Kasthurirangan et al., 2008). At present, it is unknown which if any of these progressive retinal changes contribute to the similarly-progressive vision declines in healthy aging: As reviewed by Spear (1993), documented anatomical and electrophysiological changes seem too modest, relative to inter-individual differences at any given age, to fully account for the age-related vision declines.

Longitudinal studies could clarify the anatomical and physiological links to vision declines: testing, for instance, whether the rate of a given change in retinal morphology is well-correlated with the rate of vision decline. Animal models of human aging are attractive for such studies. Given their shorter lifespans, age-related vision declines are measurable over months instead of decades. Normal aging in pigmented rats has the same features as found for humans: Declines in dark-adaptation rates (Bankson et al., 1989), declines in ERG a-wave amplitude, and increased a-wave latency (Charng et al., 2011) have been demonstrated. As in humans, retinal thickness and neuron density decrease throughout adulthood (Katz & Robison, 1986; Obin et al., 2000; Feng et al., 2007; Bissig & Berkowitz, 2011), but retinal surface area increases (Mansour et al., 2008; Harman et al., 2003; Bissig & Berkowitz, 2011), making neuron loss with advancing age uncertain (Katz & Robison, 1986; Obin et al., 2000; Harman et al., 2003; Feng et al., 2007). To our knowledge, behavioral testing has not been used to document vision declines in normal aging pigmented rats, and this is one goal of the present work. However, vision declines

consistent with those noted in pigmented mice (van Alphen et al., 2009; Kolesnikov et al., 2010) and albino rats (Linder & Gribkoff, 1991; Krauter et al., 1981) are expected.

The uncertain link between age-related vision declines and previously-documented anatomical and physiological changes at the retina (Spear, 1993) has prompted us to reevaluate the aging visual system using newer measures of retinal physiology. In the present studies, we use Mn^{2+}-enhanced MRI (MEMRI) to longitudinally and non-invasively monitor a sensitive and accurate metric of retinal physiology: calcium ion influx in light and dark-adapted eyes. In MEMRI, animals are injected with a non-toxic dose of Mn^{2+}, a Ca^{2+} surrogate which accumulates in neurons over a period of a few hours, while animals are awake and free-moving. Later, the extent of retinal Mn^{2+} uptake is measured by the manganese concentration-dependent alterations of MRI signals (Chuang et al., 2009). Because Mn^{2+} efflux is slow, taking days for the retina (Tofts et al., 2010), uptake measured a few hours after injection is a useful measure of neuronal Mn^{2+} influx. Similar to Ca^{2+}, Mn^{2+} enters neurons through L-type voltage gated calcium channels ('L-VGCC's): *In vitro*, Mn^{2+} uptake is strongly inhibited by L-VGCC blockers, and increased both by membrane depolarization (thereby opening L-VGCCs) and application of the L-VGCC agonist BayK8644 (Drapeau & Nachshen, 1984; Carlson et al., 1994). *In vivo* studies confirm that neuronal Mn^{2+} uptake is inhibited by the specific L-VGCC antagonists verapamil (Cross et al., 2007), nifedipine (Berkowitz et al., 2011), and D-*cis*-diltiazem (i.e. the (+)-*cis* isomer; Berkowitz et al., 2007b). Based on similarities between Ca^{2+} and Mn^{2+} physiology, one would predict that Mn^{2+} uptake is activity-dependent. To-date, several studies have confirmed this prediction, using MEMRI to non-invasively study neuronal activity in the rodent retina (see below) and brain (e.g. Bissig & Berkowitz, 2009; Bissig & Berkowitz, 2011; Yu et al., 2005; Eschenko et al., 2010a, Lin & Koretsky, 1997), where MEMRI demonstrates good agreement

with other measures of activity: c-Fos (Morita et al., 2002), blood oxygen level-dependent (BOLD) fMRI, and cerebral blood flow (Duong et al., 2000)(see Silva, 2012 for a recent review).

L-VGCCs, found throughout the rat retina (Ahlijanian et al., 1990; Kamphuis & Hendriksen, 1998; Nachman-Clewner et al., 1999; Morgans et al., 2001; Xu et al., 2002), contribute substantially to neuronal Ca^{2+} influx: In freshly-dissected rat retina, L-VGCCs account for roughly half of NMDA-induced Ca^{2+} influx (Melena & Osborne, 2001), while cell-specific studies show substantial inhibition of Ca^{2+} currents by L-VGCC blockers in rat bipolar cells (Pan & Lipton, 1995; Protti & Llano, 1998) and rod photoreceptors (Koulen et al., 1999). *In vivo*, we have previously monitored retinal ion influx through these channels with MEMRI: The expected pattern of activity-dependent retinal Mn^{2+} influx — low in photoreceptors exposed to light, when membranes are hyperpolarized and L-VGCCs closed, but high in darkness, when photoreceptors are fully depolarized (for review, see Yau, 1994) — has been confirmed *in vivo* using MEMRI of the rat retina (Berkowitz et al., 2006; Berkowitz et al., 2009; Tofts et al., 2010; Bissig & Berkowitz, 2011). Moreover, Mn^{2+} influx at both the inner retina (bipolar and other cells) and outer retina (photoreceptors) is inhibited by L-VGCC blockers (Berkowitz et al., 2007b; Berkowitz et al., 2011).

Ion influx through photoreceptor L-VGCCs is critical to normal retinal function: In *Xenopus*, glutamate release by photoreceptors is halted by L-VGCC blockade (Schmitz & Witkovsky, 1997). Mutant mice with altered L-VGCC expression demonstrate diminished post-photoreceptor responses to light, as well as irregular synapses between photoreceptors and bipolar cells (Chang et al., 2006), consistent with L-VGCC mediation of photoreceptor axonal growth and remodeling (Nachman-Clewner et al., 1999). If ion influx through retinal L-VGCCs changes with age, it could result in diminished retinal function: In the short-term, L-VGCC-

triggered neurotransmitter release may be compromised. Longer-term functional changes may arise if axonal growth and remodeling are compromised. For instance, as retinal surface area increases, the average distance between neighboring neurons will tend to increase, and it's likely that some remodeling is needed to maintain connectivity over greater distances.

In the brain, neuronal Ca^{2+} influx through L-VGCCs increases throughout adulthood, and is well-correlated with impaired synaptic plasticity and cognitive function (Campbell et al., 1996; Thibault & Landfield; 1996; Karst et al., 1997; Norris et al., 1998; Thibault et al., 2001; Tombaugh et al. 2005; see Thibault et al., 1998 and Foster, 2007 for reviews). However, reports addressing the possibility that the same age-related change occurs in retinal neurons are sparse: In a previous MEMRI study, we found greater retinal Mn^{2+} uptake in mid-adult than in young-adult mice (Calkins et al., 2008), and age-related increases in Ca^{2+} influx through Müller glial L-VGCCs have been documented in humans (Bringmann et al., 2000). Acute L-VGCC blockade improves contrast sensitivity in healthy adult humans (in 54-78 yr olds from Bose et al., 1995; in 21-49 yr olds from Boehm et al., 2003) — suggesting that high ion flux through L-VGCCs can somehow diminish vision — but it is not known whether this effect is age-dependent.

Based on the above considerations, we *hypothesized* that ion influx through L-VGCCs increases with age in the rat retina, and that high influx would be correlated with age-related declines in visual function. To test this hypothesis, we longitudinally measured visual performance in two groups of rats: In one cohort, rats were studied first as *Y*oung adults (aged ~2.5 mo), then again in *M*id-adulthood (~7 mo) (Group 'YM'). Rats in the second cohort were studied first as *M*id-adults, at an intermediate time point (~11.5 mo), and then again as *O*ld adults (~19 mo) (Group 'MO'). At each time point, two aspects of visual function — spatial frequency threshold ('SFT'; a proxy for visual acuity) and contrast sensitivity ('CS') — were measured

behaviorally using optokinetic tracking (OKT), a vision-dependent reflex which requires no animal training. In adult rats, OKT is stable when repeatedly measured over short periods of time (i.e., no practice effects) and is independent of visual cortex (Douglas et al., 2005; Prusky et al., 2008). Unlike other methods of quantifying vision, such as the visual water task (Prusky et al., 2000), OKT carries little risk of confounding age-related impairments in thermoregulatory and visual function (Linder & Gribkoff, 1991). In both groups, the first and final vision tests were followed by Mn^{2+}-enhanced MRI (MEMRI): Using an eye patch to keep one eye dark-adapted while the other was exposed to normal lab lighting, we tested for longitudinal changes in retinal ion influx in both lighting conditions. From the same MR images, we quantified longitudinal changes in eye morphology; both of the retina and of optical components like the lens.

In that first arm ('Arm 1') of the present study, we documented that retinal Mn^{2+} uptake increases with age. We also found that the relatively high Mn^{2+} uptake at the start of the study predicted the rate of subsequent vision declines. Since neuronal Mn^{2+} influx/uptake is inhibited by L-VGCC blockers (Drapeau & Nachshen, 1984; Carlson et al., 1994; Cross et al., 2007; Berkowitz et al., 2011; Berkowitz et al., 2007b), we considered eventually using such drugs for an intervention study of age-related vision loss. Arm 2 experiments were conducted in anticipation of such studies, to better-understand the role of L-VGCCs in Mn^{2+} uptake. In the first experiment of Arm 2, we compared L-VGCC involvement in dark- versus light-adapted outer retinal Mn^{2+} uptake. Young adult rats had one eye patched (to maintain dark-adaptation), and were studied with MEMRI after injection of the L-VGCC blocker nifedipine. Nifedipine-injected rats were compared to a set of similarly-treated vehicle-injected controls. In the second experiment of Arm 2, we tested whether inhibition of Mn^{2+} uptake by L-VGCC blockade is independent of systemic effects. To our knowledge, this has not yet been tested *in vivo*, though

positive results were expected based on previous *in vitro* studies (Drapeau & Nachshen, 1984; Carlson et al., 1994). Using dark-adapted young adult rats, we compared Mn^{2+} uptake in eyes exposed to nifedipine eye drops to Mn^{2+} uptake in the contralateral eyes, which were exposed only to the vehicle used to prepare the nifedipine eye drops.

Our investigations of age-related changes in retinal Mn^{2+} uptake were guided, in part, by previous studies of Ca^{2+} homeostasis in the rat hippocampus. At the hippocampus, age-related increases in Ca^{2+} influx have been linked to increased neuronal expression of some L-VGCC isoforms: Expression of the α_{1D} isoform ($Ca_v1.3$) is greater in older rats, but expression of the α_{1C} ($Ca_v1.2$) isoform appears unaffected by age (Veng & Browning, 2002; Veng et al., 2003). Importantly, α_{1D} is roughly an order of magnitude less-sensitive to blockade than α_{1C} (Xu & Lipscombe, 2001; Koschak et al., 2001; Tarabova et al., 2007). Substantial age-related and isoform-specific changes could therefore result in an age-related loss in sensitivity to L-VGCC blockade, complicating any pharmacological intervention in the aging process. In Arm 3, we therefore tested for an age-related loss in sensitivity to L-VGCC blockade — a potential indicator for isoform-specific changes in L-VGCC expression — using MEMRI. In a previous study of young adult rats, we found progressively lower Mn^{2+} influx in the presence of progressively higher doses of the L-VGCC blocker diltiazem (Berkowitz et al., 2007a). Based on that experience, we collected dose-response curves for that drug in both young and mid- adult rats. In a follow-up experiment, we used Western blots to compare retinal α_{1C} and α_{1D} expression over a similar age range.

CHAPTER 2

ARM 1: LONGITUDINAL STUDIES OF VISUAL PERFORMANCE AND ASSOCIATED FACTORS

2.1 Rationale

In this Arm, visual function (CS, SFT) and retinal ion physiology (MEMRI) data were collected (unless otherwise mentioned) in two groups: Group *YM* rats (studied as *Y*oung adults (age ~2.5 mo) and *M*id-adults (age ~ 7 mo)), and Group *MO* rats (studied as *M*id-adults (age ~7 mo), mid-to-older adults (age ~11.5 mo, only visual function), and *O*lder adults (age ~19 mo). Mn^{2+}-enhanced images were also used to measure age-related changes in morphology of both the retina and optical components (e.g. lens). Follow-up analyses used regression to test, for instance, whether retinal Mn^{2+} uptake predicts later declines in vision (CS, SFT).

2.2 Methods

Male Long-Evans rats (Hilltop Labs; Scottdale, PA) were studied in all arms of the present work. We detail the ages, weights, and quantities of rats used in each experimental arm below. Rats were given food and water *ad libitum* and housed and maintained in normal 12 hr light/12 hr dark cycling. All procedures were in accordance with the NIH Guide for the Care and Use of Laboratory Animals and the ARVO Statement on Animals in Vision research.

2.2.1 Missing and Excluded Data: The need for high-quality MRI data from both eyes — one being light-exposed, the other dark-adapted (i.e., patched; see below) — of each rat at each time point lead to several cases of missing or excluded data: Rats do not recover from our usual anesthetic of choice (urethane; see other Arms) and so this anesthetic was inappropriate for the present longitudinal design. Instead, we opted for a mixture of ketamine and xylazine, despite some difficulty in maintaining the depth of anesthesia needed during the ~2 hr of high-resolution MRI scanning of the eye.

We summarize different sources of missing and excluded data while keeping a running tally of the remaining subjects between <>'s in the following format: <number of subjects for visual performance & for MEMRI at ~7 mo, for visual performance at ~11.5mo, for visual performance & for MEMRI at ~19 mo>. We started with a total of 42 rats in Group MO, and in the hypothetical case that no subjects were excluded or lost to follow up, each would have contributed to all measurements <42&42,42,42&42>. Due, for instance, to animal death during scans or hardware problems, high-quality MEMRI data could not be obtained from seven rats at ~7 mo and one rat at ~19 mo <42&35,35,35&34>. In addition, three rats were removed from this group and used to collect baseline data (i.e., without Mn^{2+}; see below) at the old adult time point <42&35,35,35&31>. We then screened for univariate outliers ($|z|>3.3$) at each time point. Three animals had unusually thick retinas (suggestive of edema or other pathology) as mid-adults, but only in one eye: In those three rats, the absolute value of the left-right thickness difference was (mean±SEM) 71.8±7.1μm, versus 9.0±7.9μm in the other rats. It is unlikely that this asymmetry was related, for instance, to the eye patch or duration of anesthesia: The thicker retina was in the unpatched eye in one of the three cases, and the first eye scanned in two of three cases. Behavioral and MRI data from those three rats was excluded <39&32,32,32&28>. Twelve rats failed to recover normal health after being anesthetized for their first MRI scan (seven died within two days) and thus were unavailable for longitudinal study <39&32,20,20&16>. After fully recovering from the first scan, one animal died (42 d post MRI) before the follow-up vision testing at age ~11.5 mo. After the ~11.5 mo time point, another four rats died or were euthanized due to declining health <39&32,19,15&11>. Note that the three Group MO rats used, as old adults, for baseline (no Mn^{2+}) measurements still provided useful structural data from both eyes. As such, longitudinal changes in retinal thickness (for instance) are measured in fourteen Group

MO rats, though longitudinal changes in Mn^{2+} uptake are only measured in eleven of those fourteen rats. Demographics (age, weight) of the remaining rats are given in the next section.

Starting with 22 rats in Group YM, we summarize subject loss while keeping a running tally of remaining subjects <number of subjects for visual performance & for MEMRI at ~2.5 mo, for visual performance & for MEMRI at ~7 mo>: High-quality MEMRI data could not be obtained from three rats at the young adult time-point, and two rats at the mid-adult time point <22&19,19&17>. As in Group MO, one rat had unilaterally thickened retina and was excluded from all analyses <21&18,18&16>. Five rats failed to recover normal health (four died within two days) after the first time point, and were not available for longitudinal study <21&18,13&11>.

2.2.2 Animals: We analyzed data from twenty-one Group YM rats (mean(SD) initial age of 73(9) d; weighing 290(70) g). Thirteen of these were available for follow-up in mid-adulthood (227(7) d; 502(34) g). We analyzed data from thirty-nine Group MO animals (initial age of 206(10) d; 439(50) g). Roughly half of these rats were available at the intermediate time point 144(13) d later, when only visual function and body weight was measured (n=19; 350(15) d; 580(50)g). Fifteen of those contributed data to the old adult time point (228(21) d after the intermediate time point; age 580(29) d; 605(67)g).

2.2.3 Visual Function: Spatial frequency threshold ('SFT'; a proxy for visual acuity) and contrast sensitivity ('CS') were measured using an optokinetic tracking ('OKT') device built in-house. As illustrated in Figure 1, three identical 19" LCD monitors (I-Inc model #iX-191APB) facing the inside of the device were arranged in an equilateral triangle and fastened to a wooden frame. Mirrors fastened to the floor and ceiling of the device reflected a moving sine wave grating (black and white, or light and dark grey, stripes) shown identically on each screen

through use of a PCI 8-port VGA video splitter (model #PCI815V). The sine wave grating was displayed and distorted with VisionEgg (v.1.0) so as to form a virtual barrel (i.e., the width of one light/dark/light cycle appearing similar in all directions) when viewed from the center of the device. This device configuration resembles van Alphen et al. (2009)'s design. In the present study, however, each rat was placed on an elevated perch in the center of the triangle, and positioned such that its head was roughly centered in the device. Rats had unrestricted head movement during each of the eight 15-20 min sessions (1-2 per day) used to measure SFT (4 of the 8 sessions) and CS at a given age. Rats typically remained on the perch for several minutes, and were gently placed back on the perch when they stepped off. Visual performance was recorded while the rat remained on the perch and while the tracking eye (left if the virtual barrel rotated clockwise, right if counterclockwise, when viewed from above) was within the arena denoted by Figure 1C. A camera (Microsoft LifeCam VX-2000) aimed through a hole in the center of the ceiling mirror provided a continuous video feed, allowing the experimenter to monitor tracking behavior.

Unlike the commercial system developed by Douglas, Prusky, and colleagues (Douglas et al., 2005; Prusky et al., 2008; 'OptoMotry'), but similar to other devices (e.g. Thomas et al., 2010), the grating's spatial frequency was not dynamically adjusted to account for the changes in distance between the rat's eye and the screens, which occur during free movement of the head. We therefore describe spatial frequency settings in terms of cycles per barrel degree (c/bd) such that a (40/360°=) 0.111 c/bd setting means that the three screens, together, generated a 360° virtual barrel with 40 cycles. The position-dependent relationship between these c/bd values and subjective cycles per degree visual angle is shown for two eye positions in Figure 1D.

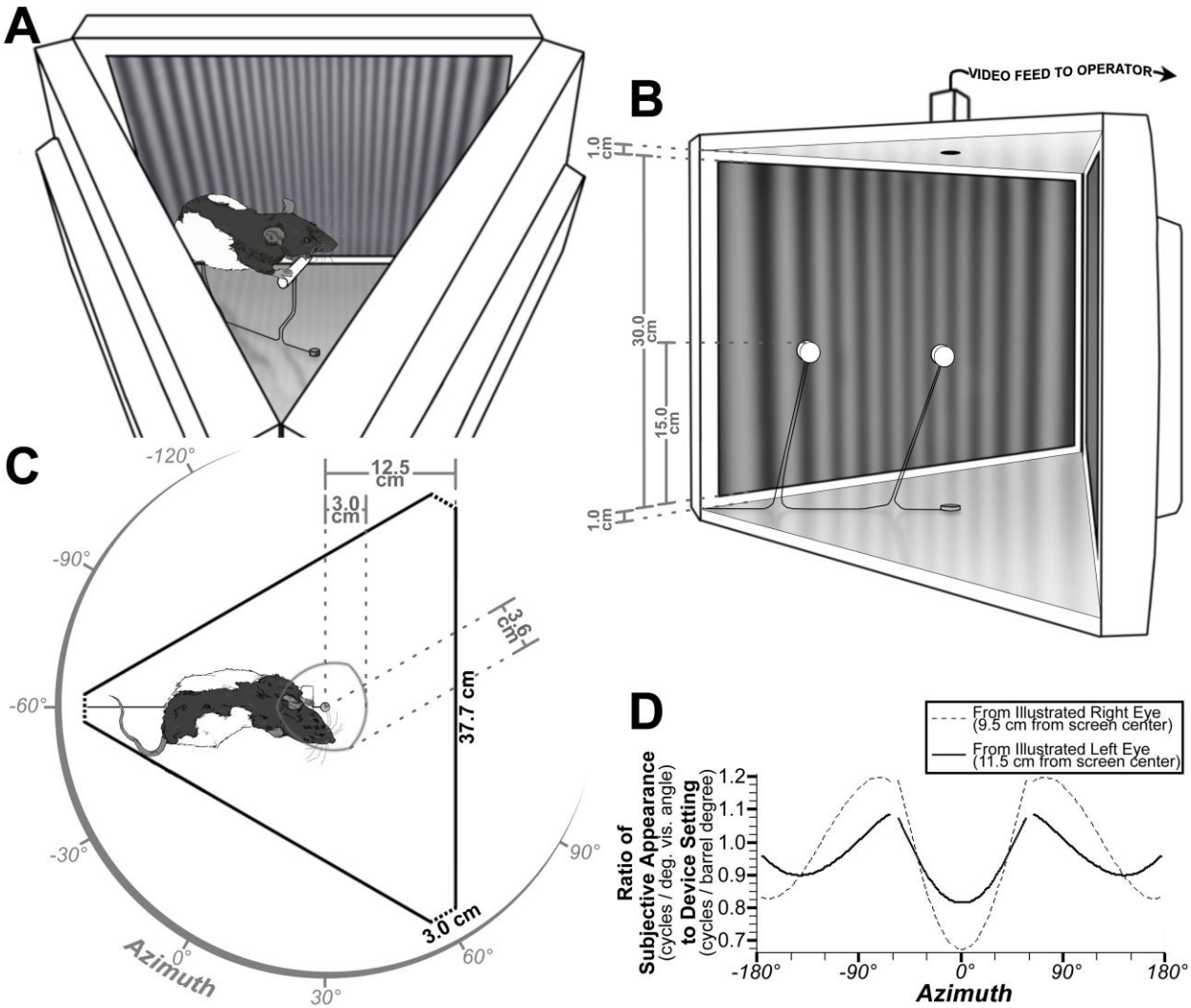

Figure 1: Schematics of the in-house-built OKT device. The stimulation chamber is made of three computer screens arranged in an equilateral triangle, with mirrors placed on the floor and ceiling. Structural elements not visible to the rat, used for instance to mount and secure screens, are omitted from this figure. For presentation purposes, the black plastic screen casings are depicted here as being white. *A:* An oblique view, with the ceiling of the stimulation chamber removed, showing the typical position of a compliant rat during optokinetic tracking. *B:* Side view, with one screen removed but floor and ceiling mirrors in place. Aside from the padded areas for hind- and forelimb placement, the stand is constructed of a single piece of metal wire (as from a clothes-hanger) secured at the center of, and at one corner of, the stimulation chamber's floor. *C:* An overhead view showing the functional elements of the stimulation chamber. The 37.7 cm-wide screen faces are represented by solid black lines, and edges connected by dashed lines (the corners of the device are occupied by screen casings; not shown here). The rat's right eye is shown just inside of the bulging-triangle shape that defines the testing arena at device center. Tracking was ignored unless the stimulated eye (left eye if the virtual barrel was moving clockwise; right if counter-clockwise) was inside the arena. The arena was not marked within the stimulation chamber, but instead was marked on the operator's screen, superimposed on and calibrated to the overhead video feed. Azimuth — direction in the horizontal plane with 0° at the center of the lower left screen — is shown here, and used as the x-axis for D. *D*: As a rat's eye moves closer to a screen, the subjective breadth of the nearest dark-light-dark cycle shown on that screen increases (i.e. less of the cycle fits within a degree visual angle). Measuring from the position of the rat's left eye in C, and a device setting of 0.111 c/bd (used for contrast sensitivity measurements), stimuli at 0° azimuth will have the spatial frequency of 0.091 cycles per degree visual angle. This is plotted as a cycles-per-degree-visual-angle to cycles-per-barrel-degree ratio of 0.82(=0.091/0.111). Near the corners of the device (gaps at -60° and 60° represent screen casings), ratios near 1.08 indicate that the 0.111 c/bd stimulus has a subjective spatial frequency of (1.08=0.120/0.111) 0.120 cycles per degree visual angle. For the right eye, which is closer to the screen center at 0° azimuth, a 0.111 c/bd setting means that stimuli will subjectively range from ~0.076 to ~0.133 cycles per degree visual angle. In this way, a single device setting can cover the range of frequencies in which Long-Evans rats' contrast sensitivity is best (Douglas et al., 2005; Keller et al., 2000).

Prior to experimentation, light intensities within each sine wave grating were calibrated using a Traceable Dual-Range Light Meter (Control Company, Friendswood, TX). The minimum value (black or dark grey) taken from a grating was shown uniformly on all three screens, and light intensity (lx) measured from the center of the device. This procedure was repeated for the maximum value (white or light grey), and used to calculate the Michelson contrast ([max. lx - min. lx]/[max. lx + min. lx]) of each grating. An animal's SFT is measured as the highest c/bd that elicits optokinetic tracking in either direction when testing at the highest contrast setting available to the device (black vs. white; ~ [97 lx - 1 lx]/[97 lx + 1 lx]). We carefully validated these SFT measurements (see Arm 4) and found that the maximum SFT for a given animal is highly reproducible and well-correlated with performance on the commercial OptoMotry system purchased more than mid-way through this project (CerebralMechanics, Lethbride, Alberta, Canada). CS measurements always took place at 0.111 c/bd — intended to expose the rat to the optimal subjective spatial frequency (~0.1 cycles per degree visual angle; Douglas et al., 2005; Keller et al., 2000) at most positions in the tracking arena (Fig.1D). For CS measurements, the highest $[\text{Michelson contrast}]^{-1}$ that elicited tracking in either direction is reported. Gratings always moved at 12° per second, as in previous work (Douglas et al., 2005; Prusky et al., 2008).

2.2.4 Eye Patch: A few days after testing an animal's visual function, we measured its eye morphology and retinal ion influx with MEMRI. To study both light and dark-adapted retina from the same rat, an opaque eye patch was adhered to one side of the head while the rat was anesthetized with diethyl ether, as previously described (Bissig & Berkowitz, 2011). Briefly, after the selected eye was sutured shut and protected by application of puralube (Pharmaderm; Melville, New York), the patch was adhered with a combination of eyelash glue (Andrea

modlash adhesive; American International Industries, Los Angeles, CA) and spirit gum (Mehron Inc., Chestnut Ridge, NY). Each rat was fit with an Elizabethan collar and monitored until full recovery from anesthesia (≤ 15 min). Rats were then dark-adapted overnight with free access to food and water. In all cases, visual inspection confirmed that sutures remained intact and patches remained fully adhered during monocular exposure to normal lab lighting on the following day, which was immediately followed by MRI scanning.

In Group YM, the left eye was patched for 9 of the 18 rats contributing MRI data to the first time point, and 4 of the 11 contributing to the final time point. In Group MO, the left eye was patched for 13 of the 32 rats contributing MRI data to the first time point, and 7 of the 14 (5 of the 11 injected with Mn^{2+}) contributing to the final time point.

2.2.5 Acquisition of MEMRI Data: As is previous work (Bissig & Berkowitz, 2011), animals were (binocularly) dark-adapted overnight after being fit with a patch. After that period of dark-adaptation, rats were placed in normal lab lighting (~300 lx) for ~30 min. Rats were then injected intraperitoneally with 44 mg $MnCl_2 \cdot 4H_2O$ / kg body weight (i.e., 222 μmol Mn^{2+} / kg; 0.1 M solution in 0.9%saline) on the following day. We have repeatedly demonstrated that this dose is non-toxic to the rat retina, (Berkowitz et al., 2006; Berkowitz et al., 2007a). After this injection, rats continued their monocular exposure to normal lab lighting until they were anesthetized prior to scanning. All scanning procedures took place under dim red light or darkness.

Immediately before MRI scans began, animals were anesthetized with a mixture of ketamine and xylazine ('k/x'; 20 mg ketamine and 2 mg xylazine / ml 0.9%saline). Maintenance doses of k/x were administered between the individual scans needed for T_1 measurements, without moving the rat, through an intraperitoneal line accessed from just outside the magnet

bore. Across all experiments, the loading dose of k/x used to induce anesthesia was about half (mean(SD): 49(15)%) of the total dose**,** which is reported below. Anesthesia began immediately before the first scans, ~4 hr after Mn^{2+} injection. This timing allows for substantial retinal Mn^{2+} uptake while rats are awake and free-moving — our standard procedure for measuring retinal function (Berkowitz et al., 2006; Berkowitz et al., 2009; Tofts et al., 2010; Bissig & Berkowitz, 2011). Due to the low efflux rate of Mn^{2+} from the retina (half-life of ~15 hr; Tofts et al., 2010), uptake represents Mn^{2+} influx. Mn^{2+} influx/uptake is measured with MEMRI as a change in spin-lattice relaxation rate (ΔR_1) which is directly proportional to tissue Mn^{2+} concentration (Chuang et al., 2009).

Scans of the left eye began (mean(SD)) 4.4(0.4) hr after Mn^{2+} injection, and were immediately followed by scans of the right eye (beginning 5.5(0.7) hr post-Mn^{2+}). For each eye, tissue R_1 (= $1/T_1$) was measured as follows: Using a 1.0 cm diameter receive-only coil on a 7 T Bruker ClinScan system, retinal images were collected at eight different TRs with a standard spin-echo sequence (echo time (TE) 13, 160 × 320 matrix, slice thickness 600 µm; 8 × 8 mm^2 field of view; yielding an in-plane resolution of 50 µm from superior to inferior × 25 µm in the axial (optic nerve to cornea) direction). Multiple repeat images were collected at lower TRs (total number given in brackets), then registered and averaged offline to improve signal-to-noise. Images were collected in the following order: TR 0.15 s [6], 3.50 s [1], 1.00 s [2], 1.90 s [1], 0.35 s [4], 2.70 s [1], 0.25 s [5] 0.50 s [3].

2.2.6 Acquisition of Baseline (no Mn^{2+}) Data: To aid in the interpretation of MEMRI data, the above procedures for measuring T_1 in a light-exposed and dark-adapted eye of the same animal were performed in nine rats *without* Mn^{2+} injection. The patched and unpatched eyes of young (n=3, aged 74(5) d, weighing 296(17) g), mid- (n=3, 198(7) d, 417(25) g) and old adult

rats (n=3, 570(29) d, 557(60) g) were scanned under k/x anesthesia (11.4(2.0) ml/kg) starting 5.1(0.6) hr after exposure to normal lab lighting began — closely matching the timing in Mn^{2+}-injected rats. In two of the three rats at each age, the patch was applied to the left eye. Since old adult Long-Evans rats were not commercially available, those three rats were randomly selected from Group MO.

2.2.7 Analysis of MEMRI Data; Optics: Eye morphology was measured in high-resolution (25 μm, axial) T_1-weighted images (TR 1.0 s). From each eye, we measured anterior chamber depth, lens thickness, posterior chamber depth (the sum of those three measurements being axial length), as well as the radius of curvature ("rC") for the anterior lens surface, posterior lens surface, and external surface of the cornea. These measurements of size and position of optical components (summarized in Figure 2) were made using semi-automated scripts written in R (v.2.9.0; R Development Core Team (2009); http://www.r-project.org), and used to calculate the quality of light focus on the retinal photoreceptors. The result, refractive state, is expressed in diopters (D) with positive values indicating hyperopia, and negative values myopia. For a near-sighted (myopic) rat with a refractive state of -4 D, for instance, light from a distant object would be optimally focused on the photoreceptors if a -4 D artificial lens were placed at the eye.

The refractive state of the eye was calculated using Hughes (1979)'s two shell ("core") lens model, and the refractive indices reported therein. A full description of this calculation is found in Hughes (1979) (see also Hughes, 1972; Southall, 1918), and in our recent application of that model to MRI images of the juvenile rat eye (Chui et al., 2012). We note some minor alterations to Hughes' original model: First, although Hughes (1979) measures corneal thickness, and uses it to calculate refractive state, the present MRI images are not optimized for that measurement. Though some layering within the cornea is visible (Fig.2), we find that the border

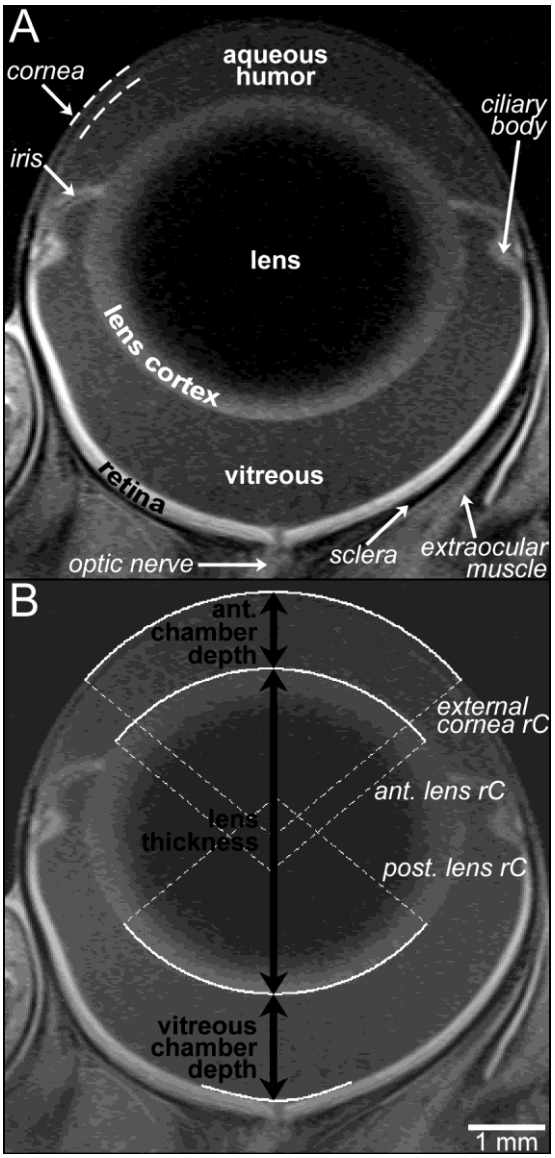

Figure 2: Anatomy of the rat eye and associated optics measurements. *A:* A high-resolution (25 μm) T1-weighted image of an old adult rat eye with anatomical labels overlaid on large structures (bold text) or indicating finer structures (arrows; italic text). White dashed lines indicate internal and external borders of the cornea. Despite the high image quality — layering is evident within both the cornea and retina — the internal border separating cornea and aqueous humor is subtle. *B:* Measurements of lens thickness and chamber depths (black arrows and text) and radii of curvature (rC) are overlaid on the same image shown in *A*, but with image brightness and contrast altered to help visualize labels.

of cornea and aqueous humor is too subtle for reliable measurement in the present images. We therefore calculate corneal thickness by its ratio to axial length, as reported by Hughes (1979)(axial length / corneal thickness = 23.004). The interior rC for the cornea is calculated by subtracting this corneal thickness value from the exterior corneal rC measured in each MRI. Second, the diameter of the spherical lens core, which is centered in the lens, is set proportional to (based on Hughes (1979), 51.67% of) the thickness of the lens measured in each MRI. Since Hughes (1979)'s model was originally developed with young adult rats, these modifications were used here and in previous work (Chui et al., 2012) to scale the model for age-related changes in eye/lens size. Finally, the position of the image plane must be estimated within the retina: Retinal thicknesses are calculated from MRI images as described below, and the image plane is placed at 84% of that thickness ('84%thick') beyond the vitreoretinal border. The 84%thick figure is based on recent *in vivo* optical coherence tomography (OCT) images of Long-Evans rat retinas (Srinivasa et al., 2006a; Srinivasa et al., 2006b; Hariri et al., 2009) which place the border between the outer

nuclear layer and bacillary layer (rod inner and outer segments) at ~71%thick, and the border between bacillary layer and retinal pigment epithelium at ~93%thick. Since inner segments are ~2/3rds the length of outer segments throughout adulthood (Hagins et al., 1970; Katz et al., 1991; Cohen, 1971; Cunea & Jeffery, 2007; Case & Plummer, 1993; Penn & Williams, 1986) the 84%thick estimate places the image plane at the photopigment-laden rod outer segments.

2.2.8 Analysis of MEMRI Data; Spatial Normalization and Retinal Morphology: These procedures were adopted without modification from Bissig and Berkowitz (2011), and are detailed therein. Briefly, we started by fitting polynomials to the vitreoretinal border. Polynomials were integrated about the central axis of the eye to calculate retinal surface area and, in combination with retinal thicknesses (see below), retinal volume. Signal intensities were sampled along perpendiculars to the polynomials, then organized as a linearized image of the retina. The distance from optic nerve to ciliary body was measured for each hemiretina, and values were averaged to calculate retinal extent. The linearized retina was then binned in 10% increments of that distance, %extent, with 0%extent at the optic nerve head, and 100%extent at the ora serrata (junction of retina and ciliary body). Average signal intensity as a function of retinal depth was calculated for each %extent bin, producing a signal intensity profile. Vitreoretinal and retina/choroid borders were demarked in each profile (where signal intensity fell halfway between the local minimum and maximum) and subtracted to calculate retinal thickness. Profiles were then resampled from a μm scale to a %thick scale, with 0%thick at the vitreoretinal border, and 100%thick at the retina/choroid border, in 4%thick increments. These spatially-normalized signal intensity profiles were used to facilitate comparisons of tissue Mn^{2+} uptake: Although the retina thins with greater age and greater distance from the optic nerve, the relative (%thick) position of each retinal layer is stable in healthy adults (Katz & Robison, 1986; Feng et al., 2007; Braekevelt

& Hollenberg, 1970). We report average retinal thicknesses and tissue Mn^{2+} uptake for the central retina (10-30%extent).

We have previously demonstrated the internal validity of the above measurements of retinal extent, surface area, thickness, and volume through comparison of left and right eyes (Bissig and Berkowitz, 2011). In young control rats, whole-retinal thickness measurements have been externally validated with histology (Berkowitz et al., 2006).

2.2.9 Analysis of MEMRI Data; Retinal Mn^{2+} Uptake: As described in the previous subsection, central retinal signal intensity ('SI') profiles were measured at each TR. These signal intensities were used to calculate tissue T_1 based on the equation $SI = a + b * (\exp(-TR / T_1))$, where a, b, and T_1 are fitted parameters. Data were fit with this function by the Levenberg-Marquardt nonlinear least-squares algorithm using the minpack.lm library (v.1.1.1, written by Timur V. Elzhov and Katharine M. Mullen) for R. Binned central retinal data were then averaged to produce a single profile of T_1 as a function of depth into the retina (i.e., %thick).

The inverse of T_1 varies linearly with tissue Mn^{2+} concentration (Chuang et al., 2009). Because this value, (T_1^{-1}=) R_1, is influenced by other tissue characteristics, Mn^{2+} uptake was measured by calculating the difference between Mn^{2+}-enhanced R_1 and the baseline (i.e., without Mn^{2+} injection) retinal R_1, yielding the measurement ΔR_1. Based on measurements from the rat brain (Chuang et al., 2009), ΔR_1s of 0, 0.5, and 1 s^{-1} represent tissue Mn^{2+} concentrations of approximately 0, 80, and 160 μM. In rats studied after monocular exposure to normal lab lighting, we also measured differences between retinal Mn^{2+} uptake in dark- versus light-adapted eyes, both proportional ($\Delta R_{1,Dark} / \Delta R_{1,Light}$) and absolute ($\Delta R_{1,Dark} - \Delta R_{1,Light}$).

Data from 16-28%thick were averaged to represent inner retinal ΔR_1s, while data from 48-68%thick were averaged to represent outer retinal ΔR_1s. These spans respectively fall within

the inner plexiform and outer nuclear layers, based on *in vivo* OCT images of Long-Evans rat retinas (Srinivasa et al., 2006a; Srinivasa et al., 2006b; Hariri et al., 2009). For completeness, we also report R_1s and ΔR_1s at all depths (%thick) into the retina in this Arm.

2.2.10 Statistics: We began by evaluating baseline (i.e., no Mn^{2+}) R_1s. Since these data were collected in young, mid-, and old-adult rats, we first tested for effects of age by looking for significant correlations (α=0.05) between age and either $R_{1,Dark}$, $R_{1,Light}$, or the dark-light difference ($R_{1,Dark}$ - $R_{1,Light}$) at each depth into the retina between 12 and 88%thick. Areas closer to the retina/non-retina borders (between 0-12% and 88-100%thick) are routinely excluded to avoid partial-volume averaging with non-retina (Bissig & Berkowitz, 2011; Berkowitz et al., 2012). The same tests were run on the averaged values for inner (16-28%thick) and outer (48-68%thick) retina. These analyses suggested no baseline effect of age (see Results), but because false-negatives are the primary concern in these comparisons of baseline data, two other approaches were attempted: We re-ran these regression analyses after log-transforming ages, and also analyzed the baseline data with one-way ANOVAs (young vs. mid vs. old). Since statistical findings were similar with these alternative approaches (P>0.05 for all age comparisons of baseline data) the results from these alternative analyses are not discussed further.

Since we found no effect of age on $R_{1,Dark}$, $R_{1,Light}$, or dark-light differences, we ignored age when testing whether dark-light differences were present within the baseline data. Paired two-tailed t-tests (n=9 pairs of eyes) compared $R_{1,Dark}$ to $R_{1,Light}$ at each depth between 12 and 88%thick, and for the averaged inner and outer retinal values. Since false-negatives were the primary concern in these analyses, α was set to 0.10 (so as to match the threshold of one-tailed tests in Mn^{2+}-enhanced retinas; see below), and no adjustment for multiple comparisons was made. No influence of light on baseline R_1 (see Results) was found. We therefore averaged

across ages and lighting conditions to generate a single baseline inner retinal R_1 (0.514 s^{-1}), outer retinal R_1 (0.568 s^{-1}), and retinal R_1 profile. These R_1s were subtracted from the Mn^{2+}-enhanced R_1s, discussed next, to generate ΔR_1s.

Based on previous *in vivo* MEMRI studies (e.g. Berkowitz et al., 2009; Berkowitz et al., 2006; Bissig & Berkowitz, 2011), as well as the general finding that outer retinal ion influx is greatest in darkness when photoreceptors there are fully depolarized (for review, see Yau, 1994), two major patterns were expected, irrespective of the hypothesized age-related changes in Mn^{2+} uptake: (1) Mn^{2+}-enhanced R_1s are expected to be higher than baseline (no Mn^{2+}) R_1s, and (2) in the outer half of the retina (where photoreceptors are located), Mn^{2+} uptake is expected to be higher in the patched, dark-adapted eye than in the unpatched, light-exposed eye. To test for these patterns, one-tailed t-tests (unpaired for Mn^{2+}-enhanced > baseline; paired for dark > light; α=0.05) were performed at each depth into the retina between 12 and 88%thick, and for the averaged inner and outer retinal regions. In addition to dark-light differences evaluated with paired t-tests, we also generated dark/light ratios (i.e. $\Delta R_{1,Dark}/\Delta R_{1,Light}$) to test whether they differed significantly from 1 (one-sample t-tests). As in previous work (e.g. Berkowitz et al., 2009; Berkowitz et al., 2006; Bissig & Berkowitz, 2011) dark-light differences are *not* expected in the inner-most portions of Mn^{2+}-enhanced retinas, since the light-driven (ON) and dark-driven (OFF) pathways are approximately equally represented, and since there is extensive spatial overlap of each pathway, the relevant neurons cannot be resolved at the present image resolution.

Next, we tested for longitudinal changes in each variable. Paired two-tailed t-tests were used to compare the first to final time point within each group, testing, for instance, whether retinal surface area increased significantly between ages ~2.5 and ~7 mo in Group YM. Body weight, and visual function (CS, SFT) had additional paired comparisons, since these

measurements were also recorded at the intermediate time point in Group MO. To control type I error in these multiple comparisons, only results falling below a standard false discovery rate threshold ('FDR'; q=0.05 on these 52 tests; Genovese et al., 2002) were considered significant.

Most variables changed with age (see Results). To better-understand these changes, we compared variables with four rounds of regression analyses: (1) We tested whether variables are correlated with one-another at the first time point. For instance, do rats which start the study with above-average body weight also start with above-average axial length? (2) We tested whether the first measurement of a variable is correlated with the last measurement of the same variable. For instance, do rats which start the study with above-average body weight tend to have above-average body weight at the end of the study? (3) We tested whether the change in a variable over time is correlated with the change in another variable over the same time. For instance, do rats which show the greatest increases in body weight also show the greatest increases in axial length? A rate was used here to remove any influence of the minor age differences within each group, and log-transformed age was used in the denominator since lifespan changes in most variables are well-approximated by a logarithmic function (see Supplemental Material in Appendix A): In Group YM, for instance, each subject's change from the initial measurement of a variable ('VAR') to the final measurement (from age ~2.5 mo to age ~7 mo) is calculated as $(VAR_{final} - VAR_{initial}) / (\ln(age_{final}) - \ln(age_{initial}))$. In Group MO, changes relative to the intermediate time point are calculated in an identical fashion. Group MO changes from study start to study end are treated in the same way, but use a linear best fit (after log-transforming age) to the three measurements available for SFT, CS, and body weight. (4) Also, we tested whether the change in a variable over time is correlated with the starting value of the same, or of any other, variable. For instance, do rats which start with the highest body weights show the

greatest increases in axial length in the following months? We further checked for relationships between starting value for ln(age) and changes over time: Presuming a logarithmic growth curve, the youngest animals will tend to show the greatest changes over a fixed follow-up interval. Though within-group age differences are small at each time point, it's important to check that a given variable's predictive power is not merely due to initial age. In these analyses, we use the same log-transformed rates as in (3).

Where possible, data from both Groups YM and MO are combined prior to statistical testing. Values from each group at each age — and for rates, each time span — are standardized by conversion to z-scores: For instance, a Group YM subject's standardized retinal thickness at age ~2.5 mo is (subject's measured retinal thickness - [mean of YM retinal thicknesses at ~2.5 mo])/[SD of YM retinal thicknesses at ~2.5 mo]. Standardizing scores has no effect on p-values or correlation coefficients (Pearson's r) when testing one group at a time, but allows both groups to be combined in the same analysis without biasing the outcome due to differences in group means or variances. For instance, we tested the hypothesis that retinal thickness is correlated with low SFT (i.e. poor vision): Standardized YM and MO data were combined to see whether subjects with thinner-than-average retinas (for their respective groups, i.e., negative z-scores) have worse-than-average SFTs (for their respective groups, i.e., negative z-scores). Before finalizing comparisons, we also tested for Group × variable (e.g. thickness) interactions. These could occur if, for instance, retinal thickness was related to SFT in mid-, but not young, adults. In the presence of a suspected interaction ($P<0.05$; not corrected for multiple comparisons) groups were analyzed separately. When there was no evidence of an interaction ($P>0.05$) formal statistical testing used only the combined (YM and MO) analysis. For completeness, though, we report correlation coefficients from each group.

For each round of regression analyses above ((1) through (4)) results were considered significant below a standard FDR threshold (q=0.05). Some *post-hoc* testing was used to further interpret positive results, and exact p-values are reported in those cases.

2.3 Results

2.3.1 Baseline R_1: Representative baseline R_1 maps are shown in Figure 3. In dark-adapted (i.e., patched) eyes, mean±SEM R_1 for the *inner* retina (16-28%thick) was 0.52±0.03 s^{-1} (young 0.58±0.04 s^{-1}; mid 0.44±0.03 s^{-1}; old 0.54±0.04 s^{-1}) and for the *outer* retina was 0.57±0.03 s^{-1} (young 0.64±0.01 s^{-1}; mid 0.49±0.05 s^{-1}; old 0.59±0.04 s^{-1}). Results were similar in unpacthed eyes, which were exposed to normal lab lighting: For the *inner* retina, R_1 was 0.51±0.02 s^{-1} (young 0.53±0.03 s^{-1}; mid 0.51±0.03 s^{-1}; old 0.48±0.07 s^{-1}). For the outer retina, R_1 was 0.56±0.03 s^{-1} (young 0.59±0.05 s^{-1}; mid 0.50±0.03 s^{-1}; old 0.60±0.03 s^{-1}). Consistent with expectations for these control animals, which were not injected with Mn^{2+}, there were no significant dark-light differences in either *inner* retina or *outer* retina (P>0.23). We found no effects of age on R_1s in dark, light, or dark-light differences (*inner retina*: -0.32<r<0.21 with P>0.41; *outer retina*: -0.18<r<0.17 with P>0.66). The above analyses yielded similarly negative (P>0.05) results when extended to the entire retinal profile. Age-averaged profiles for dark, light, and the dark-light difference are shown in Figure 4.

Because baseline (no Mn^{2+}) R_1s were stable with age and light exposure, we averaged across ages and lighting conditions to generate a single baseline inner retinal R_1 (0.514 s^{-1}) outer retinal R_1 (0.568 s^{-1}), and retinal R_1 profile (see Fig.4). Those mean baseline values are subtracted from Mn^{2+}-enhanced R_1s in all arms of this study to generate ΔR_1s.

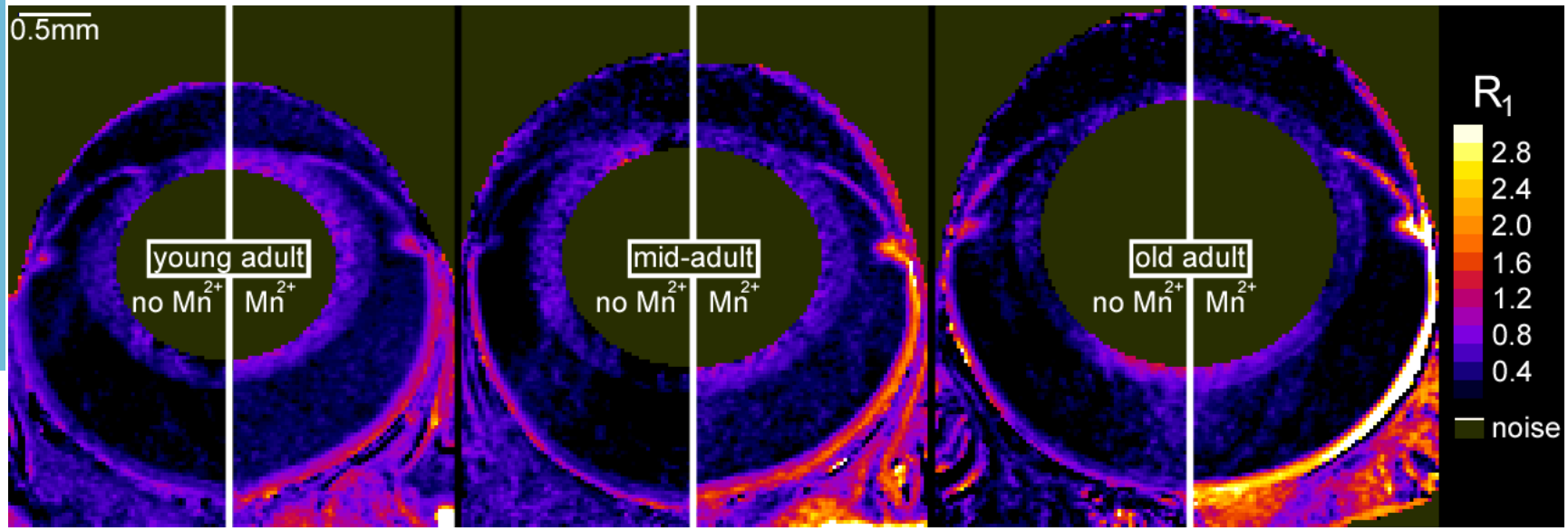

Figure 3: Representative maps of tissue R_1 (in units of s^{-1}) showing age-related changes in eye anatomy and retinal physiology. Dark-adapted (patched) eyes are shown from rats injected with Mn^{2+} (from Arm 1) and control (no Mn^{2+}) rats at three different ages; young (~2.5 mo), mid- (~7 mo), and old adulthood (~19 mo). Axial length, lens thickness, and anterior chamber depth noticeably increase with age (see Fig.2 for anatomical labels). The retinal extent (distance form Optic N. to ciliary body) and therefore surface area of the vitreoretinal border also increase with age. In the absence of Mn^{2+}, retinal R_1 is stable with age. In Mn^{2+}-injected rats, R_1 clearly increases with age. Since R_1 is linearly related to tissue Mn^{2+} concentration (Chuang et al., 2009) this demonstrates that Mn^{2+} uptake increases with age. Note that in most analyses, the stable R_1 from controls is subtracted from Mn^{2+}-injected R_1s to yield ΔR_1, which is linearly related and directly proportional to Mn^{2+} uptake. Also note that these R_1 maps are for illustration only: Formal measurements of R_1, as shown in Figure 4, used linearized and spatial-normalized retinal data.

2.3.2 R_1s and ΔR_1s from Mn^{2+}-enhanced Retinas: Representative R_1 maps showing the effects of Mn^{2+} injection and age are shown in Figure 3. Quantitative details of the results summarized here are provided in Figure 4 and legend.

Rat retinas showed the expected Mn^{2+}-enhancement at all ages, based on the finding that those R_1s were significantly higher ($P<0.05$) than baseline (no Mn^{2+}) at all retinal depths. Also, consistent with expectations, *inner* retinal Mn^{2+} uptake was similar ($P>0.05$) in light and darkness, but *outer* retinal Mn^{2+} uptake was significantly higher ($P<0.05$) in dark-adapted (patched) eyes than in the unpatched eyes, which were exposed to normal lab lighting during the period of Mn^{2+} accumulation (Berkowitz et al., 2009; Berkowitz et al., 2006; Bissig & Berkowitz, 2011). This activity-dependent pattern of Mn^{2+} uptake was noted at all ages when testing whether the difference between $R_{1,Dark}$ and $R_{1,Light}$ was significantly different from zero (i.e. paired t-tests of $R_{1,Dark}$ versus $R_{1,Light}$), whether that difference was significantly greater than the (near-zero and non-significant) dark-light differences in baseline (no Mn^{2+}) data, and when testing whether the dark/light ratio of Mn^{2+} uptake (i.e., $\Delta R_{1,Dark}/\Delta R_{1,Light}$) was significantly greater than 1.

Note that the paired comparisons of $R_{1,Dark}$ to $R_{1,Light}$ are identical to paired comparisons of $\Delta R_{1,Dark}$ and $\Delta R_{1,Light}$ since a common baseline value is used to calculate ΔR_1s from R_1s: A paired t-test is equivalent to a one-sample t-test (versus zero) on the difference scores, which are $\Delta R_{1,\,Dark} - \Delta R_{1,\,Light} = [(R_{1,\,Dark} - R_{1,\,Baseline}) - (R_{1,\,Light} - R_{1,\,Baseline})] = R_{1,\,Dark} - R_{1,\,Light}$. The same considerations apply to paired comparisons of longitudinal data (e.g. young-adult versus mid-adult $\Delta R_{1,\,Dark}$ in Group YM).

Retinal Mn^{2+} uptake significantly ($q<0.05$; Fig.4) increased with age in both Group YM and Group MO. This effect was found in both light and darkness, and in both the inner and outer

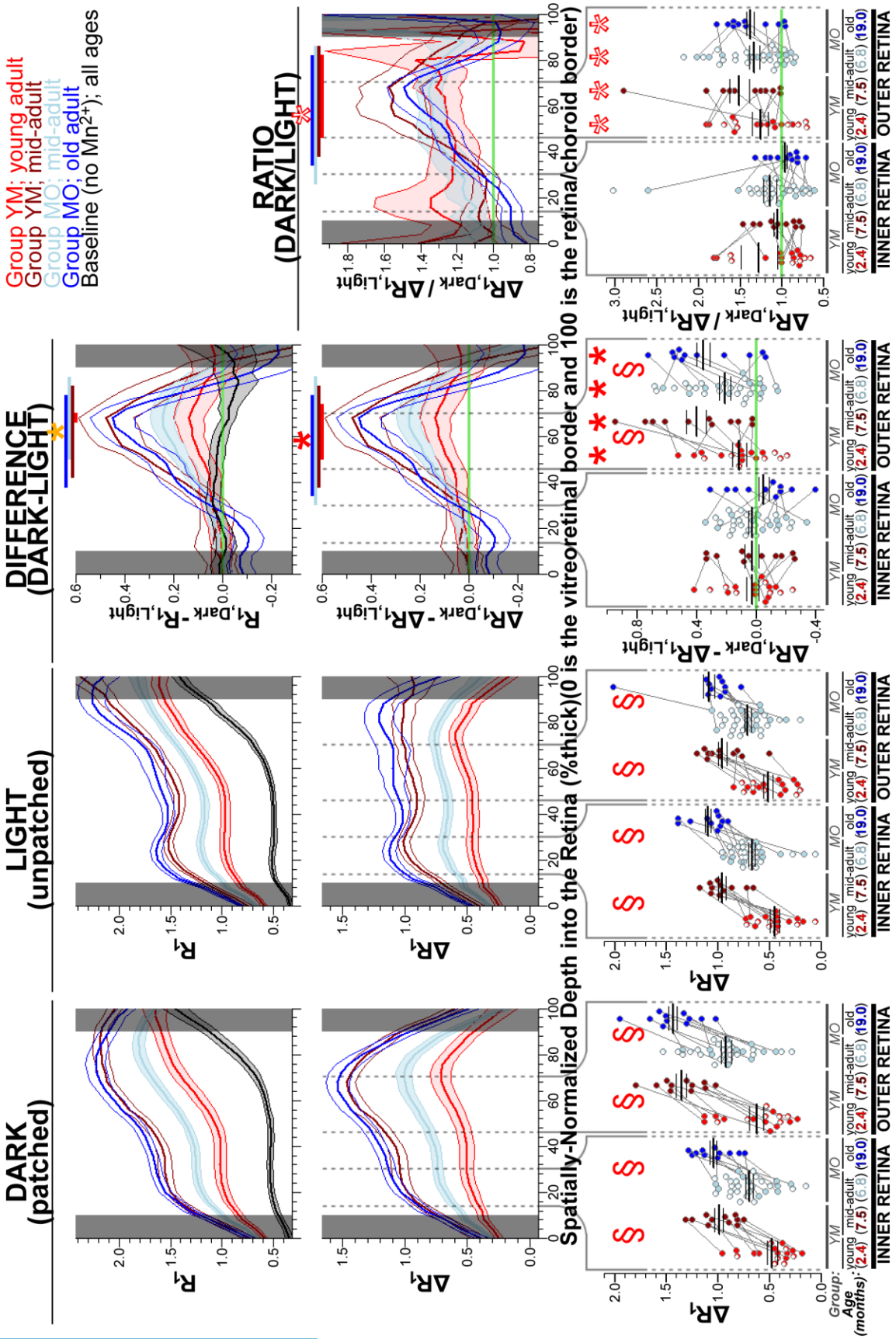

Figure 4 (previous page): Light- and age-dependent changes in Mn^{2+} uptake in Arm 1. *Top Row:* Plots of R_1 (in units of s^{-1}) as a function of depth into the retina for the dark-adapted retina, light-adapted retina, and the dark-light difference in R_1s. Profiles are color-coded by group (*top right*). Grayed areas near the vitreoretinal (0%thick) and retina/choroid (100%thick) borders are routinely ignored to avoid partial-volume averaging with non-retina. Mn^{2+}-enhanced R_1s are significantly higher than baseline (i.e., no Mn^{2+}) in both light and dark in all four Mn^{2+}-enhanced datasets (P<0.0002 at all depths from 12-88%thick; one-tailed t-tests; not labeled). Dark-light differences greater than 0 (marked with a green line) indicate activity-dependent Mn^{2+} uptake. No dark-light differences were found for the baseline group, consistent with expectations. For other groups, this check of activity-dependent Mn^{2+} uptake is shown in the middle and bottom rows of this figure. Here, the orange * indicates dark-light differences significantly greater than those calculated at baseline (no Mn^{2+}) over the span indicated for each group by color-coded bars (P<0.05; one-tailed t-tests). *Middle Row*: Plots of ΔR_1 (in units of s^{-1}) which is directly proportional to tissue Mn^{2+} concentration (Chuang et al., 2009). ΔR_1 is calculated by subtracting the baseline (no Mn^{2+}) tissue R_1 from the Mn^{2+}-enhanced R_1. Note that the dark-light differences in this row are identical to in the top row of this figure because the same baseline (averaged across ages and lighting conditions) is used to calculate dark and light ΔR_1s (i.e. $\Delta R_{1,Dark} - \Delta R_{1,Light} = (R_{1,Dark} - R_{1,baseline}) - (R_{1,Light} - R_{1,baseline})$). Filled red * indicates dark-light differences significantly greater than 0 (P<0.05; one-tailed t-tests). The dark-to-light ratio is shown at figure right, with the absence of light-dependent Mn^{2+} uptake (ratio = 1) marked with a green line. The open red * indicates dark/light ratios significantly greater than 1 (P<0.05; one-tailed t-tests). Note that ratio profiles become highly variable near the retinal borders (at 0 and 100%thick) due to partial-volume averaging with non-retina, which has little Mn^{2+} uptake and therefore smaller (and occasionally negative) denominator ($\Delta R_{1,Light}$) values. Dashed vertical lines indicate the regions selected for further analyses — the inner retina from 16-28%thick, and the outer retina from 48-68%thick. *Bottom Row:* Inner and outer retinal means from each subject are shown, with one exception: For the inner retina, a young adult dark/light ratio value of 4.69 is omitted to retain a useful y-axis range (but was retained in statistical comparisons; this is the only scatter plot omission throughout the entire present work). Mean±SEM are indicated by the thick and thin horizontal lines overlaid on each scatter plot. Horizontal offset of points avoids overlap. Measures from the same subject (at different ages) are connected by gray lines, while a white mark within a point denotes the lack of follow-up MEMRI data (e.g., due to animal death). Note that values from rats lost to follow-up are fairly evenly distributed among (and statistically similar to P>0.05) those from animals retained for longitudinal comparisons. As with profiles, filled red *s indicate dark-light differences significantly greater than 0 (all outer retinal tests P<0.017), and open red *s indicates dark/light ratios significantly greater than 1 (all outer retinal tests P<0.0058). Consistent with the inner retina's intermingled and equally-represented ON and OFF pathways, no activity-dependent changes in inner retinal Mn^{2+} uptake were noted. § indicates a significant (q<0.05; paired two-tailed tests) effect of age in longitudinal comparisons — young vs. mid-adults in Group YM, and mid- vs. old adults in Group MO. Retinal Mn^{2+} uptake (ΔR_1s) increased significantly with age in both darkness (all P<8.4e-4) and light (all P<5.3e-4). Activity-dependent Mn^{2+} uptake — measured as outer retinal dark-light differences — also increased with age (both P<0.038). Interestingly, the dark-to-light ratio of Mn^{2+} uptake was stable with age (P>0.3; uptake was consistently ~35% higher in dark than light). We considered the possibility that ratio values simply had greater variance, making it more difficult to detect age effects. However, outer retinal tests for activity-dependent changes had similar effect sizes when testing whether dark-light > 0 and dark/light > 1: For the young and mid-adults of Group YM as well as the mid- and old adults of Group MO, Cohen's d was respectively 0.54, 1.27, 0.88, and 1.30 for differences and nearly identical for ratios: respectively 0.67, 0.94, 0.87, and 1.30. Thus, variance does not appear inflated in *outer* retinal dark/light ratios. In short, the data demonstrate stability in the dark-to-light ratio of Mn^{2+} uptake — despite age-related increases in the total quantity of Mn^{2+} uptake in dark, in light, and the activity-dependent difference in Mn^{2+} uptake revealed by outer retinal dark-light differences.

retina. In the *inner* retina, dark-light differences in Mn^{2+} uptake were similar to zero (P>0.05) in all cases and did not change with age (P>0.05). Dark/light ratios showed a similar pattern. In the *outer* retina, the absolute amount of activity-dependent Mn^{2+} uptake — represented by dark-light differences in ΔR_1 — increased significantly (q<0.05) with age in both groups. Interestingly, the outer retina's dark/light ratios did not change with age (P>0.05).

2.3.3 Visual Function: SFT declined from ages ~2.5 to ~7 mo (q<0.05; P=2.4e-4) and then remained stable from ~7 mo onward (P>0.26 for all Group MO comparisons of SFT). In contrast, each longitudinal comparison of CS showed significant (q<0.05) declines with age in

both Group YM (*P*=3.4e-2) and Group MO (*P*=2.7e-4 for ~7 to ~11.5 mo; *P*=1.3e-4 for ~11.5 to ~19 mo). These data are plotted in Figure 5.

2.3.4 Morphology: Significant (q<0.05; Fig.5) results were found for each longitudinal comparison of retinal morphology (*P*<8.3e-3), radii of curvature ('rC's; *P*<2.0e-5), refractive state (*P*<5.3e-3), and axial length (*P*<1.7e-5). The age-related increase in axial length was mostly driven by significant (q<0.05) increases in lens thickness (*P*<4.5e-6) and anterior chamber depth (*P*<4.3e-3), rather than vitreous chamber depth (*P*=0.22 from young to mid-adulthood; *P*=0.031 from mid- to old adulthood). In most cases, the magnitude change in morphology from young to mid-adulthood appears similar to the change from mid- to old adulthood. This is consistent with a logarithmic growth curve, since the log-transformed age differences in those comparisons are similar (i.e., ln(19 mo) - ln(7 mo)) ≈ ln(7 mo) - ln(2.5 mo)). Body weight appeared to stabilize from ~11.5 to ~19 mo (*P*=0.08), but significantly increased with age over all other ranges (q<0.05; *P*<1.1e-6; Fig.5). Further exploration of these growth patterns is offered as Supplemental Material in Appendix A.

2.3.5 Regression Analyses: Results are presented in Tables 1-4. Before considering relationships with visual function, we summarize the inter-relationships of the other variables:

Correlations found for several morphological variables seem generally linked to eye growth beyond young adulthood: Body weight, anterior chamber depth, lens thickness, axial length, corneal radius of curvature, lens radii of curvature, retinal extent, and retinal surface area all share the following features: (1) As seen in Table 1, they all are significantly (q<0.05) *positively* correlated to one-another at the start of the experiment (i.e. at age ~2.5 mo in Group YM, at ~ 7mo in Group MO), such that rats which weighed more also tended to have a larger axial lengths, retinal surface areas, etc. (2) As seen in Table 2, the starting value for each is

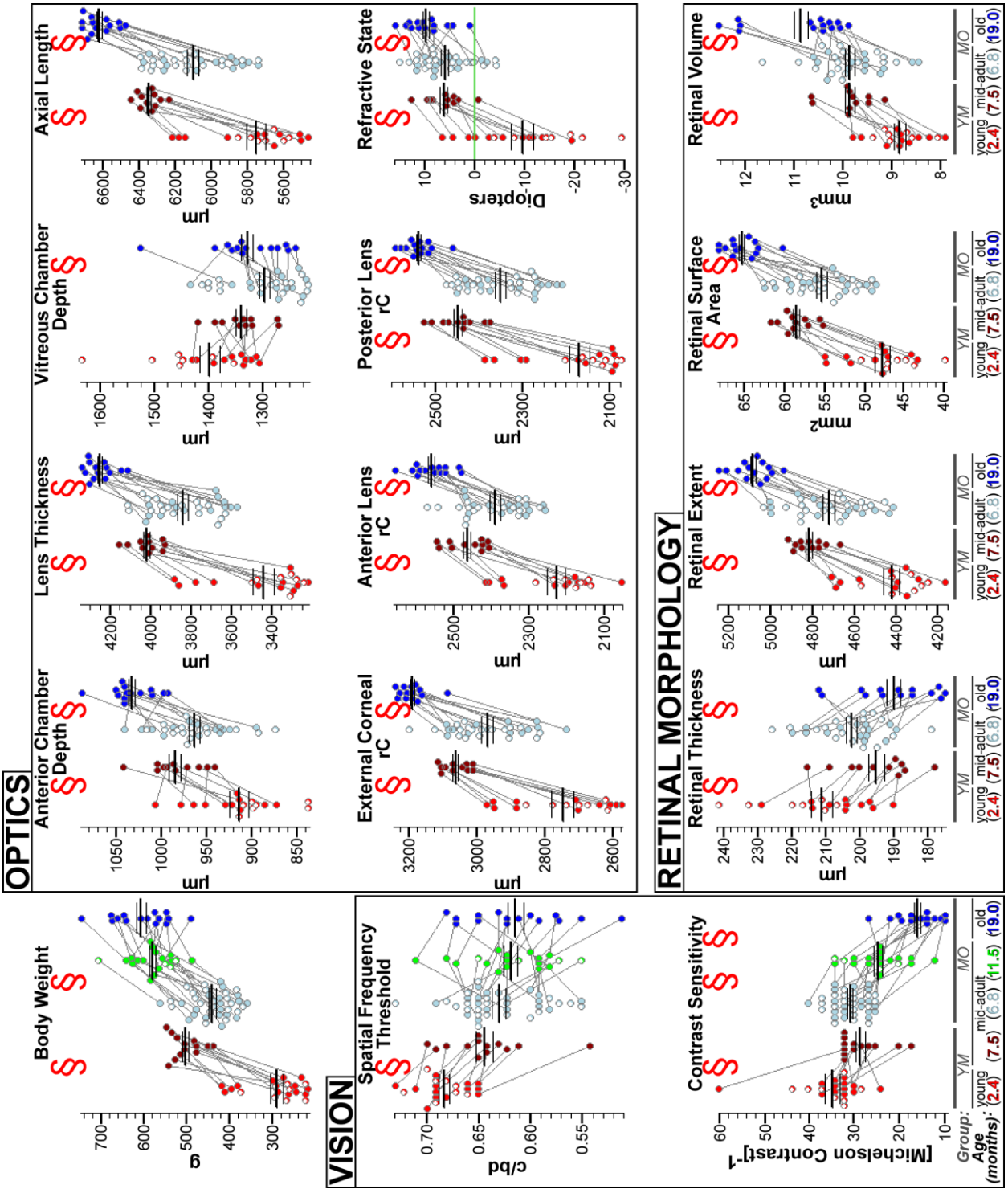

Figure 5 (previous page): Longitudinal changes in body weight, visual function, the morphology of optical components, and retinal morphology. As in Figure 4, mean±SEM are indicated by the thick and thin horizontal lines overlaid on each scatter plot. Measures from the same subject (at different ages) are connected by gray lines, while a white mark within a point denotes the lack of follow-up MEMRI data (e.g., due to animal death). Note that values from rats lost to follow-up are evenly distributed among those from animals retained for longitudinal comparisons. § indicates a significant (q<0.05; paired two-tailed tests) effect of age. For SFT, CS, and body weight, comparisons of ~7 to ~19 mo data are not labeled since patterns of significance (respectively, *P*=0.57, *P*=2.1e-7, *P*=5.1e-8) are well-depicted by the ~7 vs. ~11.5 mo comparisons. Body weight tends to stabilize from 11.5 mo onward, and SFT tends to stabilize after the initial decline from young to mid-adulthood. CS progressively declines with age. Refractive state calculations indicate that rats are hyperopic (i.e., >0 diopters; indicated by the green horizontal line) through most of their life, but myopic (<0 diopters) as young adults. The sizes of most eye structures and the associated radii of curvature ('rC'), increase with age. This general pattern of eye growth is noted in retinal morphology as well: The retina thins with age, and may partially be due to stretching of the retina as the eye continues to grow (Katz & Robison, 1986), as suggested by increases in retinal extent and surface area with age. Since retinal volume increases with age, it seems unlikely that thinning is due to cell loss.

significantly (q<0.05) *positively* correlated with the final value, such that rats with larger-than-average axial lengths at study start with tend to have larger-than-average axial lengths at study end. (3) As seen in Table 3, the rate of change in each is significantly (q<0.05) *positively* correlated with the rate of change in the other 'eye growth' variables, such that rats which show the largest increases in axial length over time tend to show the largest increases in retinal surface area over the same time. (4) As seen in Table 4 (pt.2), each variable mentioned here is significantly *negatively* correlated with later changes in self, and in other 'eye growth' variables: Rats with above-average body weight at the first time point will tend to have the smallest gains in body weight by the final time point, and will similarly have the smallest gains in retinal surface area, lens thickness, etc. The above relationships also hold reasonably well for refractive state, though changes in refractive state over time (Tables 3 and 4) are well-correlated with only some of the 'eye growth' variables (e.g. corneal rC, but not lens thickness). This may be due to significant relationships between refractive state and vitreous chamber depth, which is poorly correlated with most other variables.

The relationships between most morphological measures over time may be summarized in the following way: A larger-than-average rat at the start of the experiment it is nearer to its final size than the other members of its cohort. Growth of that rat in the following months is modest, relative to growth in smaller-than-average animals, which end up at a similar final size

as the larger rats. Morphological data thereby tend to converge over time, a pattern readily seen in Figure 5 (e.g., for external corneal rC). For most variables, this convergence is incomplete: The larger-than-average rat at the start of the study remains larger-than-average at the end, but by a smaller margin. Anterior chamber depth is one exception to this pattern: Though initial size is well-correlated with later growth (Table 4), values converge so much that starting smaller- or larger-than-average has no bearing on whether a rat will end with a smaller- or larger-than-average anterior chamber. The non-significant regression result in Table 2 describes this pattern, which is visible in Figure 5: Most of the connecting lines intersect for anterior chamber depth, but not, for instance, for external corneal rC.

Patterns observed for retinal volume were similar to those for the 'eye growth' variables described above. Central retinal thickness and volume are related — animals whose central retinas thin least over time tend to have the greatest increases in retinal volume over time (significant positive correlation in Table 3) — but changes in thickness were poorly correlated with changes in 'eye growth' variables. Although cross-sectional comparison of retinal thickness and surface area suggests an inverse relationship — as though some animals' retinas were more 'stretched out' (greater surface area), resulting in thinner central retina at the start of the experiment ($q<0.05$ for negative correlation; Table 1) — there was no correlation between rates of change in surface area and retinal thickness ($q>0.05$; Table 3).

Mn^{2+} uptake in dark-adapted outer retina ($\Delta R_{1,Dark}$) is well-correlated with uptake in the inner retina at the start of the experiment (Table 1), and changes in these variables over time were well-correlated (Table 3). Rats starting with high Mn^{2+} uptake (relative to other cohort members) in either location tended to have the smallest subsequent increases in Mn^{2+} uptake (Table 4). Values converged enough that starting Mn^{2+} uptake was not well-correlated with Mn^{2+}

Table 1: Correlations between measurements at the first time point in Arm 1. Correlation coefficients (Pearson's r) are listed for each analysis as [(Group YM , Group MO) Combined]. Bold indicates significance (q<0.05; FDR calculated on 205 tests): When r is listed for the combined analysis, group-specific r values are shown only for completeness. When * appears instead of an r value, an interaction between group and the correlation was suspected (P<0.05) and statistics were run on each group separately.

	SFT	CS	Ant. Chamber Depth	Lens Thickness	Vit. Chamber Depth	Axial Length	Corneal rC	Anterior Lens rC	Posterior Lens rC	Refractive State	Retinal Thickness	Retinal Extent	Retinal Surface Area	Retinal Volume	ΔR_1, (inner retina)	$\Delta R_{1,Dark}$ (outer retina)	$\Delta R_{1,Light}$ (outer retina)	$\Delta R_{1,Dark}$ - $\Delta R_{1,Light}$ (outer retina)	$\Delta R_{1,Dark}$ / $\Delta R_{1,Light}$ (outer retina)
Body Weight	(0.0,-0.2) -0.12	(0.5,0.2) **0.33**	(0.6,0.5) **0.53**	(0.9,0.9) **0.87**	(-0.4,0.1) -0.03	(0.8,0.8) **0.83**	(0.8,0.8) **0.75**	(0.9,0.8) **0.85**	(0.9,0.8) **0.80**	(0.7,0.4) **0.48**	(-0.5,-0.4) **-0.42**	(0.8,0.8) **0.81**	(0.8,0.8) **0.79**	(0.6,0.7) **0.65**	(**0.8**,0.2) *	(**0.8**,0.2) *	(0.6,0.2) **0.33**	(0.6,0.1) 0.28	(0.3,0.1) 0.16
SFT		(0.1,-0.1) 0.02	(0.1,-0.4) -0.22	(0.1,-0.3) -0.12	(-0.1,0.1) 0.05	(0.1,-0.2) -0.12	(0.0,-0.2) -0.11	(0.2,-0.1) -0.01	(0.1,-0.4) -0.19	(0.1,-0.1) -0.07	(0.0,0.0) -0.03	(0.2,-0.2) -0.01	(0.3,-0.1) 0.04	(0.3,0.0) 0.09	(0.2,-0.2) -0.07	(0.1,-0.2) -0.07	(0.5,-0.1) 0.13	(-0.3,-0.2) -0.23	(-0.5,-0.2) -0.28
CS			(0.3,0.1) 0.15	(0.6,0.1) 0.28	(-0.1,0.2) 0.10	(0.5,0.2) 0.31	(0.5,0.1) 0.21	(0.5,0.1) 0.22	(0.5,0.2) **0.34**	(0.4,-0.2) 0.02	(-0.2,0.1) -0.01	(0.5,0.0) 0.16	(0.5,-0.1) 0.14	(0.4,0.0) 0.13	(0.4,-0.2) 0.03	(0.4,0.0) 0.14	(0.5,-0.2) *	(0.0,0.2) 0.13	(0.0,0.2) 0.13
Ant. Chamber Depth				(0.6,0.6) **0.60**	(-0.5,-0.1) -0.26	(0.6,0.6) **0.61**	(0.4,0.6) **0.52**	(0.6,0.6) **0.58**	(0.6,0.6) **0.58**	(0.6,0.4) **0.49**	(-0.6,-0.3) **-0.40**	(0.6,0.6) **0.56**	(0.6,0.6) **0.61**	(0.1,0.4) **0.33**	(0.5,0.0) 0.19	(0.5,0.0) 0.17	(0.3,0.1) 0.12	(0.4,0.0) 0.13	(0.2,-0.1) 0.00
Lens Thickness					(-0.3,0.1) -0.04	(1.0,0.9) **0.95**	(0.9,1.0) **0.94**	(1.0,1.0) **0.96**	(1.0,0.9) **0.95**	(0.8,0.5) **0.60**	(-0.6,-0.3) **-0.36**	(0.9,0.9) **0.87**	(0.8,0.9) **0.85**	(0.6,0.8) **0.72**	(**0.7**,0.1) *	(**0.8**,0.1) *	(**0.6**,0.0) *	(0.5,0.2) 0.30	(0.2,0.2) 0.19
Vit. Chamber Depth						(0.0,0.4) 0.23	(-0.2,0.1) -0.03	(-0.3,0.1) -0.05	(-0.4,0.1) -0.05	(-0.8,-0.8) **-0.76**	(**0.7**,0.1) *	(-0.2,0.2) 0.01	(-0.5,0.0) -0.16	(0.2,0.1) 0.17	(-0.4,-0.2) -0.27	(-0.4,-0.1) -0.21	(-0.2,-0.2) -0.18	(-0.4,0.0) -0.13	(-0.2,0.1) -0.03
Axial Length							(0.9,0.9) **0.89**	(0.9,0.9) **0.91**	(0.9,0.9) **0.90**	(0.5,0.3) **0.36**	(-0.4,-0.2) -0.29	(0.8,0.9) **0.85**	(0.7,0.8) **0.78**	(0.7,0.8) **0.73**	(**0.6**,0.0) *	(**0.7**,0.1) *	(0.5,-0.1) 0.15	(0.4,0.1) 0.24	(0.2,0.1) 0.15
Corneal rC								(0.9,0.9) **0.92**	(0.9,0.9) **0.88**	(0.8,0.6) **0.65**	(-0.6,-0.3) **-0.38**	(0.8,0.8) **0.84**	(0.8,0.8) **0.82**	(0.5,0.8) **0.68**	(0.5,0.0) 0.20	(0.6,0.1) 0.25	(0.5,0.0) 0.18	(0.4,0.1) 0.18	(0.2,0.0) 0.09
Anterior Lens rC									(0.9,0.9) **0.92**	(0.7,0.5) **0.60**	(-0.6,-0.3) **-0.38**	(0.9,0.8) **0.85**	(0.9,0.8) **0.84**	(0.7,0.8) **0.73**	(0.7,0.2) **0.38**	(0.7,0.2) **0.41**	(0.6,0.1) 0.26	(0.5,0.2) 0.31	(0.2,0.1) 0.16
Posterior Lens rC										(0.8,0.4) **0.56**	(-0.6,-0.3) **-0.38**	(0.8,0.7) **0.74**	(0.8,0.7) **0.73**	(0.6,0.6) **0.60**	(**0.8**,0.1) *	(**0.8**,0.2) *	(**0.6**,0.0) *	(0.5,0.3) **0.36**	(0.2,0.2) 0.22
Refractive State											(-0.8,-0.3) **-0.52**	(0.7,0.4) **0.50**	(0.8,0.5) **0.61**	(0.1,0.4) 0.27	(0.5,0.2) **0.32**	(0.6,0.1) **0.32**	(0.4,0.2) 0.26	(0.5,0.0) 0.21	(0.2,0.0) 0.08
Retinal Thickness												(-0.6,-0.3) **-0.38**	(-0.7,-0.3) **-0.44**	(0.1,0.1) 0.09	(-0.4,-0.1) -0.22	(-0.6,-0.4) **-0.44**	(-0.2,-0.3) -0.25	(-0.6,-0.2) **-0.37**	(-0.5,-0.2) -0.28
Retinal Extent													(0.9,1.0) **0.96**	(0.7,0.8) **0.79**	(0.6,0.0) 0.21	(**0.6**,0.0) *	(0.5,0.0) 0.17	(0.3,0.0) 0.13	(0.2,0.0) 0.08
Retinal Surface Area														(0.5,0.8) **0.73**	(**0.6**,0.0) *	(**0.6**,0.0) *	(0.5,0.0) 0.18	(0.3,0.0) 0.10	(0.1,0.0) 0.03
Retinal Volume															(0.4,0.1) 0.19	(0.3,0.0) 0.11	(0.5,0.0) 0.16	(-0.1,0.0) -0.01	(-0.2,0.0) -0.07
ΔR_1, (inner retina)																(0.9,0.8) **0.86**	(0.9,0.8) **0.79**	(0.5,0.4) **0.41**	(0.2,0.2) 0.16
$\Delta R^{1,Dark}$ (outer retina)																	(0.7,0.6) **0.64**	(0.7,0.7) **0.73**	(0.4,0.5) **0.49**
$\Delta R_{1,Light}$ (outer retina)																		(0.0,-0.1) -0.05	(-0.3,-0.3) -0.31
$\Delta R_{1,Dark}$ - $\Delta R_{1,Light}$ (outer retina)																			(0.9,0.9) **0.92**

Table 2: Correlations between measurements at the start versus at the end of the study in Arm 1. Correlation coefficients (Pearson's r) values are listed for each comparison. Bold indicates significance ($q<0.05$; FDR calculated on 26 tests — twenty of the combined data and six with the ~11.5 mo age as a start or endpoint). Formal analyses combined z-standardized Group YM and Group MO data. For completeness, r values calculated for each group are also shown.

		from the start to the end of the experiment			**with ~11.5 mo data as start or endpoint**	
	Group	**YM**	**MO**	**Combined**	**MO**	
	Age Range (months)	~2.5 to ~7	~7 to ~19	←	~7 to ~11.5	~11.5 to ~19
	Body Weight	(n=13)	(n=15)	(n=28)	(n=19)	(n=15)
		0.05	0.41	0.25	**0.85**	**0.60**
Behavior		(n=13)	(n=15)	(n=28)	(n=19)	(n=15)
	STF	0.77	0.59	**0.67**	0.37	**0.68**
	CS	0.11	0.06	0.09	0.40	0.37
Morphology and Optics		(n=11)	(n=14)	(n=25)		
	Ant. Chamber Depth	0.08	0.05	0.06		
	Lens Thickness	0.90	0.77	**0.83**		
	Vit. Chamber Depth	0.52	0.51	**0.52**		
	Axial Length	0.72	0.53	**0.61**		
	Corneal rC	0.83	0.68	**0.75**		
	Anterior Lens rC	0.84	0.37	**0.57**		
	Posterior Lens rC	0.76	0.39	**0.55**		
	Refractive State	0.80	0.53	**0.65**		
	Retinal Thickness	0.80	0.08	0.39		
	Retinal Extent	0.73	0.60	**0.66**		
	Retinal Surface Area	0.74	0.62	**0.67**		
	Retinal Volume	0.55	0.12	0.31		
Physiology		(n=11)	(n=11)	(n=22)		
	ΔR_1 (inner retina)	0.29	0.01	0.15		
	$\Delta R_{1,Dark}$ (outer retina)	0.39	0.12	0.26		
	$\Delta R_{1,Light}$ (outer retina)	0.11	0.61	0.36		
	$\Delta R_{1,Dark} - \Delta R_{1,Light}$ (outer retina)	0.31	0.52	0.42		
	$\Delta R_{1,Dark} / \Delta R_{1,Light}$ (outer retina)	0.04	0.48	0.26		

Table 3: Correlations between rate of change in one variable with rate of change in another in Arm 1. Correlation coefficients (Pearson's r) are listed for each analysis as [(Group YM , Group MO) Combined]. Bold indicates significance (q<0.05; FDR calculated on 206 tests): When r is listed for the combined analysis, group-specific r values are shown only for completeness. Where an * appears instead of an r value, an interaction between group and the correlation was suspected (P<0.05) and statistics were run on each group separately. Additional tests (included in the 206 total) using Group MO's age ~11.5 mo data as a start or endpoint (body weight vs. SFT, body weight vs. CS, and SFT vs. CS) all produced negative results (-0.31<r<0.27; P>0.2; not shown).

	SFT	CS	Ant. Chamber Depth	Lens Thickness	Vit. Chamber Depth	Axial Length	Corneal rC	Anterior Lens rC	Posterior Lens rC	Refractive State	Retinal Thickness	Retinal Extent	Retinal Surface Area	Retinal Volume	ΔR_1, (inner retina)	$\Delta R_{1,Dark}$ (outer retina)	$\Delta R_{1,Light}$ (outer retina)	$\Delta R_{1,Dark}$ - $\Delta R_{1,Light}$ (outer retina)	$\Delta R_{1,Dark}$ / $\Delta R_{1,Light}$ (outer retina)
Body Weight	(-0.1,-0.2) -0.14	(0.8,0.4) **0.61**	(0.6,0.6) **0.61**	(0.8,0.6) **0.71**	(0.3,0.2) 0.26	(0.8,0.6) **0.72**	(0.7,0.7) **0.69**	(0.7,0.6) **0.65**	(0.8,0.7) **0.75**	(0.4,0.2) 0.32	(-0.2,0.2) 0.02	(0.8,0.5) **0.61**	(0.7,0.5) **0.60**	(0.4,0.5) 0.45	(0.6,-0.1) 0.24	(0.5,0.2) 0.37	(0.5,0.3) 0.38	(0.2,0.0) 0.10	(0.4,0.2) 0.28
SFT		(0.0,0.0) 0.00	(0.1,0.0) 0.08	(0.0,-0.1) -0.06	(0.0,0.0) 0.04	(0.0,0.0) -0.01	(-0.2,0.2) 0.01	(0.2,0.2) 0.16	(0.0,0.0) 0.02	(-0.3,0.2) -0.02	(0.5,-0.1) 0.18	(-0.2,0.0) -0.09	(-0.3,-0.1) -0.22	(0.3,0.0) 0.12	(-0.1,0.3) 0.10	(0.1,0.1) 0.10	(-0.2,-0.1) -0.13	(0.3,0.2) 0.23	(0.0,-0.1) -0.05
CS			(0.5,0.5) **0.50**	(0.8,0.4) **0.59**	(0.1,0.1) 0.11	(0.7,0.5) **0.58**	(0.8,0.6) **0.68**	(0.7,0.6) **0.57**	(0.8,0.5) **0.63**	(0.7,0.3) 0.47	(0.2,-0.1) 0.02	(0.7,0.5) **0.58**	(0.7,0.6) **0.61**	(0.5,0.4) 0.46	(0.7,0.0) 0.34	(0.4,-0.1) 0.18	(0.6,0.0) 0.29	(0.0,0.0) 0.02	(0.0,0.0) 0.02
Ant. Chamber Depth				(0.8,0.7) **0.73**	(-0.1,0.3) 0.12	(0.8,0.8) **0.80**	(0.4,0.8) **0.60**	(0.7,0.6) **0.67**	(0.7,0.8) **0.75**	(0.3,0.2) 0.26	(-0.4,0.2) -0.06	(0.8,0.7) **0.77**	(0.8,0.8) **0.79**	(0.3,0.6) 0.46	(**0.7**,-0.2) *	(0.6,-0.2) 0.18	(0.6,0.2) 0.37	(0.2,-0.5) -0.13	(0.2,-0.4) -0.12
Lens Thickness					(0.1,0.3) 0.20	(1.0,0.9) **0.94**	(0.8,0.8) **0.84**	(0.9,0.7) **0.77**	(1.0,0.9) **0.93**	(0.7,0.2) 0.39	(-0.1,0.5) 0.23	(0.9,0.9) **0.91**	(0.8,0.8) **0.80**	(0.6,0.7) **0.69**	(**0.9**,-0.3) *	(0.6,0.1) 0.35	(0.7,0.0) 0.35	(0.1,0.1) 0.11	(0.1,0.2) 0.16
Vit. Chamber Depth						(0.3,0.6) 0.46	(0.1,0.4) 0.26	(0.3,0.4) 0.34	(0.3,0.3) 0.28	(-0.4,-0.7) **-0.54**	(0.1,0.4) 0.27	(0.1,0.1) 0.10	(-0.1,0.1) 0.02	(0.1,0.2) 0.15	(0.1,-0.3) -0.12	(0.4,-0.2) 0.10	(0.2,-0.5) -0.15	(0.3,0.3) 0.26	(0.3,0.2) 0.25
Axial Length							(0.8,0.9) **0.82**	(0.9,0.7) **0.82**	(1.0,0.9) **0.92**	(0.5,-0.1) 0.18	(-0.1,0.5) 0.22	(0.9,0.8) **0.86**	(0.8,0.8) **0.77**	(0.6,0.7) **0.64**	(**0.8**,-0.4) *	(0.7,-0.1) 0.30	(0.7,-0.1) 0.29	(0.2,0.0) 0.11	(0.2,0.1) 0.14
Corneal rC								(0.8,0.8) **0.81**	(0.8,0.8) **0.83**	(0.9,0.3) **0.57**	(0.1,0.3) 0.21	(0.8,0.9) **0.82**	(0.7,0.8) **0.78**	(0.6,0.7) **0.66**	(0.7,-0.2) *	(0.2,0.0) 0.10	(0.7,-0.1) 0.28	(-0.3,0.1) -0.08	(-0.2,0.1) -0.07
Anterior Lens rC									(0.9,0.8) **0.86**	(0.6,0.2) 0.40	(0.0,0.1) 0.04	(0.9,0.5) **0.68**	(0.7,0.6) **0.64**	(0.7,0.3) 0.43	(**0.8**,-0.2) *	(0.5,0.0) 0.28	(0.7,0.0) 0.35	(0.0,0.1) 0.04	(0.0,0.0) 0.01
Posterior Lens rC										(0.6,0.2) 0.37	(0.1,0.3) 0.22	(0.9,0.7) **0.78**	(0.7,0.7) **0.72**	(0.7,0.6) **0.65**	(**0.8**,-0.4) *	(0.6,-0.1) 0.26	(0.7,0.0) 0.36	(0.1,-0.1) -0.01	(0.1,0.0) 0.06
Refractive State											(0.0,-0.5) -0.25	(0.6,0.4) **0.49**	(0.6,0.4) **0.52**	(0.5,0.1) 0.29	(0.5,0.1) 0.30	(0.0,-0.1) -0.05	(0.6,0.2) 0.37	(-0.4,-0.3) -0.36	(-0.4,-0.3) -0.34
Retinal Thickness												(-0.3,0.3) 0.05	(-0.4,0.2) -0.05	(0.5,0.6) **0.60**	(-0.1,0.2) 0.06	(-0.2,0.6) 0.20	(0.0,0.0) -0.01	(-0.2,**0.8**) *	(-0.4,0.7) *
Retinal Extent													(0.9,0.9) **0.94**	(0.5,0.8) **0.65**	(**0.8**,-0.2) *	(0.5,-0.1) 0.17	(0.8,-0.1) 0.34	(-0.1,-0.1) -0.08	(0.0,-0.1) -0.05
Retinal Surface Area														(0.3,0.7) **0.53**	(**0.8**,-0.2) *	(0.4,-0.3) 0.05	(0.8,-0.0) 0.37	(-0.2,-0.3) -0.25	(-0.1,-0.3) -0.22
Retinal Volume															(0.5,-0.1) 0.23	(0.1,0.0) 0.03	(0.6,-0.2) 0.19	(-0.3,0.1) -0.09	(-0.3,0.1) -0.11
ΔR_1, (inner retina)																(0.7,0.7) **0.72**	(0.9,0.6) **0.73**	(0.1,0.4) 0.23	(-0.1,0.1) 0.01
$\Delta R_{1,Dark}$ (outer retina)																	(0.4,0.6) **0.53**	(0.7,0.7) **0.70**	(0.5,0.5) 0.5
$\Delta R_{1,Light}$ (outer retina)																		(-0.3,-0.2) -0.23	(-0.4,-0.2) -0.33
$\Delta R_{1,Dark}$ - $\Delta R_{1,Light}$ (outer retina)																			(0.9,0.8) **0.85**

Table 4 (pt.1 on this page; pt.2 on following page): Correlations between starting values and subsequent rates of change over the several-month follow-up periods in Arm 1. Part 1 shows the correlations between starting measurements and the rate of change in either the ~4.5 mo following the first MRI, or in the ~4.5 mo to ~12 mo following MRI. Part 2 shows the correlations between starting measurements and the rate of change measured from the start to the end of the study — a ~4.5 mo period in Group YM, but ~12 mo period in Group MO. To fit Part 2 on a single printed page, an index number (from 1 to 21) was assigned to each starting variable. These are listed together in Part 1.

Correlation coefficients (Pearson's r) are listed for each analysis as [(Group YM,Group MO) Combined]. Bold indicates significance ($q<0.05$; FDR calculated on the 600 tests in pts.1 and 2 of this Table): When r is listed for the combined analysis, group-specific r values are shown only for completeness. Where an * appears instead of an r value, an interaction between group and the correlation was suspected ($P<0.05$) and statistics were run on each group separately. Combined analysis was not possible when testing for lagging predictors of change (i.e. dependent variable = change from ~4.5 mo to ~12 mo after study start) since only Group MO was tested over such a time period. Therefore only one number is shown for those analyses (right half of Table 4, pt.1). Note that Group YM's r values appear in both pt.1 and pt.2 — since the "~4.5 mo later" time point was also the end of the study for those rats — but are combined with different Group MO data.

		Predicting Change in Measurement (per unit ln(age))…						
		from the start of the study to ~4.5 mo later ***(Group YM, Group MO) Combined***			from ~4.5 mo after study start to ~12 mo after study start ***(Group MO)***			
		Body Weight	SFT	CS	Body Weight	SFT	CS	
Measured at the Start of the Study								
1	Body Weight	(-**0.9**,0.0) *	(-0.2,-0.2) -0.23	(-0.8,-0.2) **-0.46**	(-0.1)	(-0.1)	(-0.4)	
2	SFT	(0.0,0.0) 0.03	(0.2,-0.5) -0.18	(0.0,0.2) 0.14	(0.3)	(0.2)	(0.3)	
3	CS	(-0.7,-0.2) -0.37	(0.2,-0.3) -0.09	(-0.8,-0.3) **-0.51**	(-0.4)	(0.0)	(-0.2)	
4	Ant. Chamber Depth	(-0.5,-0.3) -0.37	(-0.4,0.0) -0.18	(-0.5,-0.1) -0.26	(-0.3)	(-0.1)	(-0.4)	
5	Lens Thickness	(-0.8,-0.3) **-0.50**	(-0.1,-0.1) -0.11	(**-0.8**,-0.1) *	(-0.3)	(-0.2)	(-0.4)	
6	Vit. Chamber Depth	(0.2,0.2) 0.18	(-0.2,-0.3) -0.25	(0.4,0.1) 0.22	(-0.2)	(0.0)	(-0.1)	
7	Axial Length	(-0.8,-0.2) **-0.44**	(-0.2,-0.2) -0.19	(-0.8,-0.1) -0.36	(-0.4)	(-0.2)	(-0.4)	
8	Corneal rC	(-0.6,-0.3) **-0.44**	(0.0,-0.2) -0.09	(**-0.8**,0.0) *	(-0.4)	(-0.2)	(-0.5)	
9	Anterior Lens rC	(-0.7,-0.3) **-0.46**	(-0.1,-0.2) -0.18	(-0.8,-0.2) **-0.43**	(-0.3)	(-0.1)	(-0.3)	
10	Posterior Lens rC	(-0.8,-0.3) **-0.49**	(0.0,-0.1) -0.07	(**-0.9**,-0.1) *	(-0.4)	(-0.2)	(-0.5)	
11	Refractive State	(-0.6,-0.4) **-0.45**	(0.1,0.1) 0.11	(**-0.8**,0.0) *	(-0.2)	(-0.2)	(-0.2)	
12	Retinal Thickness	(0.6,0.0) 0.23	(-0.2,-0.1) -0.13	(0.5,0.0) 0.17	(0.3)	(0.3)	(0.2)	
13	Retinal Extent	(-0.7,-0.3) **-0.49**	(0.0,0.0) -0.03	(-0.7,-0.1) -0.33	(-0.1)	(-0.1)	(-0.4)	
14	Retinal Surface Area	(-0.7,-0.3) **-0.49**	(0.1,0.0) 0.01	(**-0.8**,-0.1) *	(-0.1)	(-0.1)	(-0.4)	
15	Retinal Volume	(-0.6,-0.2) -0.38	(-0.2,-0.2) -0.18	(-0.6,-0.2) -0.36	(0.1)	(0.0)	(-0.3)	
16	ΔR_1 (inner retina)	(**-0.8**,0.4) *	(-0.1,0.1) 0.05	(-0.6,-0.7) **-0.68**	(0.0)	(-0.1)	**(0.6)**	
17	$\Delta R_{1,Dark}$ (outer retina)	(**-0.8**,0.2) *	(-0.1,0.2) 0.11	(-0.7,-0.8) **-0.74**	(-0.2)	(-0.2)	**(0.7)**	
18	$\Delta R_{1,Light}$ (outer retina)	(-0.6,**0.7**) *	(0.1,0.1) 0.07	(-0.6,-0.5) **-0.51**	(0.0)	(-0.1)	(0.4)	
19	$\Delta R_{1,Dark}$ - $\Delta R_{1,Light}$ (outer retina)	(-0.7,-0.4) **-0.53**	(-0.2,0.3) 0.08	(-0.5,-0.6) **-0.57**	(-0.2)	(-0.1)	(0.4)	
20	$\Delta R_{1,Dark}$ / $\Delta R_{1,Light}$ (outer retina)	(-0.6,-0.5) **-0.57**	(0.0,0.3) 0.16	(-0.4,-0.3) -0.37	(-0.2)	(-0.1)	(0.3)	
21	ln(Age)	(-0.4,0.5) *	(-0.3,-0.2) -0.29	(-0.6,0.1) -0.19	(0.3)	(-0.2)	(-0.2)	

Measured at the Start of the Study	Predicting Change in Measurement (per unit ln(age))… from the start to the end of study *(Group YM spanning ~4.5 mo, Group MO spanning ~12 mo)*															
	Body Weight	SFT	CS	Ant. Chamber Depth	Lens Thickness	Vit. Chamber Depth	Axial Length	Corneal rC	Anterior Lens rC	Posterior Lens rC	Refractive State	Retinal Thickness	Retinal Extent	Retinal Surface Area	Retinal Volume	ΔR_1, (inner retina)	$\Delta R_{1,Dark}$ (outer retina)	$\Delta R_{1,Light}$ (outer retina)	$\Delta R_{1,Dark}$ - $\Delta R_{1,Light}$ (outer retina)	$\Delta R_{1,Dark}$ / $\Delta R_{1,Light}$ (outer retina)
1	(-0.9,-0.2) **-0.54**	(-0.2,-0.1) -0.17	(-0.8,-0.2) **-0.49**	(-0.6,-0.5) **-0.55**	(-0.9,-0.7) **-0.80**	(-0.3,-0.2) -0.28	(-0.9,-0.7) **-0.77**	(-0.8,-0.8) **-0.77**	(-0.9,-0.5) **-0.67**	(-0.9,-0.5) **-0.71**	(-0.5,-0.3) -0.37	(-0.1,-0.2) -0.19	(-0.7,-0.9) **-0.81**	(-0.5,-0.8) **-0.68**	(-0.7,-0.5) **-0.59**	(-0.6,0.2) -0.24	(-0.5,0.1) -0.22	(-0.5,0.2) -0.14	(-0.2,-0.1) -0.14	(-0.3,0.1) -0.10
2	(0.0,0.4) 0.20	(0.2,-0.1) 0.05	(0.0,0.4) 0.23	(-0.2,0.5) 0.21	(-0.2,**0.6**) *	(-0.6,-0.2) -0.38	(-0.3,0.5) 0.14	(-0.1,0.4) 0.19	(-0.3,0.1) -0.05	(-0.2,0.5) 0.20	(0.2,0.2) 0.21	(0.3,0.4) 0.35	(-0.1,0.6) 0.30	(-0.1,0.5) 0.25	(0.1,0.7) 0.43	(-0.4,0.3) -0.01	(-0.6,0.4) *	(-0.3,0.6) *	(-0.3,-0.1) -0.20	(-0.2,0.1) -0.06
3	(-0.7,-0.4) **-0.55**	(0.2,0.1) 0.15	(-0.8,-0.6) **-0.67**	(-0.4,-0.2) -0.27	(-0.5,-0.3) -0.39	(-0.2,-0.3) -0.28	(-0.5,-0.4) -0.43	(-0.5,-0.3) -0.37	(-0.4,-0.3) -0.30	(-0.5,-0.2) -0.35	(-0.3,0.1) -0.06	(0.1,0.0) 0.08	(-0.6,-0.1) -0.32	(-0.7,0.0) -0.31	(-0.1,0.0) -0.06	(-0.5,0.1) -0.21	(-0.3,-0.3) -0.34	(-0.6,-0.1) -0.33	(0.1,-0.3) -0.13	(0.0,-0.6) -0.31
4	(-0.5,-0.5) **-0.51**	(-0.4,-0.1) -0.22	(-0.5,-0.4) -0.43	(-0.8,-0.9) **-0.84**	(-0.7,-0.6) **-0.63**	(-0.1,-0.3) -0.21	(-0.8,-0.7) **-0.72**	(-0.4,-0.7) **-0.57**	(-0.8,-0.4) **-0.54**	(-0.7,-0.6) **-0.60**	(-0.2,-0.2) -0.21	(0.1,-0.1) -0.01	(-0.8,-0.7) **-0.76**	(-0.7,-0.8) **-0.73**	(-0.4,-0.6) **-0.53**	(-0.6,0.1) -0.22	(-0.5,0.3) -0.08	(-0.5,0.0) -0.24	(-0.1,0.4) 0.13	(0.0,0.4) 0.21
5	(-0.8,-0.5) **-0.66**	(-0.1,-0.1) -0.10	(-0.8,-0.4) **-0.59**	(-0.7,-0.7) **-0.71**	(-1.0,-0.9) **-0.94**	(-0.2,-0.3) -0.27	(-0.9,-0.9) **-0.91**	(-0.9,-0.9) **-0.92**	(-1.0,-0.7) **-0.81**	(-1.0,-0.8) **-0.88**	(-0.7,-0.3) -0.46	(-0.1,-0.4) -0.25	(-0.9,-0.9) **-0.91**	(-0.8,-0.9) **-0.82**	(-0.7,-0.7) **-0.71**	(**-0.8**,0.2) *	(-0.5,0.0) -0.24	(**-0.8**,0.1) *	(0.1,-0.1) 0.00	(0.1,-0.1) 0.02
6	(0.2,0.0) 0.07	(-0.2,-0.2) -0.19	(0.4,0.0) 0.17	(0.0,-0.1) -0.08	(0.2,-0.3) -0.08	(-0.4,-0.3) -0.36	(0.0,-0.3) -0.16	(0.2,-0.2) -0.03	(0.0,-0.1) -0.09	(0.1,-0.2) -0.05	(0.5,0.4) 0.41	(-0.2,-0.6) -0.43	(0.0,-0.1) -0.03	(0.1,0.0) 0.03	(0.1,-0.2) -0.09	(0.2,-0.3) -0.06	(0.0,-0.7) -0.35	(0.0,-0.4) -0.18	(0.0,-0.6) -0.28	(0.1,-0.2) -0.09
7	(-0.8,-0.5) **-0.64**	(-0.2,-0.2) -0.16	(-0.8,-0.4) **-0.56**	(-0.7,-0.8) **-0.75**	(-0.9,-0.9) **-0.91**	(-0.2,-0.4) -0.33	(-0.9,-0.9) **-0.92**	(-0.8,-0.9) **-0.88**	(-1.0,-0.6) **-0.79**	(-0.9,-0.8) **-0.85**	(-0.6,-0.1) -0.34	(-0.1,-0.5) -0.31	(-0.9,-0.9) **-0.89**	(-0.8,-0.8) **-0.79**	(-0.7,-0.7) **-0.71**	(**-0.8**,0.1) *	(-0.5,-0.1) -0.32	(-0.8,0.0) -0.41	(0.1,-0.2) -0.04	(0.1,0.0) 0.03
8	(-0.6,-0.6) **-0.62**	(0.0,-0.2) -0.10	(-0.8,-0.3) **-0.53**	(-0.4,-0.7) **-0.59**	(-0.8,-0.9) **-0.83**	(-0.1,-0.3) -0.25	(-0.7,-0.9) **-0.81**	(-1.0,-1.0) **-0.96**	(-0.8,-0.7) **-0.77**	(-0.8,-0.8) **-0.80**	(-0.8,-0.3) **-0.54**	(-0.2,-0.3) -0.29	(-0.7,-0.9) **-0.81**	(-0.6,-0.8) **-0.73**	(-0.7,-0.7) **-0.69**	(-0.6,0.2) *	(-0.2,0.0) -0.08	(-0.7,0.1) -0.31	(0.3,-0.1) 0.13	(0.3,0.0) 0.15
9	(-0.7,-0.5) **-0.63**	(-0.1,-0.2) -0.15	(-0.8,-0.3) **-0.52**	(-0.7,-0.8) **-0.73**	(-0.9,-0.8) **-0.86**	(-0.2,-0.4) -0.33	(-0.9,-0.9) **-0.88**	(-0.9,-0.9) **-0.89**	(-0.9,-0.8) **-0.84**	(-0.9,-0.8) **-0.82**	(-0.7,-0.2) -0.41	(-0.1,-0.3) -0.21	(-0.8,-0.9) **-0.84**	(-0.7,-0.8) **-0.76**	(-0.7,-0.6) **-0.62**	(**-0.8**,0.1) *	(-0.5,0.0) -0.26	(-0.7,0.0) -0.38	(0.0,0.0) 0.00	(0.1,0.1) 0.07
10	(-0.8,-0.6) **-0.70**	(0.0,-0.1) -0.08	(-0.9,-0.4) **-0.61**	(-0.6,-0.9) **-0.75**	(-0.9,-0.9) **-0.93**	(-0.2,-0.4) -0.30	(-0.9,-0.9) **-0.93**	(-0.9,-0.9) **-0.89**	(-0.9,-0.7) **-0.81**	(-1.0,-0.9) **-0.93**	(-0.7,-0.1) -0.39	(-0.1,-0.4) -0.29	(-0.8,-0.8) **-0.84**	(-0.7,-0.8) **-0.75**	(-0.7,-0.7) **-0.70**	(**-0.9**,0.2) *	(-0.5,-0.1) -0.28	(-0.8,-0.1) -0.48	(0.1,0.1) 0.06	(0.1,0.0) 0.06
11	(-0.6,-0.4) **-0.49**	(0.1,0.0) 0.04	(-0.8,-0.1) -0.43	(-0.3,-0.4) -0.37	(-0.7,-0.4) **-0.53**	(0.0,0.0) 0.00	(-0.6,-0.4) -0.47	(-0.9,-0.6) **-0.72**	(-0.7,-0.5) **-0.55**	(-0.7,-0.5) **-0.56**	(-0.9,-0.6) **-0.72**	(-0.1,0.4) 0.15	(-0.6,-0.6) **-0.57**	(-0.5,-0.6) **-0.55**	(-0.6,-0.3) -0.43	(-0.6,0.5) *	(-0.1,0.6) 0.25	(-0.6,0.4) *	(0.3,0.4) 0.36	(0.2,0.2) 0.23
12	(0.6,0.3) 0.44	(-0.2,0.1) -0.03	(0.5,0.0) 0.22	(0.1,0.2) 0.16	(0.5,0.1) 0.30	(0.2,-0.3) -0.07	(0.5,0.0) 0.22	(0.7,0.2) 0.42	(0.6,0.1) 0.30	(0.5,0.2) 0.33	**0.59** 0.59	(-0.2,-0.6) -0.42	(0.5,0.2) 0.34	(0.4,0.2) 0.28	(0.4,0.0) 0.16	(0.3,-0.3) 0.02	(0.0,-0.3) -0.17	(0.3,0.1) 0.19	(-0.2,-0.5) -0.37	(0.0,-0.5) -0.24
13	(-0.7,-0.3) **-0.53**	(0.0,0.0) -0.03	(-0.7,-0.4) **-0.53**	(-0.7,-0.6) **-0.63**	(-0.9,-0.7) **-0.81**	(-0.2,-0.1) -0.16	(-0.9,-0.7) **-0.76**	(-0.9,-0.8) **-0.83**	(-0.9,-0.5) **-0.70**	(-0.9,-0.5) **-0.69**	(-0.7,-0.4) **-0.56**	(0.1,-0.1) -0.05	(-0.9,-0.9) **-0.88**	(-0.7,-0.9) **-0.80**	(-0.6,-0.5) **-0.57**	(**-0.8**,0.2) *	(-0.4,0.1) -0.15	(**-0.7**,0.2) *	(0.1,0.0) 0.04	(0.1,0.0) 0.04
14	(-0.7,-0.4) **-0.54**	(0.1,0.0) 0.03	(-0.8,-0.4) **-0.56**	(-0.6,-0.6) **-0.62**	(-0.9,-0.7) **-0.76**	(-0.2,-0.2) -0.16	(-0.9,-0.6) **-0.73**	(-0.9,-0.8) **-0.83**	(-0.9,-0.5) **-0.68**	(-0.9,-0.5) **-0.67**	(-0.8,-0.4) **-0.58**	(0.1,0.0) 0.01	(-0.8,-0.9) **-0.86**	(-0.7,-0.9) **-0.82**	(-0.6,-0.5) **-0.54**	(**-0.8**,0.3) *	(-0.4,0.3) -0.05	(**-0.8**,0.2) *	(0.2,0.2) 0.16	(0.1,0.2) 0.14
15	(-0.6,-0.1) -0.34	(-0.2,0.0) -0.07	(-0.6,-0.4) **-0.50**	(-0.7,-0.5) **-0.58**	(-0.7,-0.6) **-0.67**	(-0.3,-0.3) -0.30	(-0.8,-0.6) **-0.70**	(-0.6,-0.7) **-0.67**	(-0.8,-0.5) **-0.63**	(-0.8,-0.4) **-0.59**	(-0.4,-0.2) -0.28	(-0.2,-0.3) -0.24	(-0.6,-0.8) **-0.73**	(-0.5,-0.8) **-0.68**	(-0.7,-0.5) **-0.57**	(**-0.8**,0.2) *	(-0.6,0.1) -0.22	(**-0.7**,0.4) *	(-0.1,-0.2) -0.13	(0.0,-0.1) -0.05
16	(**-0.8**,0.1) *	(-0.1,-0.2) -0.16	(-0.6,-0.1) -0.35	(-0.7,0.3) *	(**-0.9**,0.3) *	(-0.3,0.0) -0.14	(**-0.9**,0.3) *	(-0.7,0.2) *	(**-0.8**,0.1) *	(**-0.9**,0.4) *	(-0.4,0.1) -0.13	(0.1,0.0) 0.05	(**-0.8**,0.1) *	(-0.6,0.2) -0.18	(-0.5,0.1) -0.15	(-0.8,-0.8) **-0.80**	(-0.7,-0.4) **-0.58**	(-0.5,-0.2) -0.36	(-0.4,-0.4) -0.37	(-0.4,-0.1) -0.26
17	(-0.8,-0.1) -0.43	(-0.1,0.0) -0.03	(-0.7,-0.1) -0.37	(-0.6,0.5) *	(**-0.9**,0.2) *	(-0.3,0.1) -0.08	(**-0.9**,0.3) *	(**-0.7**,0.2) *	(**-0.8**,0.1) *	(**-0.9**,0.4) *	(-0.5,0.0) -0.19	(0.1,0.0) 0.01	(**-0.7**,0.2) *	(-0.5,0.3) *	(-0.4,0.1) -0.14	(-0.7,-0.8) **-0.74**	(-0.7,-0.7) **-0.67**	(-0.4,-0.3) -0.35	(-0.4,-0.6) -0.50	(-0.4,-0.5) -0.48
18	(-0.6,0.3) *	(0.1,-0.4) -0.21	(-0.6,0.0) -0.26	(-0.6,0.5) *	(**-0.8**,0.5) *	(-0.5,0.2) -0.11	(**-0.9**,0.5) *	(-0.7,0.3) *	(**-0.8**,0.4) *	**0.8**,0.6) *	(-0.4,0.0) -0.18	(0.0,0.2) 0.13	(-0.7,0.3) *	(-0.6,0.3) *	(-0.4,0.2) -0.06	(-0.8,-0.6) **-0.72**	(-0.8,-0.3) **-0.54**	(-0.7,0.0) -0.34	(-0.4,-0.3) -0.35	(-0.3,0.1) -0.11
19	(-0.7,-0.4) **-0.55**	(-0.2,0.4) 0.14	(-0.5,-0.1) -0.30	(-0.4,0.0) -0.16	(-0.7,-0.2) -0.42	(-0.1,0.0) -0.05	(-0.6,-0.1) -0.36	(-0.6,-0.1) -0.30	(-0.6,-0.2) -0.42	(-0.7,-0.2) -0.41	(-0.5,0.1) -0.17	(0.1,-0.3) -0.09	(-0.6,0.0) -0.26	(-0.4,0.0) -0.13	(-0.4,-0.1) -0.21	(-0.4,-0.3) -0.33	(-0.3,-0.5) -0.41	(-0.1,-0.3) -0.18	(-0.3,-0.4) -0.33	(-0.4,-0.6) **-0.54**
20	(-0.6,-0.4) **-0.50**	(0.0,0.4) 0.22	(-0.4,-0.1) -0.22	(-0.2,0.0) -0.10	(-0.4,-0.3) -0.35	(0.1,-0.1) 0.01	(-0.3,-0.2) -0.27	(-0.4,-0.1) -0.21	(-0.3,-0.2) -0.23	(-0.4,-0.3) -0.33	(-0.4,0.1) -0.11	(0.3,-0.3) -0.05	(-0.4,-0.1) -0.2	(-0.2,0.0) -0.10	(-0.1,-0.2) -0.14	(0.0,0.0) -0.02	(0.0,-0.3) -0.14	(0.2,-0.1) 0.07	(-0.1,-0.3) -0.23	(-0.5,-0.7) **-0.61**
21	(-0.4,0.4) *	(-0.4,-0.4) -0.38	(-0.6,-0.1) -0.33	(0.0,0.1) 0.09	(-0.3,-0.1) -0.18	(-0.1,0.1) 0.04	(-0.3,0.0) -0.09	(-0.6,0.0) -0.29	(-0.5,0.2) -0.09	(-0.5,0.1) -0.13	(-0.6,0.0) -0.25	(-0.6,-0.4) **-0.51**	(-0.2,-0.1) -0.18	(-0.1,-0.1) -0.07	(-0.8,-0.3) **-0.53**	(-0.2,-0.4) -0.29	(-0.2,-0.2) 0.03	(-0.3,0.1) -0.11	(0.5,-0.3) 0.07	(0.4,0.1) 0.27

uptake at the end of the study (Table 2). Though starting values (Table 1) and changes in (Table 3) Mn^{2+} uptake in *light*-adapted outer retina ($\Delta R_{1,Light}$) were reasonably well-correlated with the those found in darkness and inner retina, starting values were poor predictors of later changes in $\Delta R_{1,Light}$ (Table 4,pt.2). A similar pattern was found for activity-dependent Mn^{2+} uptake, defined as the outer retinal dark-light difference ($\Delta R_{1,Dark}$ - $\Delta R_{1,Light}$). However, outer retinal $\Delta R_{1,Light}$ and activity-dependent Mn^{2+} uptake were poorly correlated in all cases. Relationships between Mn^{2+} uptake and the 'eye growth' variables were sometimes present in Group YM, but generally absent in Group MO — suggesting that, overall, intraretinal Mn^{2+} uptake is independent of eye size and growth.

The two measures of visual function (CS and SFT) showed distinct patterns, and were poorly correlated with one-another in all regression analyses. We first consider SFT: We found it was poorly correlated with all variables at the start of the study (Table 1). Rate of change in SFT was not significantly correlated with rate of change in any other variable (Table 3), or predicted by any starting variable (Table 4). We note that starting values for SFT were positively correlated with later measures of SFT (Table 2) — demonstrating that subject-to-subject differences in SFT were reasonably stable over time.

On the other hand, CS showed several significant relationships with eye morphology and Mn^{2+} uptake: High rates of 'eye growth' were *positively* correlated with changes in CS over time (Table 3) — rats which showed the largest increases in e.g. retinal surface area experienced the smallest CS declines. Measuring from the start to the end of the study, the rate of CS decline was significantly *negatively* correlated with starting values of most 'eye growth' variables (Table 4, pt.2) such that animals which started with the larger-than-average retinal surface areas (for instance) experienced the largest CS declines. A similarly strong relationship was found for

initial values of CS. Since initial CS was poorly correlated with most of the 'eye growth' variables at the start of the study (Table 1), we considered the possibility that they were independent predictors of CS decline: After statistically controlling for the influence of any one of the eye growth variables (e.g. axial length), initial CS remained a significant predictor of later declines ($P \leq 1.1e\text{-}3$), but the remaining eye growth variables typically were not ($P > 0.05$, except for posterior lens rC, which yielded $0.05 > P > 0.025$ when controlling for either retinal volume or body weight). Testing in the reverse order — statistically controlling for the influence of initial CS, then evaluating whether any of the eye growth variables remained significant predictors of CS decline — yielded uniformly positive results (all $P \leq 0.021$). From these *post-hoc* multiple regression analyses, we conclude that initial CS and initial retinal surface area are the strongest pair of predictors for rate of CS decline from the start to the end of the study, accounting for ~60% of the variance in rate of CS decline. In that model ($F_{[2,25]}=18.5$, $P=1.19e\text{-}5$, multiple $R^2=0.596$), initial CS uniquely accounts for ~28% of the variance in rate of CS decline (squared semipartial correlation ('sr^2') = 0.281; $P=3.20e\text{-}4$) while initial retinal surface area uniquely accounts for another ~15% of the variance in rate of CS decline ($sr^2=0.147$, $P=5.80e\text{-}3$). The remaining (60% - 28% - 15% =) ~17% of the variance is accounted for by either variable (e.g. when only initial retinal surface area is used to predict rate of CS decline, $P=1.87e\text{-}3$, $R^2=0.316 \approx (15\%+17\%)$). In short, those animals which showed the largest CS declines were those which began with larger-than-average retinal surface area (and other 'eye growth' measures described above), or better-than-average CS, and declined most with a combination thereof.

The above correlations with rate of CS decline were generally weaker when evaluating declines over a shorter time period in Group MO (Table 4, pt.1). In those analyses, Group MO

declines in CS were calculated between the starting (~7 mo) and intermediate (~11.5 mo) time points, instead of the yearlong span between the start and end of the study. Of note, those analyses revealed that *high retinal Mn^{2+} uptake was the strongest predictor of CS declines in the ~4.5 mo after MRI scans*. The relationship between Mn^{2+} uptake and future CS declines was not evident when considering the trends over the yearlong study of Group MO (Table 4, pt.2) for the following reason: Those rats which declined rapidly from ages ~7 to ~11.5 mo tended to decline least from ~11.5 to ~19 mo. Mn^{2+} uptake in the inner retina and dark-adapted outer retina were thereby significant predictors of *preserved* CS from ~11.5 to ~19 mo (Table 4, pt.1), despite being significant predictors of *declining* CS in the ~4.5 mo following MRI scans. This complex relationship between CS and Mn^{2+} uptake, as well as the broader correlations with 'eye growth' variables are illustrated in Figure 6.

Considering both Group YM and Group MO together, several starting measurements were significant predictors of CS decline in the ~4.5 mo following MRI (Table 4, pt.1): body weight, anterior lens rC, initial CS, as well as Mn^{2+} uptake in the inner retina, dark-adapted outer retina, light-adapted outer retina, and the dark-light difference in outer retinal Mn^{2+} uptake. Since several of these variables were significantly correlated (Table 1) we used multiple regression to gauge the importance of each: The strongest predictor of CS decline was Mn^{2+} uptake in the dark-adapted outer retina (P=1.24e-6; R^2=0.55). After controlling for this relationship, only initial CS remained a significant predictor of CS decline (P=3.51e-4; for the other five variables, P>0.05). The model with those two independent variables accounted for ~71% of the variance in CS declines (i.e., multiple R^2=0.71), which was statistically similar (P=0.38) to a model including all seven independent variables (multiple R^2=0.77). The failure of the five other variables (e.g. body weight) to improve predictions of CS decline in those models argues that

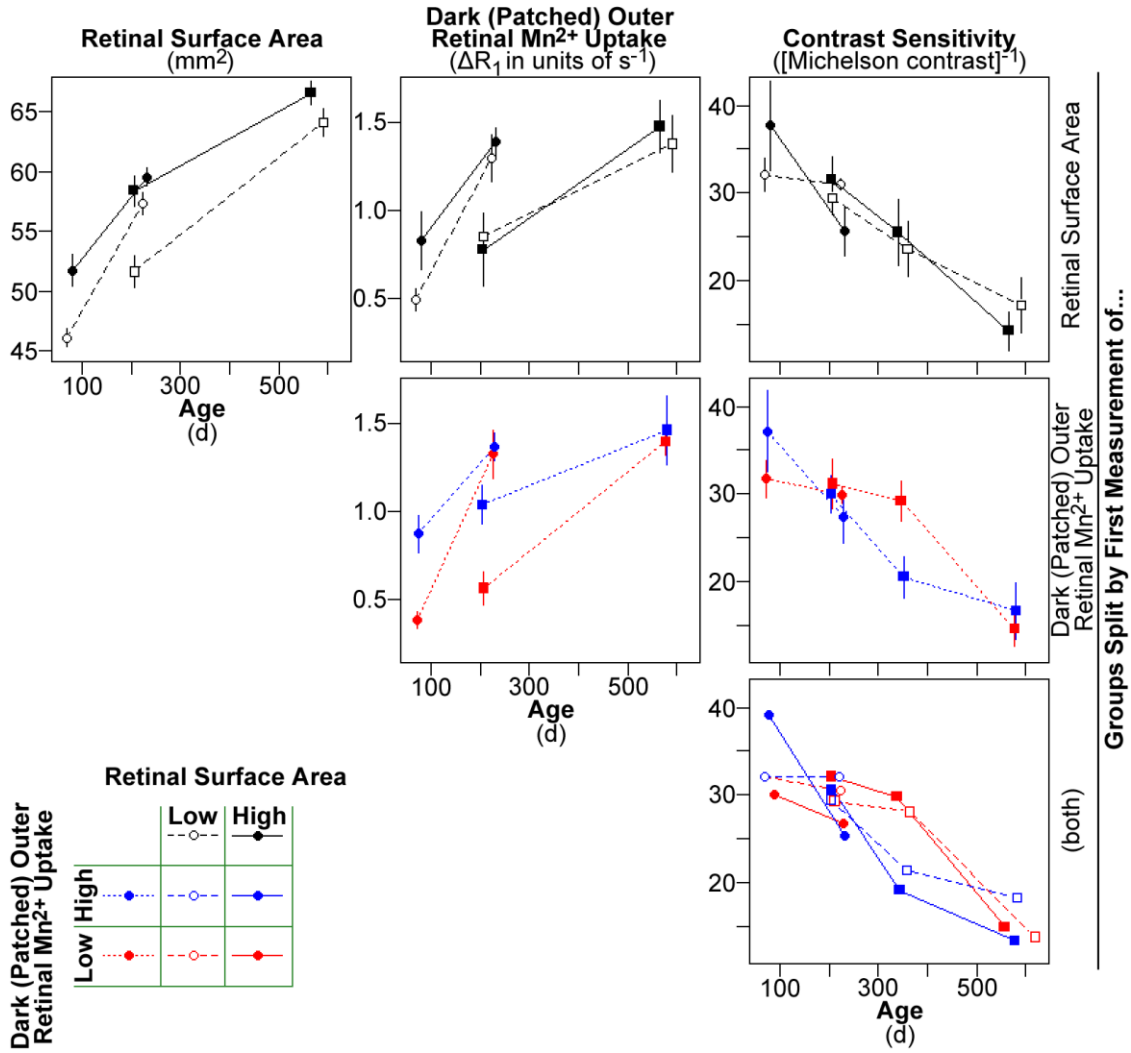

Figure 6: Visualization of regression results linking initial morphological and physiological measurements to subsequent CS declines. In these plots, groups are split based on whether an animal's first measurement (at age ~2.5 mo for Group YM (circles); at age ~7 mo for Group MO (squares)) was higher or lower than the median value for that group at that time. Note that these splits are intended for visualization purposes only: Because distributions were roughly normal in all cases, these high/low categories were *not* used in formal statistical comparisons, which were performed with linear regression (see Tables 1-4). Only animals which were studied longitudinally (i.e., vision tested ~4.5 mo after the first measurement) were used to calculate medians, or the means ±SEM plotted for each sub-group (note that, for clarity, the lower right panel omits error bars). In terms of the patterns shown here, retinal surface area is representative of most other morphological measures: Its starting values and rates of change were correlated with starting values and rates of change for most other morphological measures (Tables 1,3,4). The slopes of connecting lines are of critical importance in these plots, representing rates of change described in Tables 3 and 4. *Top Left*: Rats starting with relatively (for one's age) low surface area experience significantly greater growth over the course of the study (steeper slopes on dashed than solid lines; Table 4,pt.2) but still end our studies with lower surface area (Table 2). *Top Center:* There are no consistent relationships between starting surface area and starting values of, or rates of change in, retinal Mn^{2+} uptake (Tables 1 and 4). *Top Right:* Measuring from the first to the final time point for each group, rats starting with higher surface areas experience significantly greater CS declines (steeper slopes on solid than dotted lines; Table 4). *Center*: Rats starting with relatively low Mn^{2+} uptake area experience significantly greater increases in Mn^{2+} uptake over the course of the study (steeper slopes on red than blue; Table 4,pt.2). Levels of Mn^{2+} uptake converge so much over time that starting and ending values are not correlated (Table 2). *Center Right*: In the ~4.5 mo after MRI scans, rats starting with high Mn^{2+} uptake showed significantly steeper CS declines (steeper slopes for blue than red; Table 4,pt.1), but from ~4.5 to ~12 mo after MRI scans, the opposite pattern was seen in Group MO (squares). *Bottom Right:* The patterns at Top Right and Center Right are present when splitting data by both Mn^{2+} uptake and surface area, arguing that they are relatively independent processes. In Group MO (squares), ultimate (over 1 year) CS declines are predictable by starting surface area (solid lines steeper than dashed), but the tendency to decline immediately (within ~4.5 mo of scan; blue lines) versus retain function until a later eventual decline (from ~4.5 mo to ~12 mo; red lines) is predicted by starting Mn^{2+} uptake, regardless of starting surface area.

their correlations with CS decline (Table 4, pt.1) are a byproduct of their significant relationships with dark-adapted outer retinal Mn^{2+} uptake (Table 1). We note that the relationship between initial CS and later CS declines cannot account for the relationship between Mn^{2+} uptake and CS declines: After statistically controlling for the relationship with initial CS, each of the Mn^{2+} uptake variables remains a significant (P<1.36e-3) predictor of CS declines — with dark-adapted outer retinal Mn^{2+} uptake remaining the strongest of those four variables (P=2.13e-7). In short, Mn^{2+} uptake and initial CS are both strong and unique predictors of CS declines in the subsequent ~4.5 mo. This relationship is detailed in Figure 7.

Additional regression analyses were run to fully document the relationships between Mn^{2+} uptake and CS decline in the ~4.5 mo after MRI scans: As noted above, inner retinal Mn^{2+} uptake was not significant after controlling for the relationship with dark outer retinal Mn^{2+} uptake (P=0.88). However, the reverse was not true: Dark-adapted outer retinal Mn^{2+} uptake (as well as the dark-light difference) remained significant predictors of CS decline (P=2.81e-2 (and 3.58e-2, respectively)) even after controlling for the relationship to inner retina. These findings argue that dark-adapted outer retinal Mn^{2+} uptake is a superior predictor of CS declines, and we therefore tried to differentiate between the activity-dependent (i.e. dark-light difference) and other (light-adapted Mn^{2+} uptake) components of Mn^{2+} uptake in the dark-adapted outer retina. However, regression analyses including both light-adapted Mn^{2+} uptake and the dark-light difference showed that each variable was a significant and unique predictor of CS decline, either when statistically controlling for the relationship with initial CS (both P≤1.72e-4) or not (both P≤6.64e-4).

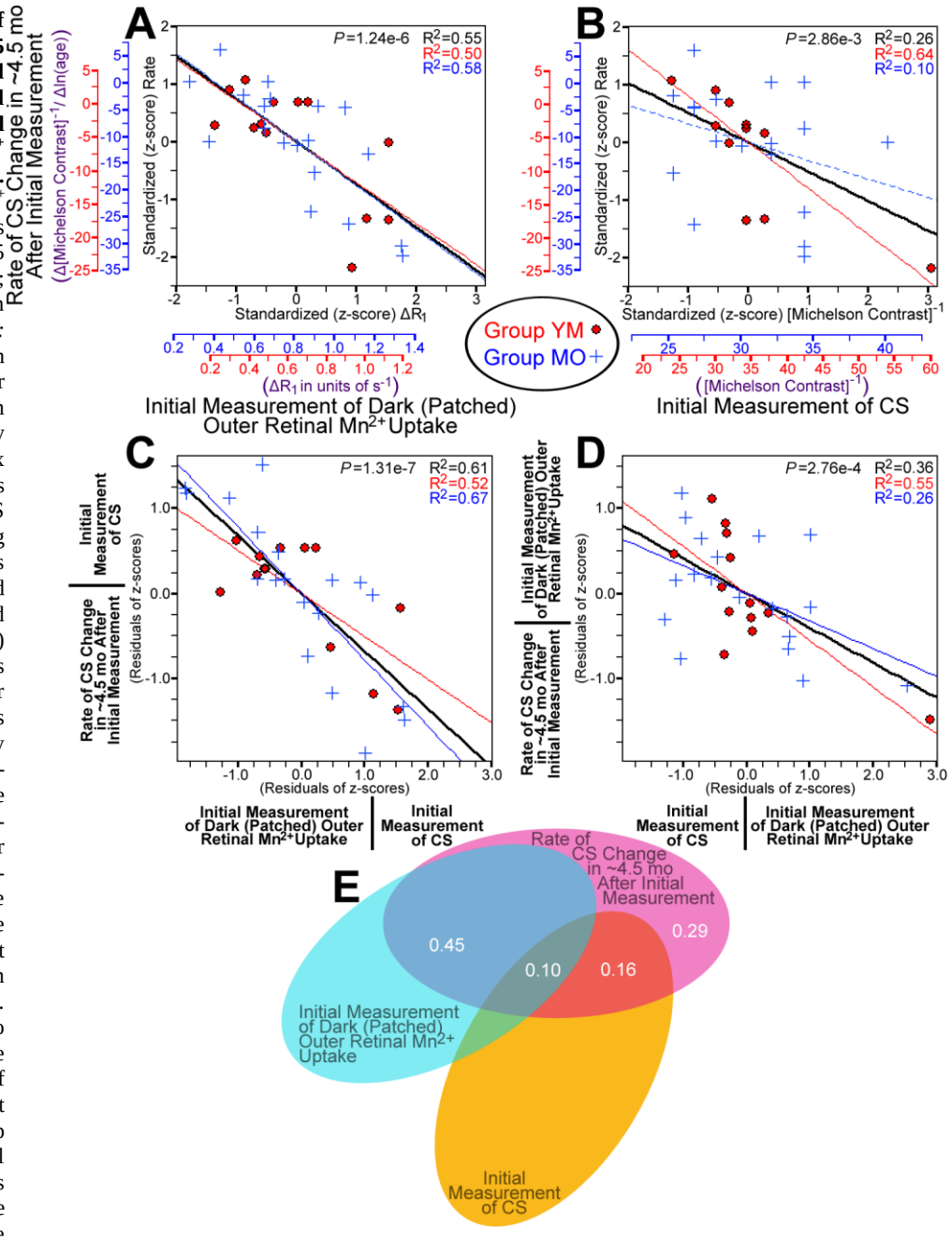

Figure 7: Prediction of CS declines in the ~4.5 mo after the initial MRI by both initial level of dark-adapted outer retinal Mn^{2+} uptake and initial CS. Initial CS and Mn^{2+} uptake measurements were made at age ~2.5 mo in Group YM (red; •) and age ~7 mo in Group MO (blue; +). *A):* Greater Mn^{2+} uptake in the dark-adapted outer retina — when photoreceptors are fully depolarized and ion flux is greatest — predicts greater rates of CS decline in the following ~4.5 mo. As with Tables 1-4, the combined analysis (black line and scales, p-value, R^2) showing this effect is performed after standardizing values from each group by converting them into z-scores. The red and blue axes show the pre-standardized values for Mn^{2+} uptake (ΔR_1; x-axis) and rate of change in CS (change in inverse Michelson contrast divided by change in log-transformed age). Note that the ~4.5 mo time span covered here is ~ 1 natural log-unit of age for Group YM, but only ~0.5 for Group MO. Although formal statistical testing was restricted to the combined analysis, we also show R^2 values and best-fit lines (solid lines indicate $P<0.05$) for each group separately. *B):* Higher initial CS values predict greater rates of CS decline in the following ~4.5 mo. Layout of axes is similar to that of *A*. *C):* Even after statistically controlling for the effect of initial CS — y-axis values in this plot are the residuals from the combined (black line) best-fit in *B* — greater Mn^{2+} uptake in the dark-adapted outer retina strongly predicts greater rates of CS declines in the following ~4.5 mo. *D):* Even after statistically controlling for the effect of greater Mn^{2+} uptake in the dark-adapted outer retina, initial CS strongly predicts greater rates of CS decline in the following ~4.5 mo. *E):* Venn diagram showing the proportion of variance in rate of CS decline that is uniquely explained by dark-adapted outer retinal Mn^{2+} uptake (semipartial correlation ('sr^2') = 45%) or initial CS ('sr^2' = 16%), of the total ~71% of variance which can be explained by some combination of those two variables. Note that R^2 values in *A* through *D* can be derived from this diagram, for instance: The unique 45% explained by Mn^{2+} uptake plus 10% shared with initial CS combine to yield the R^2 of 0.55 in *A*. Controlling for the effects of Mn^{2+} uptake to make plot *D* is visualized by removing the 0.45 and 0.10 regions from the diagram, leaving only the variance that could *not* be explained by Mn^{2+} uptake. Of that remaining (0.16+0.29=)45%, (0.16/(0.16+0.29)=)36% is explained by initial CS, as reflected by R^2=0.36 in *D*.

CHAPTER 3

ARM 2: EFFECTS OF L-VGCC BLOCKADE ON RETINAL Mn^{2+} UPTAKE IN YOUNG ADULTS

3.1 Rationale

Arm 2 experiments were carried out to better-understand the role of L-VGCCs in Mn^{2+} uptake, which seems to be an important predictor of vision decline, based on Arm 1 results. We measured retinal Mn^{2+} uptake in young adult rat retinas with and without exposure to the dihydropyridine L-VGCC blocker nifedipine. To test the hypothesis that L-VGCC blockade inhibits the activity-dependent component of retinal Mn^{2+} uptake, we used an eye patch to expose one eye to normal lab lighting while the other remained dark-adapted. The well-documented (e.g., Berkowitz et al., 2009; Berkowitz et al., 2006; Bissig & Berkowitz, 2011) dark-light difference in outer retinal Mn^{2+} uptake is due to the full depolarization of photoreceptors in darkness, but relative hyperpolarization in light (for review, see Yau, 1994). In addition to verifying this effect in vehicle-injected controls, we tested whether systemic (intraperitoneal) nifedipine attenuated outer retinal activity- (i.e. light-) dependent Mn^{2+} uptake. In a second experiment, nifedipine eye drops were administered to only one eye of binocularly dark-adapted rats. Mn^{2+} uptake was compared in vehicle-treated versus nifedipine-treated eyes. Positive results from that experiment would indicate that the effect of L-VGCC blockade on retinal Mn^{2+} uptake is not an artifact of systemic effects.

3.2 Methods

All aspects of these experiments — for instance, the rat strain, eye patch procedure, Mn^{2+} doses, MRI equipment, procedures, and image processing, including the use of averaged baseline (no Mn^{2+}) data collected for Arm 1 to calculate ΔR_1s — are identical to those in Arm 1 unless otherwise noted.

3.2.1 Intraperitonal Nifedipine: The influence of nifedipine on retinal Mn^{2+} influx was tested in both light- and dark-adapted eyes using two groups of young-adult rats. After a patch was applied to one eye of each rat (the right eye for four members of each group), animals were dark-adapted overnight. The following day, rats were monocularly exposed to normal lab lighting (~300 lx). Immediately after beginning light exposure, drug-treated rats (n=8; 264(20) g; aged 63(3) d) were injected with nifedipine (30 mg/kg body weight) dissolved in DMSO (20 mg nifedipine / ml of undiluted dimethyl sulfoxide), and vehicle-control rats (n=6; 259(57) g; aged 63(9) d) were injected with DMSO only (1.5 ml/kg body weight). Each rat was injected with Mn^{2+} 31(2) min later, then maintained in normal lab lighting until immediately before MRI scanning, when rats were anesthetized with k/x solution (8.3(2.6) and 8.3(2.3) ml/kg, respectively, in drug-injected and control rats) immediately followed by removal of the eye patch and scanning of the left, then right, eyes (respectively 4.3(0.2) and 5.5(0.2) hr after Mn^{2+} injection in drug-injected and 4.4(0.3) and 5.6(0.3) hr in controls). Some data collected for this experiment has been published previously (Berkowitz et al., 2011).

3.2.2 Topical Nifedipine: The influence of nifedipine eye drops on retinal Mn^{2+} influx was tested in five dark-adapted young adults (330(18) g; aged 80(2) d). Undiluted PEG400 (polyethylene glycol with an average molecular weight of 400 daltons; Sigma-Aldrich; St. Louis, MO) was used as a vehicle for the extremely hydrophobic nifedipine. PEG400 is nonirritating when applied to rabbit eyes and in alternative assays (ECETOC, 1998; Adriaens et al., 2005) and otherwise has low potential for toxicity (Smyth et al., 1950). Nifedipine (Sigma-Aldrich; St. Louis, MO) was expected to be similarly nonirritating (Gonzalez et al., 1993). Although temporary reductions in intraocular pressure have been reported following topical nifedipine administration in rabbits, they are similar to reductions measured in an untreated contralateral

eye, or in animals exposed only to vehicle (Segarra et al., 1993; Payne et al., 1990). Nifedipine was dissolved in warm (40-45°C) PEG400 to produce high-concentration (0.211 M) eye drops, which were aliquoted and stored at -80°C until use. Along with a sample of identically-treated vehicle (PEG400 only), aliquots were thawed at room temperature before application to the eyes. All additional procedures took place under dim red light or darkness. After anesthetizing the rat with diethyl ether, six 50 µl drops of nifedipine in PEG400 were applied to one eye (the right in 3 of 5 subjects; ~1 min between each drop), and six 50 µl drops of PEG400 only were applied to the contralateral eye. Rats were injected with Mn^{2+} 38(2) minutes after nifedipine exposure (ensuring full recovery from anesthesia). Rats were scanned ~4hr later (left and right eye respectively at 4.0(0.3) and 5.3(0.5) hr post-Mn^{2+}) immediately after being anesthetized with urethane (3.7(0.3) ml/kg of a 36%w/v solution in 0.9% saline; Sigma-Aldrich, St. Louis, MO). Only dark-adapted retinas were studied in this experiment; eye patches were never applied to these rats.

3.2.3 Statistics: Multiple *in vitro* (Carlson et al., 1994; Drapeau & Nachshen; 1984) and *in vivo* (Cross et al., 2007; Berkowitz et al., 2007b) studies have demonstrated that L-VGCC blockade inhibits neuronal Mn^{2+} uptake. In addition, several previous studies, both *in vivo* with MEMRI (Berkowitz et al., 2006; Berkowitz et al., 2009; Bissig & Berkowitz, 2011; Tofts et al., 2010) and *ex vivo* (e.g. Morjaria & Voaden, 1979; see Yau 1994 for review), have demonstrated that the outer retina is more active and ion permeable in dark than light. For these reasons, we initially analyzed Mn^{2+} uptake (ΔR_1) with one-tailed t-tests (patched > unpatched; control > nifedipine; $\alpha = 0.05$). ANOVAs and meta-analytic methods were used to aid in the interpretation, as detailed alongside exact p-values in the Results section.

3.3 Results

3.3.1 Intraperitonal Nifedipine: For the *inner* retina, paired t-tests showed that dark and light conditions were similar in vehicle-control rats (P=0.832), and in nifedipine-treated rats (P=0.569). This is consistent with Arm 1 results, showing that dark and light are similar in inner retina (Fig.4). Mn^{2+} uptake non-significantly trended lower in nifedipine-injected than in vehicle-control rats, for both light-exposed and dark-adapted (patched) inner retina (P=0.128 and 0.0573, respectively). When assessed with a two-way (light vs. dark × drug vs. vehicle) mixed ANOVA, the drug effect was suggestive (see below; $F_{[1,12]}$=3.15; P=0.101) but none of the results reached significance ($F_{[1,12]}$<0.59; P>0.45 for both the light effect and interaction). These results are summarized in Figure 8.

For the *outer* retina, vehicle-control rats showed more Mn^{2+} uptake in dark than light (P=0.0181; Fig.8), but nifedipine-treated animals did not (P=0.571). Other comparisons suggested this was due to inhibition of activity-dependent Mn^{2+} uptake by nifedipine: Comparing nifedipine-injected to vehicle-control rats, outer retinal Mn^{2+} uptake was inhibited in dark-adapted (patched) (P=0.0418; Fig.8) but not light-exposed eyes (P=0.524). This activity- (i.e., light-)dependent drug effect was further suggested by significant drug vs. vehicle differences in ratio ($\Delta R_{1,dark}/\Delta R_{1,light}$) and difference ($\Delta R_{1,dark}-\Delta R_{1,light}$) scores ($P$=0.0430 and 0.0257, respectively, two-tailed unpaired t-tests; Fig.8). (The latter point is similarly described by a significant (light vs. dark × drug vs. vehicle) interaction in a mixed ANOVA ($F_{[1,12]}$=6.48; P=0.0257).)

3.3.2 Nifedipine Eye Drops: Paired t-tests (nifedipine- vs. vehicle-treated eye) failed to show an effect of nifedipine on Mn^{2+} uptake in the inner retina (P=0.379) but revealed a significant effect at the outer retina (P=0.0312). In these dark-adapted outer retinas, Mn^{2+} uptake

in nifedipine-treated eyes was (mean±SEM) 82±6% that in vehicle-control eyes (calculated as $\Delta R_{1,nifedipine}/\Delta R_{1,vehicle}$; P=0.0221 for difference from 100%). These results are shown in Figure 9.

3.3.3 A Note on the Inner Retina: Somewhat surprisingly, neither experiment found a significant effect of nifedipine on *inner* retinal Mn^{2+} uptake. It's plausible that the relatively small sample sizes used in each experiment contributed to these negative findings. We therefore reexamined the data: Taking advantage of the fact that both experiments test the same general hypothesis, their results can be meta-analytically combined. This produces an outcome consistent with expectations: Using the Z-transform method, weighted by degrees of freedom ('df') (Whitlock, 2005), the ANOVA main effect for drug (P=0.101;df=12) and the test comparing eye drops (P=0.379;df=4) combine to produce a significant (P=0.0493) demonstration that inner retinal Mn^{2+} uptake is inhibited by nifedipine. Reassuringly, assessment with a different channel blocker (see Arm 3) supports this finding.

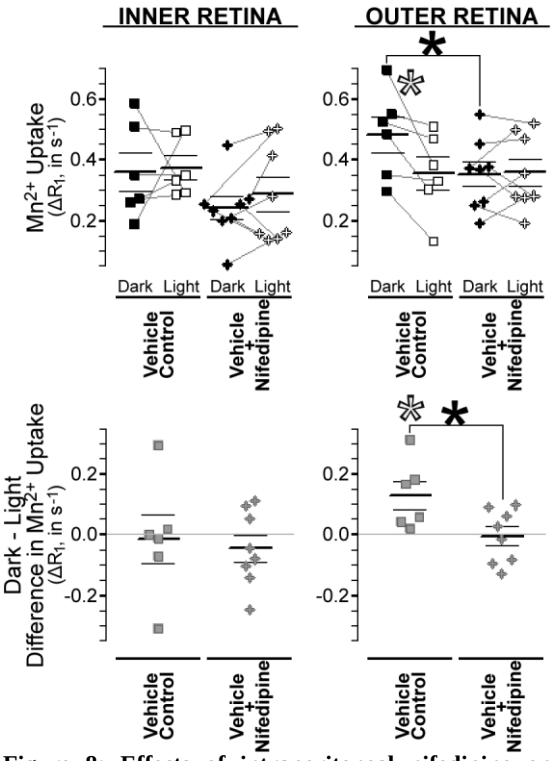

Figure 8: Effects of intraperitoneal nifedipine on retinal Mn^{2+} uptake. *Top:* Scatter plots show Mn^{2+} uptake in the inner and outer retina from both eyes of control (□) and nifedipine-treated (+) rats. Values from the dark-adapted ('dark'; patched) eye of each subject are connected by gray lines to the values from the contralateral eye, which was exposed to normal lab lighting ('light'; unpatched) during the period of Mn^{2+} accumulation. As in previous figures, mean±SEM are indicated by the thick and thin horizontal lines overlaid on each scatter plot. Consistent with expectations (and Arm 1 studies, see Fig.4) inner retinal Mn^{2+} uptake was similar in light and darkness and — in controls only — outer retinal Mn^{2+} uptake was higher in dark than light (P<0.05; open *). Outer retinal Mn^{2+} uptake was inhibited by nifedipine, but only in darkness (P<0.05; closed *) when photoreceptors are fully depolarized, thereby allowing ion flux through L-VGCCs (Yau, 1994). *Bottom:* The difference in Mn^{2+} uptake in dark versus light is shown. As indicated in *Top*, these dark-light differences are greater than zero (horizontal grey line) for only the control outer retina (P<0.05; open *). The dark-light difference is significantly higher in control than nifedipine-treated rats (P<0.05; closed *). The ability of nifedipine to suppress activity-dependent outer retinal Mn^{2+} influx strongly argues that (at least) this portion of the total Mn^{2+} uptake occurs through L-VGCCs.

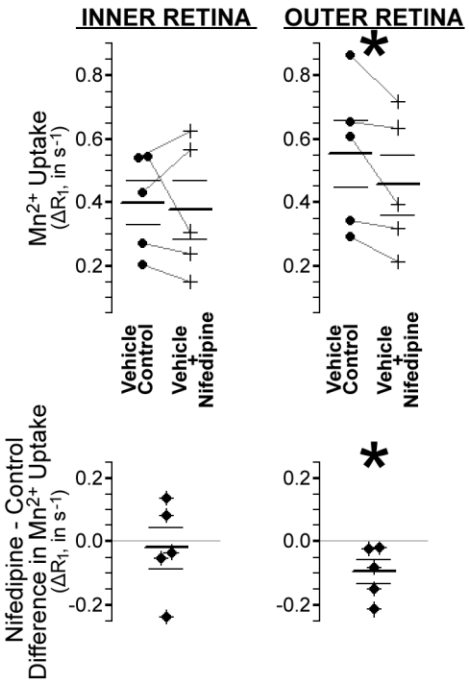

Figure 9: Effects of topical nifedipine on dark-adapted retinal Mn^{2+} uptake. *Top:* Scatter plots show Mn^{2+} uptake in the inner and outer retina from the nifedipine-treated eye of each rat connected by gray lines to the partner, vehicle-treated, control eye. As in previous figures, mean±SEM are indicated by the thick and thin horizontal lines overlaid on each scatter plot. Outer retinal Mn^{2+} uptake is significantly inhibited by nifedipine exposure (* P<0.05). *Bottom:* Differences between control and nifedipine-treated eyes are plotted, again showing that dark-adapted outer retinal Mn^{2+} uptake is significantly inhibited by topical nifedipine exposure (* P<0.05 for difference below zero (horizontal grey line)).

CHAPTER 4

ARM 3: TESTING FOR ISOFORM-SPECIFIC CHANGES IN L-VGCC EXPRESSION

4.1 Rationale

Results from Arms 1 and 2 demonstrated that retinal Mn^{2+} uptake — including the activity-dependent dark-light difference — increased with age, and was inhibited by L-VGCC blockade. Based on these findings, we hypothesized that the retina was experiencing an age-related increase in L-VGCC expression. By analogy to the aging rat hippocampus — where Veng and Browning (2002) demonstrated an age-related increase in expression of the ~180 kDa isofrom of α_{1D}, but not of the larger (>200 kDa) α_{1D} isoform or α_{1C} levels — an isoform-specific change in expression was expected.

Based on *ex vivo* studies, the concentration of L-VGCC antagonist needed to achieve half-maximum inhibition of current through α_{1D} channels is roughly an order of magnitude higher than for α_{1C}, both with dihydropyridine (Xu & Lipscombe, 2001; Koschak et al., 2001) and non-dihydropyridine antagonists including diltiazem and verapamil (Tarabova et al., 2007). If retinal α_{1D} expression increases with age, pharmacological inhibition of Mn^{2+} uptake through L-type channels should become more difficult with age — at least at lower drug doses. To our knowledge, the differential sensitivity of the α_{1C} and α_{1D} isoforms has not been demonstrated with nifedipine (only related drugs in the same class). For this reason, we use the non-dihydropyridine L-VGCC blocker D-*cis*-diltiazem (i.e., the (+)-*cis* isomer) in this arm of the study. We have previously demonstrated progressive inhibition of retinal Mn^{2+} uptake following intraperitoneal doses (5 and 30 mg/kg) of this drug in young adult rats (Berkowitz et al., 2007a). Western blots were also performed to test for changes in L-VGCC expression.

4.2 Methods

4.2.1 Intraperitoneal Diltiazem Dose-Response: All aspects of this experiment — for instance, rat strain, Mn^{2+} doses, MRI equipment, procedures, and image processing, including the use of averaged baseline (no Mn^{2+}) data collected for Arm 1 to calculate ΔR_1s — are identical to those used in Arm 1 unless otherwise noted. Rats in this experiment were never fit with an eye patch; only dark-adapted eyes were studied.

Young adult (n=10, aged 72(2) d, weighing 287(26) g) and mid-adult (n=12, 202(20) d, 465(59) g) rats were dark-adapted overnight. The following day, they were injected with 10, 30, 50, 100, or 125 mg diltiazem (Sigma-Aldrich; St. Louis, MO; intraperitoneal injection of 1.4 ml of diltiazem mixed in 0.9% saline / kg body weight), and maintained in darkness until MRI scanning was complete. Rats were injected with Mn^{2+} 31(2) min after diltiazem injection. 4.0(0.3) hr after Mn^{2+} injection, the left eye of these dark-adapted rats was scanned under urethane anesthesia (see above; 3.6(0.8) ml/kg).

4.2.2 Western Blots: Retinal expression of two isoforms of the pore-forming subunit of L-VGCCs — α_{1C} and α_{1D} (i.e.$Ca_v1.2$ and $Ca_v1.3$, respectively) — was studied in young adult (n = 6; all age 59 d, weighing 267(9) g) and mid-adult rats (n = 6; 192 d; 532(53) g). Immediately after death via urethane overdose, the left retina was isolated from each rat and stored at -80°C. Later, samples were sonicated on ice in a nonionic denaturing urea buffer (6 M urea; 62.5 mM Tris-HCl; pH 6.8; 10% glycerol; 2% sodium dodecyl sulfate; 0.00125% bromophenol blue; and freshly-added 5% β-mercaptoethanol; Shah et al., 1995) and the protein content of each sample was determined by a dot blot protein assay (Henkel and Bieger, 1994) calibrated against bovine serum albumin (BSA). Aliquots of each sample were diluted with the urea buffer to 3µg protein / µl in preparation for SDS-PAGE. Samples were loaded (20 µl per lane) onto 6% polyacrylamide

separating mini-gels alongside size standards (Bio-Rad Dual Color Standards #161-0374). Bio-Rad mini-gel kits were used to separate proteins and transfer to membranes (#IPFL00010, Millipore). Membranes were blocked at room temperature in TST (10 mM Tris base and 145 mM NaCl in dH_2O, pH 8.0, mixed with Tween 20 (0.05%v/v)) containing 10%w/v non-fat dry milk and 3%w/v BSA, then incubated overnight at 4°C with primary antibodies — mouse anti-β actin (clone AC-15, #A5441, lot 030M4788, 1:10,000 dilution, Sigma-Aldrich) and either mouse anti-α_{1C} (clone L57/46, #73-053, lot 437-4VA-62, 1:4 dilution) or mouse anti-α_{1D} (clone N38/8, #73-080, lot 437-4VA-10, 1:4 dilution) — mixed into TST containing 5%w/v nonfat dry milk and 1.5%w/v BSA. The monoclonal anti-α_{1C} and anti-α_{1D} antibodies were obtained from the UC Davis/NIH NeuroMab Facility. The following day, blots were thoroughly washed in TST, then incubated for 1.5 hr at room temperature with the secondary antibody, horseradish peroxidase-linked sheep-anti-mouse IgG (#NA931V, lot 399402, 1:5000 dilution, GE Healthcare), mixed into TST containing 5%w/v non-fat dry milk and 1.5%w/v BSA. Blots were visualized using chemiluminescent horseradish peroxidase substrate (#WBKLS0500, Millipore) and imaged on a FluorChem E system (ProteinSimple, Santa Clara, California).

Blot chemiluminescence intensities were quantified in ImageJ. Intensities were normalized to a non-specific band common to both anti-α_{1C}- and anti-α_{1D}-exposed blots at ~60 kDa. Although we originally planned to use β-actin for normalization, we found that apparent β-actin expression was in gross excess of L-VGCC levels and was therefore not a reliable control for protein loading (Dittmer and Dittmer, 2006). For completeness, however, we note that no age differences were found for the apparent β-actin levels normalized to the non-specific band at ~60 kDa (P>0.39 with two-tailed t-tests; not shown).

4.2.3 Statistics: To test for age effects on diltiazem's inhibition of Mn^{2+} uptake, inner retinal (16-28%thick) and outer retinal (48-68%thick) ΔR_1 values were compared using multiple regression to test for effects of age (young vs. mid-adult), dose, and a dose × age interaction. Lower ΔR_1s were expected in younger rats (given Arm 1 results), and in rats given higher doses of diltiazem. A significant interaction would indicate that the relationship between diltiazem dose and Mn^{2+} uptake is modulated by age.

In an alternative statistical approach, we compared ΔR_1s of rats injected with relatively low (10 to 30 mg/kg) and high (≥100 mg/kg) doses of diltiazem to age-matched, dark-adapted (patched), control ΔR_1s from Arm 1: Young diltiazem-injected rats were compared to the young-adult data from Group YM, while the mid-adult diltiazem-injected rats were compared to the combined mid-adult data from Groups YM and MO. These comparisons allowed us to test whether low and/or high doses of diltiazem were effective, and to estimate %inhibition of Mn^{2+} uptake at each age. These comparisons of Mn^{2+} uptake were one-tailed (control > low-dose; control > high-dose; low-dose > high-dose) given the large body of previous work showing inhibition of Mn^{2+} uptake by L-VGCC blockers (e.g., Carlson et al., 1994; Drapeau & Nachshen; 1984; Cross et al., 2007; Berkowitz et al., 2007b). Due to the disparate subject numbers and variances in Arm 1 control versus diltiazem-treated rats (ratios ≥3.5), we used Welch's t-tests for these comparisons.

For Western blots, the direction of findings (higher expression in older rats) for the ~180 kDa isofrom of α_{1D} is predicted both by two previous studies in the rat hippocampus (Veng & Browning, 2002; Veng et al., 2003), and significant differences in diltiazem dose-response data (see Results). We therefore use one-tailed t-tests (mid > young adults, $\alpha = 0.05$) to test for age differences in expression (normalized chemiluminescence) of that protein. The other bands (α_{1C},

and α_{1D} banding at >200 kDa) are similarly tested, but serve as negative controls: Only the ~180 kDa α_{1D} isofrom is expected to change with age (Veng & Browning, 2002; Veng et al., 2003).

4.3 Results

4.3.1 Intraperitoneal Diltiazem Dose-Response: Multiple regression analysis of the *inner* retina showed that Mn^{2+} uptake (ΔR_1) was generally lower in young than mid-adult rats (*P*=7.32e-5) and lower with higher doses of diltiazem (*P*=3.19e-3). Consistent with expectations, we also found a dose × age interaction (*P*=1.30e-2). Follow-up testing for each age group showed that mid-adult ΔR_1 steadily declined with higher diltiazem doses (*P*=7.54e-4; r=-0.83; mean±SEM change in ΔR_1 per 100mg/kg diltiazem (slope) of -0.45±0.09) but young adult ΔR_1 was similar throughout the 10-125 mg/kg range of doses (*P*>0.6; r=-0.14; slope of -0.05±0.11). Comparison to Arm 1 data — i.e., to age-matched dark-adapted control data — demonstrated that the highest (≥100 mg/kg) doses of diltiazem significantly inhibited Mn^{2+} uptake in young adults (*P*=1.62e-2) by ~40±11% (estimated as $[1 - (\Delta R_{1,diltiazem} / \Delta R_{1,control})]$ and considering only the standard error of $\Delta R_{1,diltiazem}$). A similar effect was noted in mid-adult rats (*P*=7.36e-4; ~42±8%). The lowest (10 to 30 mg/kg) doses inhibited Mn^{2+} uptake in young rats (*P*=2.74e-2; ~45±14%), but had no effect in older rats (*P*>0.9). These results are summarized in Figure 10.

Multiple regression analysis of the *outer* retina showed that Mn^{2+} uptake was generally lower in young than mid-adult rats (*P*=1.60e-4) and lower with higher doses of diltiazem (*P*=0.0212). The dose × age interaction did not reach significance (*P*=0.0951). Follow-up testing for each age group showed that mid-adult ΔR_1 steadily declined with higher diltiazem doses (*P*=0.0143; r=-0.68; slope of -0.42±0.14) but young adult ΔR_1 was similar throughout the 10-125 mg/kg range of doses (*P*>0.5; r=-0.20; slope of -0.08±0.13). Comparison to Arm 1 data demonstrated that the highest (≥100 mg/kg) doses of diltiazem significantly inhibited Mn^{2+}

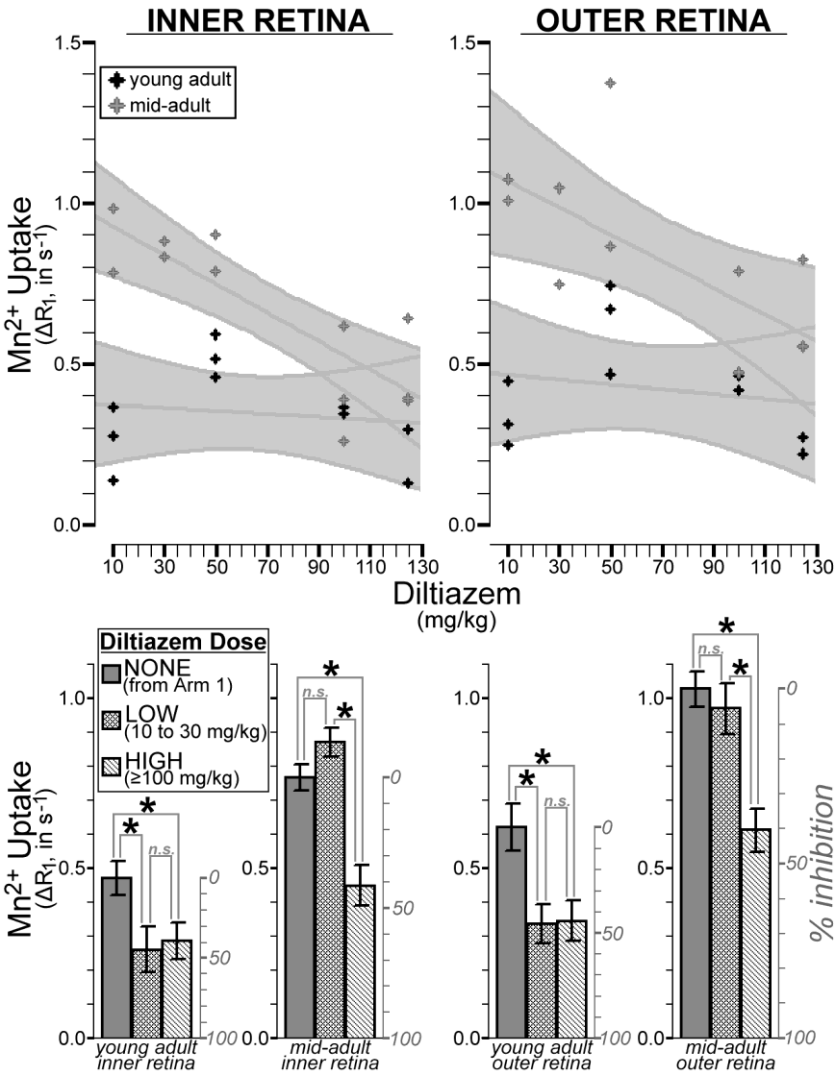

Figure 10: Diltiazem inhibition of retinal Mn^{2+} uptake in young and mid-adult rats. Data from both the inner retina (*Left*) and outer retina (*Right*) are shown. *Top:* Scatter plots, with best-fit lines (±95%C.I.) for young and mid-adults in the background, showing that progressively higher doses of diltiazem are correlated with progressively less Mn^{2+} uptake (i.e., greater inhibition; $P<0.05$) in mid-adults, but have little effect in young adults ($P>0.05$). Note that two pairs of mid-adult data points for the outer retina overlap: one pair at 100 mg/kg (ΔR_1s of 0.471 and 0.475) and one at 125 mg/kg (ΔR_1s of 0.551 and 0.556). *Bottom:* Retinal Mn^{2+} uptake in diltiazem-injected rats is compared to uptake in age-matched rats from Arm 1, which were never exposed to diltiazem. The right y-axis for each plot shows %inhibition, calculated as $[1 - (\Delta R_{1,diltiazem} / \Delta R_{1,control})]$, such that Arm 1 data (which serves as a control for diltiazem injection) is set to zero. In young adults, diltiazem significantly inhibits Mn^{2+} uptake (* $P<0.05$) at both low and high doses: Beyond the ~40% inhibition seen with the low dose, no additional inhibition is seen with high doses ('n.s.' indicates not significant; $P>0.05$). In mid-adults, low doses of diltiazem showed no effect on Mn^{2+} uptake, but high doses yielded significant (* $P<0.05$; ~40%) inhibition of Mn^{2+} uptake. Taken together, these data suggest that there is an age-related decrease in sensitivity to L-VGCC blockers, though with high-enough doses, maximum inhibition is still possible. This pattern is consistent with an age-related increase in the α_{1D} isoform of L-VGCCs, which is roughly an order of magnitude less-sensitive to diltiazem than the α_{1C} isoform (Tarabova et al., 2007).

uptake in young adults (*P*=4.72e-3) by ~44±9%. A similar effect was noted in mid-adult rats (*P*=1.07e-4; ~40±6%). The lowest (10 to 30 mg/kg) doses inhibited Mn^{2+} uptake in young rats (*P*=5.53e-3; ~46±9%), but had no effect in older rats (*P*>0.4; Fig.10).

4.3.2 Western Blots: Expression of α_{1D} was confirmed by the presence of specific banding (i.e., absent in partner anti-α_{1C} gels) at high molecular weight (~180 kDa and >240 kDa). The ~180 kDa variant was expressed more in mid-adult than young adult rats (*P*=0.0434), but this was not true of the >240 kDa variant (*P*>0.4) — consistent with aging patterns in the rat hippocampus (Veng & Browning, 2002; Veng et al., 2003). Aside from the non-specific band at ~60 kDa that was used for normalization, there was also modest α_{1D} labeling near ~120 kDa and between ~70 and ~90 kDa (not shown). For completeness, measurements were made from these bands. They showed no age differences when normalized to the ~60 kDa band, and normalizing α_{1D} bands to either of these (instead of the ~60 kDa band) had no effect on statistical conclusions for the >240 kDa (no effect of age) and ~180 kDa (mid>young) bands (not shown). Results are summarized in Figure 11.

Expression of α_{1C} was confirmed by the presence of specific banding at high molecular weight (~240 kDa). Consistent with expectations, similar α_{1C} expression was measured in young and mid-adults (*P*>0.2). However, we note that labeling of this band was fairly faint, plausibly making any age differences difficult to detect. Other qualitative patterns were noted for completeness: Although α_{1C} labeling for the rat brain typically shows a second high molecular weight band (~190 kDa; Westenbroek & Babcock, 1999; Iwamoto et al., 2004), this was not found in retina (Figure 11). Some banding was noted at ~45 kDa and ~100 kDa (not shown). Although α_{1C} labeling at ~100 kDa has been reported for other tissues (Callinan et al. 2005;

Westenbroek & Babcock, 1999), it is typically subtle or absent in rat brain (Ahlijanian et al., 1990; Iwamoto et al., 2004; Westenbroek & Babcock, 1999).

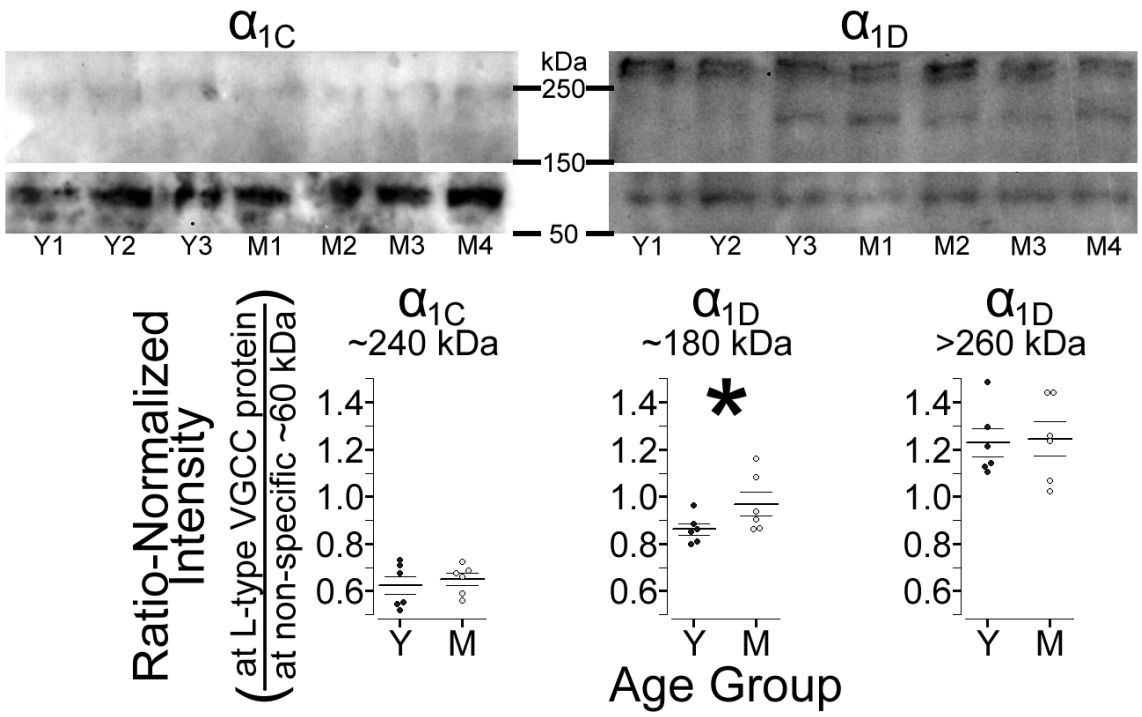

Figure 11: Western blots comparing α_{1C} and α_{1D} expression in retinas of young and mid-adult rats. *Top*: Representative anti-α_{1C} (left) and anti-α_{1D} (right) gels with lanes loaded with protein from 3 (of 6) young-adults (Y1-Y3) and 4 (of 6) mid-adults (M1-M4). For display purposes, images were cropped to highlight bands from of L-type channels at >150 kDa and the non-specific band used for normalization at ~60 kDa. The brightness and contrast settings differ for anti-α_{1C} (meant to display the fairly faint band at ~240 kDa) versus anti-α_{1D}, but are the same for the high and low molecular weight portions of each gel. Qualitatively, banding ≥240 kDa is similar in the two age groups, but the anti-α_{1D} band at ~180 kDa is clearly visible in all the mid-adult lanes shown here, but only one of the young-adult lanes. This is consistent with the expectation of greater expression of the ~180 kDa α_{1D} isoform in older rats (Veng & Browning, 2002; Veng et al., 2003). *Bottom:* Thick and thin horizontal lines indicate mean±SEM for the six data points plotted for each age group, which showed a difference in protein expression for only the ~180 kDa band of α_{1D} (* $P<0.05$). Since visual inspection of the ~180 kDa data suggested slight skewedness, that comparison of young to mid- adults was repeated with a one-tailed non-parametric test, yielding similar results ($P=0.0465$; Wilcoxon rank-sum test).

CHAPTER 5

ARM 4: ADDITIONAL MEASUREMENTS

5.1 Methods

5.1.1 Blood-Retinal Barrier (BRB) Integrity: After all other imaging procedures were finished, BRB was measured in five of the nine rats (2 young, 1 mid-, and 2 old adults) used to collect baseline (no Mn^{2+}) data in Arm 1. As in Berkowitz et al. (2004), BRB is measured by testing for vitreous enhancement in T_1-weighted images following tail vein injection of the vascular contrast agent Gd-DTPA (0.3 mmol/kg; Magnevist; Bayer HealthCare Pharmaceuticals, Leverkusen, Germany): Using the same hardware as for all other MRI scans reported here, 25 images of the eye were collected over a 37 min period using a standard spin-echo sequence (TR 1.0s, TE 11, 64 × 128 matrix, slice thickness 600 μm; 12 × 12 mm^2 field of view; 1 min 18 s acquisition time, 15 s pause between scans).The bolus of Gd-DTPA was injected through a tail vein between the fifth and sixth images.

A hand-drawn region of interest (ROI) was used to measure the mean signal intensity of all vitreous ('vSI') appearing in each image. For each subject, the pre-contrast signal intensity was calculated by averaging vSIs from the five pre-Gd-DTPA images ($vSI_{mean(pre)}$). Blood retinal barrier permeability surface area product (BRB PS) was calculated using vSIs from last three images of each subjects' series ($vSI_{mean(post)}$), the ROI volume (mean(SD): 2.9(0.4) mm^3), image repetition time (TR=1.0 s), and previously described methods and constants (a_1, a_2, m_1, m_2, vitreous T_1, and relaxivity of Gd-DTPA; Berkowitz et al., 2004).

5.1.2 Validation of SFT Measurements: Reproducibility of SFT measurements on our in-house device was assessed in 13 mid-adult rats (aged 206(14) d, weighing 458(67) g). Linear regression was used to compare each rat's SFT measurement (the maximum of 4 sessions) with a

second SFT measurement 14(10) d later. Late in the present studies, a commercial OKT system (OptoMotry; CerebralMechanics, Lethbride, Alberta, Canada) became available. We measured SFT of 9 young adult rats and 13 old adult rats using both the in-house and commercial systems (≤10 d between measurements). Shortly after this vision testing, the young adult rats were used for Arm 3 MRI studies, and old adult rats were used for the final time point in Arm 1. Linear regression was used to compare in-house and commercial measurements within each age group, and across all subjects.

5.1.3 Lifespan MRI Growth Curves: The MRI measurements described in Arm 1 produce a unique dataset cataloguing changes in eye morphology and physiology through much of the lifespan of Long-Evans rats. The corresponding growth curves for these measures are of some interest in their own right, providing a potentially useful baseline for studies in, for instance, transgenic or calorie-restricted rats (Guggenheim et al., 2004; Obin et al., 2000). Refractive state, derived from our measurements of optical media, is of some additional interest since previous measurements in adult rats differ substantially: While behavioral testing (Wiesenfeld & Branchek, 1976) suggests adult rats are myopic, retinoscopic (Massof & Chang 1972; Hughes, 1977; Mutti et al., 1992) measurements, as well as single-unit recordings from the optic nerve (Hughes, 1977), argue for hyperopia in adulthood. Age-related changes in refractive state during young adulthood may help account for inter-study variability. Growth curves were constructed using MRI data from control (Arm 1) rats, combined with a small set of juvenile control rats (aged 14-53 d; for details, see Supplemental Material in Appendix A), most of which were used in previous studies (Berkowitz et al., 2011; Chui et al., 2011).

5.2 Results

For each of the following, plots and further details are provided as Supplemental

Information in Appendix A.

5.2.1 Blood-Retinal Barrier (BRB) Integrity: All subjects had passive blood retinal barrier permeability surface area products less than 0.22 (10^{-5} cm^3/min). Since this is not higher than previously-collected control data (Berkowitz et al., 2004) it argues that the BRB was fully intact in every subject. No relationship between permeability and age was found with linear regression (r=0.03; *P*=0.97).

5.2.2 Validation of SFT Measurements: Test-retest reproducibility of SFT measurements from the in-house system was good (r=0.70; *P*=7.48e-3; mid-adults), and showed no change in acuities in the short time between test and retest (*P*=0.296; paired two-tailed t-test). SFT measurements from the in-house and commercial systems were well-correlated within young adult (r=0.70; *P*=0.0360) and old adult groups (r=0.75; *P*=3.01e-3)(combined: r=0.82; *P*=3.56e-6).

5.2.3 Lifespan MRI Growth Curves: Age-related increases were characterized for all variables except retinal thickness, which decreased with age, and vitreous chamber depth, which showed no consistent change with age. In most cases, logarithmic models reasonably approximated growth, except for predicting larger optical components (e.g. lens thickness, rC) for old-adults than was measured presently. In this regard, Weibull models offered a superior fit. Age-related increases in body weight, refractive state, retinal volume, and retinal Mn^{2+} uptake appeared sigmoid in Weibull models, with inflection points appearing in young or mid-adulthood.

CHAPTER 6

DISCUSSION

In these studies, we developed and applied, for the first time, a unique combination of behavioral, morphological, and physiological measures to examine the normal aging rat eye. The major findings from each arm are as follows: (1) In Arm 1, we demonstrated progressive age-related declines in contrast sensitivity ('CS'), as well as progressive age-related increases in retinal Mn^{2+} influx and eye size. Declines in SFT (a proxy for acuity) leveled off after ~7 mo and were not well correlated with any structural or physiological measurements. Importantly, relative to measurements from other rats in the same cohort, high Mn^{2+} influx in the dark-adapted outer retina was the best predictor of CS declines in the ~4.5 mo following MRI scans. When measuring CS declines over a broader time period — from the start to the end of our studies — rats beginning the study with a large eye (relative to other rats in the same cohort) experienced significantly greater CS declines. (2) In Arm 2, we demonstrated Mn^{2+} uptake in the dark-adapted outer retina was similarly inhibited by both systemic and topical exposure to the L-VGCC blocker nifedipine. (3) In Arm 3, we demonstrated age-related and isoform-specific increases in L-VGCC expression: Inhibition of retinal Mn^{2+} uptake by diltiazem was age-dependent, requiring more drug in mid-adult than young-adult rats. This pattern, observed *in vivo*, was consistent with greater expression of the relatively drug-insensitive α_{1D} isoform in mid-adult rats — a finding confirmed *ex vivo* with Western blots. These findings are discussed in more detailed below.

In Arm 1, age-related declines in visual function were heterogeneous: SFT declined from young to mid-adulthood, and then leveled off. In contrast, CS declined progressively over all age spans tested. Neither starting values (Table 1) nor rates of change (Table 3) in CS were

correlated with SFT. This disparity argues that CS declines are independent of pre- and post-retinal factors with potential to diminish both CS and SFT (e.g. very poor optics, motor function). Owing to that same disparity, poor correlations between SFT and our MRI measurements might be expected, given the strong correlations found between the same MRI measurements and CS declines. Indeed, both starting values and rates of change in SFT were poorly-correlated with measures of morphology and Mn^{2+} uptake (Tables 1 and 3). SFT measurements were nevertheless reliable, with repeated measurements collected over a short period being well-correlated, regardless of whether the in-house or commercial OKT system were used for the second measurement (see Appendix A for more detail). The finding that SFTs were well-correlated over broader age ranges (Table 2) and stable from mid- to old adulthood (Fig.5) similarly argues for the reliability of the measurement, and offers an explanation for the negative correlations to MRI measures: Almost every measure changes from mid- to old adulthood (Figs.4&5), ruling out any simple links with the relatively unchanging SFT. There nevertheless remained several opportunities to link the structural and physiological MRI measures to age-related vision declines, since progressive declines in CS were observed.

6.1 Structural Changes in the Aging Rat Eye

Consistent with several previous studies in pigmented rats, we found that the retina thinned throughout adulthood (Katz & Robison, 1986; Obin et al., 2000; Feng et al., 2007; Bissig & Berkowitz, 2011). By analogy to models of retinal degeneration, where more-dramatic retinal thinning is caused by cell loss — we considered the possibility that the retinal thinning we observed reflected cell loss in healthy aging. However, interpretation of retinal thinning is not straightforward: Retinal extent and surface area increase throughout adulthood (present data; Katz & Robison, 1986; Obin et al., 2000; Feng et al., 2007; Mansour et al., 2008; Bissig &

Berkowitz, 2011). Due to this 'stretching' of the retina, some thinning is expected even if neuron numbers are fully preserved. Though we are aware of two reports of age-related cell loss in the pigmented rat retina which attempt to adjust for this 'stretching' of the retina (Katz & Robison, 1986; Obin et al., 2000), the adjustment presumes stretching and proportional thinning is uniform throughout the retina. If that were true, longitudinal rates of change in central retinal thickness and surface area would be well-correlated. We find no such correlation (Table 3; r=-0.05; P>0.05).

Other attempts to quantify age-related cell loss have produced negative results: Recent stereological work by Feng et al. (2007) indicated no cell loss in any retinal layer from 6 to 24 mo, and Harman et al. (2003) found that ganglion cell numbers, sampled evenly from a retinal wholemount, are stable from 3 to 30 mo. Rhodopsin levels are stable or increase from 4 to 26 mo, suggesting preserved photoreceptor numbers (Katz & Robison, 1986). In the retinas of young versus old C57BL/6 mice — which, like Long-Evans rats, show age-related CS declines, retinal thinning, and increases in retinal surface area (van Alphen et al., 2009; Samuel et al., 2011) — neuron numbers are unaffected by age when counted by flow cytometry (Samuel et al., 2011).

Recent studies suggest that retinal volume is unaffected by age (Feng et al., 2007; Samuel et al., 2011), further arguing against cell loss. Presently, we find age-related *increases* in total retinal volume. Though this also argues against cell loss, it's not immediately obvious why volume would increase with age. Age-related increases in astrocyte size (Mansour et al., 2008) and cross-sectional area of the nuclei within each retinal layer (Case & Plumber, 1993; Harman et al., 2003; but see Katz & Robison, 1986) may contribute, but would presumably influence the histology-based estimates showing constant volume (Feng et al., 2007; Samuel et al., 2011). We

speculate that changes in total extracellular water contribute: As the retinal sheet expands, distances between adjacent photoreceptors increase. A corresponding increase in the cross-sectional area of the interphotoreceptor space — the water-filled space between neighboring rod outer segments (see cross-sections in Hagins et al., 1970; Katz et al., 1991) — is therefore expected. Since rod outer segment length is stable with age, at least in the first 12 mo of life, (Fox & Rubinstein, 1989), such an increase in cross-sectional area should translate into an increase in the volume of the outer retina. Though detectable *in vivo* with MRI, the dehydration steps common to histologic methods would make them insensitive to such a volume increase.

The above considerations would suggest that measurements of retinal morphology are not sufficient, on their own, to understand the basis of vision declines in healthy aging. Nevertheless, rates of change in retinal surface area were well-correlated with rates of CS decline (Table 3), and initial retinal surface area was a strong predictor of declines in CS from the start to the end of our studies (Table 4,pt.2). At first glance, age-related reductions in dendritic field size of retinal ganglion cells (Samuel et al., 2011), for example, could explain this structure/function link: Amplified by the expansion of the retinal sheet, the fraction of retina covered by each dendritic arbor is substantially reduced, potentially producing gaps in visual field coverage by some RGC subtypes. Our findings seem to argue against that hypothesis: Insofar as increased retinal surface area is itself deleterious, one would expect a negative correlation between surface area and visual function even at study start, but no such relationship was found (Table 1). Also, longitudinally, one would expect that relatively rapid increases of retinal surface area would be correlated with relatively rapid declines in visual function, but we found a significant correlation in the opposite direction (Table 3): Those rats experiencing the largest surface area increases show the smallest losses in CS.

Links between retinal surface area and CS decline are part of the broader set of relationships with general eye growth: Axial length, lens thickness, and most other measures of eye morphology related to optics increased with age in a similar (roughly logarithmic) way. The starting values (Table 1), rates of change (Table 3), and predictive relationship between starting values and later rates of change (Table 4,pt.2) for each of these 'eye growth' variables were well-correlated with other 'eye growth' variables including retinal surface area. The above-stated relationships between CS and retinal surface area are similarly strong for lens thickness, corneal radius of curvature, and other such measures: Rats whose eyes grow least from the start to the end of the study tend to show the greatest age-related declines in CS (Table 3), and rats which start the experiment with large eyes tend to show the greatest age-related declines in CS (Table 4).

We synthesize the link between CS and morphology, using surface area as a representative metric for all 'eye growth' variables, in the following way: Consider very young (e.g. 14 d postnatal) rats: Retinal surface areas are fairly similar from rat to rat, ranging from 30 to 32.5 mm^2 (see Supplemental Material in Appendix A). By age ~2.5 mo, mean surface area is ~48 mm^2 (Fig.5). Consistent with a logarithmic growth curve (see Supplemental Material in Appendix A), at least half the postnatal growth needed to reach the old adult surface area of ~65 mm^2 (Fig.5) took place before the start of our longitudinal studies. In that early juvenile period, some of the rats grew much faster than others, producing the wide variety in surface areas seen in Figure 5 (e.g., ranging from 40 to 55 mm^2 in young adults). At the start of our studies, there was little sign that this early growth conferred either cost or benefit to visual function, given the preponderance of non-significant correlations between CS (and SFT) and 'eye growth' variables in Table 1. However, beginning the study with a large eye predicted greater declines in visual

function (Table 4). There seems to be a delayed penalty to unusually rapid postnatal growth. The correlation between rates of change in CS with rate of change in 'eye growth' (Table 3) may be explained through that relationship: Those large-eyed rats experienced less growth (Table 4,pt.2) during our study — owing to unusually rapid postnatal growth, they entered the study nearer to their final (old age) eye size.

Why might rapid eye growth in the earliest stages of life predict eventual vision declines? As the retina stretches, the relatively constant population of retinal neurons is distributed over a progressively larger surface area, and the average distance between neighboring neurons increases. It's therefore plausible that some remodeling is necessary to maintain the interconnectivity of these retinal neurons between early postnatal life and adulthood. If early eye growth is rapid enough, it may surpass the rate of remodeling. If true, this alone is not enough to diminish visual function, since surface area and other measures of eye size were generally not correlated with visual function at the start of our studies (Table 1). However, well-matched eye growth and neuronal remodeling in early life might buffer the retina against the reductions in (for instance) dendritic field size of retinal ganglion cells (Samuel et al., 2011) in later in life. Extraocular factors may also contribute to the association between eye size/growth and CS declines: Body weight, being well-correlated with 'eye growth' variables, also tracked with and predicted CS declines. Since low body weight in young-adulthood (3 mo) predicts prolonged lifespan among rats fed *ad libitum* (Anisimov et al., 2004), low body weight during young-adulthood may also confer some modest neuroprotective effects in the retina.

Future studies may experimentally manipulate early eye growth to better-determine its relationship to later vision decline. Calorie restriction ('CR') is one possible approach: Compared to controls (fed *ad libitum*), rats maintained on a CR diet starting in young adulthood

have smaller retinal extents at mid-adulthood (age 12 mo). Later, their eye growth is more rapid than in rats fed *ad libitum*, since both groups eventually (age ≥24 mo) have the same retinal extents (Obin et al., 2000). However, CR could confound early eye growth with altered retina ion physiology: CR is reported to alter Ca^{2+} homeostasis in the hippocampus, preserving the low-influx phenotype of young adulthood, even through old age (Hemond & Jaffe, 2005). A similar pattern might be found for the retina.

6.2 Physiological Changes in the Aging Rat Retina

Retinal Mn^{2+} influx increased throughout adulthood in both the inner and outer retina. Longitudinally, there were no consistent relationships between increases in Mn^{2+} uptake and changes in eye morphology (Table 3), suggesting that they are relatively independent processes. Retinal Mn^{2+} uptake was the strongest predictor of CS decline in the ~4.5 mo following MRI scans (Figs.6,7). When Mn^{2+} uptake in the dark-adapted outer retina was considered along with initial CS, we could account for ~70% of the variance in rates of subsequent CS decline (Fig.7). It is unclear whether predictions of CS decline could be improved any further, since some variability is intrinsic to behavioral measures of visual function. For instance, although our test-retest measures of SFT were well-correlated, the first measurements ('test') never accounted for more than ~70% of the variance in the second ('retest'). The present findings argue that progressive and potentially-deleterious changes in retinal ion physiology occur in normal aging. Given the strong link between high retinal Mn^{2+} uptake and CS declines in the subsequent ~4.5 mo, we were interested in identifying the molecular basis of age-related increases in Mn^{2+} uptake. To this end, we compared Mn^{2+} uptake in dark- versus light-adapted retina during aging, and pharmacologically modified Mn^{2+} uptake in Arms 2 and 3.

In the inner retina, there is extensive spatial overlap and relatively equal representation of light-activated (ON pathway) and dark-activated (OFF pathway) neurons. Because the present image resolution is too low to distinguish between these pathways, no dark-light differences in inner retinal (16-28%thick) Mn^{2+} uptake were expected or found, consistent with previous work (e.g. Berkowitz et al., 2009; Berkowitz et al., 2006; Bissig & Berkowitz, 2011). This does not imply that the inner retina is quiescent. Rather, during the period of Mn^{2+} accumulation, one would expect roughly half of inner retinal neurons to be depolarized regularly in light-exposed (ON) eyes, while the other half would be depolarized regularly in patched (OFF) eyes. Some degree of activity-dependent Mn^{2+} influx is therefore expected in both conditions, entering depolarized neurons through L-VGCCs (Drapeau & Nachshen, 1984; Carlson et al., 1994; Cross et al., 2007; Berkowitz et al., 2011; Berkowitz et al., 2007b). Consistent with these considerations, we found that L-VGCC antagonists significantly inhibited inner retinal Mn^{2+} uptake in Arms 2 and 3.

The inner retina experienced an age-related increase in Mn^{2+} uptake (Fig.4), which significantly predicted CS declines (Table 4,pt.1). High doses of the L-VGCC blocker inhibited a similar proportion of Mn^{2+} uptake (i.e., '%inhibition') in both young- and mid-adult rats (Fig.10). Thus, age-related increases in both the L-VGCC-dependent and L-VGCC-independent portions of Mn^{2+} uptake seem to occur. Also note that, at both ages, substantial Mn^{2+} uptake was detected even with high doses of antagonist (Fig.10). For inner retina, it is unclear whether the L-VGCC-independent Mn^{2+} uptake is activity-dependent — for instance, involving other types of voltage-gated channels — or represents some basal level of Mn^{2+} uptake occurring even in quiescent (hyperpolarized) neurons and/or adjacent non-neuronal (e.g., Müller) cells.

The outer retina is almost exclusively populated by photoreceptors, which are depolarized in darkness and hyperpolarized in light (for review, see Yau, 1994). Consistent with previous reports (e.g., Berkowitz et al., 2009; Berkowitz et al., 2006; Bissig & Berkowitz, 2011) and the expectation of Mn^{2+} uptake through voltage-gated channels, we found significantly higher Mn^{2+} uptake in darkness than in light in the outer retinas of each age group (Fig.4). It is very likely that those dark-light differences in Mn^{2+} uptake are specific to photoreceptors: Although Müller cell processes interdigitate with photoreceptor somas in the outer retina, each Müller cell also extends through inner retina. Intracellular movement of Mn^{2+} is fairly rapid — generally > 2mm/hr (Watanabe et al., 2001; Olsen et al., 2010) — and any Mn^{2+} entering Müller cells in a light-dependent fashion therefore had hours to evenly distribute over the < 0.2mm separating inner from outer retina. Since dark-light differences were confined to the outer retina, we attribute them to the only non-negligible population of cells confined to the outer retina: photoreceptors.

Dark-light differences in outer retinal Mn^{2+} uptake progressively increased with age (Fig.4), and rats with high activity-dependent Mn^{2+} uptake compared to other cohort members experienced the greatest CS declines in the ~4.5 mo following MEMRI (Table 4,pt.1). The outer retina's activity-dependent Mn^{2+} uptake occurs predominantly through photoreceptor L-VGCCs. In Arm 2, dark-light differences were eliminated by systemic administration of a L-VGCC blocker: Nifedipine inhibited outer retinal Mn^{2+} uptake in darkness, but had no effect in light (Fig.8). In dark-adapted eyes, outer retinal Mn^{2+} uptake was similarly-inhibited by topical nifedipine administration (Fig.9). That finding may be important for some proposed uses of L-VGCC blockers wherein systemic drug delivery would be problematic (e.g. retinal ischemia or retinopathy of prematurity; Crosson et al., 1990; Berkowitz et al., 2011). For present purposes, the topical nifedipine data confirmed that L-VGCC blockade decreases neuronal Mn^{2+} uptake

independent of peripheral drug effects, as expected from previous *in vitro* studies (Drapeau & Nachshen, 1984; Carlson et al., 1994).

The present data argue that rat photoreceptors experience a progressive age-related increase in ion influx through L-VGCCs. Explanations for this phenomenon fall, broadly, into two categories: (1) Light-dependent changes in photoreceptor membrane voltage depend on dark-light differences in cyclic-GMP gated channels ('cGMPGCs'). In darkness, cGMPGCs are open, allowing constant influx of the major charge carrier, Na^+, into the photoreceptor and preventing membrane hyperpolarization. Light exposure ultimately closes cGMPGCs, stopping most Na^+ influx and permitting membrane hyperpolarization (for review, see Yau, 1994). Although Mn^{2+} does not appear to enter cGMPGCs (except in special, non-physiologic, preparations; Capovilla et al., 1983; Cervetto et al., 1988), light-dependent changes in Mn^{2+} uptake through L-VGCCs will depend on light-dependent changes in photoreceptor membrane voltage, which in turn is controlled by cGMPGCs. We first considered the possibility that this electrical response to light becomes more exaggerated with age, producing larger dark-light differences in L-VGCC opening and therefore Mn^{2+} uptake. (2) A change in expression or regulation of the L-VGCCs themselves could increase dark-light differences in Mn^{2+} uptake. In the conceptually simplest case — the number of L-VGCCs increases with age — Mn^{2+} has more opportunities to enter in darkness, when the membrane is depolarized and L-VGCCs are open, but a similar number in light, when L-VGCCs are closed, producing increased dark-light differences in Mn^{2+} uptake.

If the electrical activity of the photoreceptors increases with age, it will be difficult to distinguish between the first and second possibilities, since the effects could be additive. If the electrical activity of the photoreceptors is constant or decreases with age, then a change in L-

VGCCs themselves is more likely to account for the age-related increase in dark-light differences documented in Arm 1.

Previous studies strongly argue against the first possibility; that light-dependent changes in photoreceptor membrane voltage increase with age. The electrical response of photoreceptors to light, ultimately determined by cGMPGCs currents, is described *in vivo* by the amplitude of the electroretinogram a-wave (Breton et al., 1994). Through adulthood, progressive age-related *decreases* in a-wave amplitude are found in humans (Wright et al., 1985; Freund et al., 2011), albino rats (DiLoreto et al., 1995), pigmented rats (Parmer et al., 1982; Charng et al., 2011), and in pigmented mice (Kolesnikov et al., 2010). In mice, the age-related decrease in a-wave amplitude was further probed using *ex vivo* measurements of individual photoreceptors' rod outer segments, which confirmed diminished electrical (i.e., cGMPGC current) responses to light (Kolesnikov et al., 2010).

Since dark-light differences in total current across the photoreceptor membrane (predominantly through cGMPGCs) appear to decrease with age, but dark-light differences in outer retinal Mn^{2+} uptake (through L-VGCCs) increased with age in the present work, we next considered the second possibility — that the aging rat retina experiences an alteration in expression or regulation of L-VGCCs. Intriguely, in the rat hippocampus, age-related increases in neuronal Ca^{2+} influx, L-VGCC density, and L-VGCC protein expression have been documented, and are greatest in those rats with the poorest cognitive function (Thibault and Landfield, 1996; Veng & Browning, 2002; Veng et al., 2003). In the hippocampus, increased expression of the pore-forming α L-VGCC subunit is isoform specific, with the ~180 kDa isoform of α_{1D} increasing with age, while expression of α_{1C} and the larger (>200 kDa) α_{1D} isoform appears stable (Veng & Browning, 2002, Veng et al., 2003). By analogy to the

hippocampus, we expected age-related increases in retinal α_{1D} expression. The α_{1D} isoform is roughly an order of magnitude less-sensitive to pharmacological blockade than α_{1C} (Xu and Lipscombe, 2001; Koschak et al., 2001; Tarabova et al., 2007). Based on those isoform-specific drug sensitivities, we first tested for a change in retinal α_{1D} expression *in vivo* by measuring inhibition of Mn^{2+} uptake by different doses of the L-VGCC antagonist diltiazem. We found substantial inhibition with 10 mg/kg doses in young adult rats, consistent with previous work (Berkowitz et al., 2007b), but 100 mg/kg doses were needed to produce similar %inhibition in mid-adult rats (Fig.10). This result is of some interest in its own right, suggesting that neuronal L-VGCC-based therapies/interventions may become progressively less-effective with age. For present purposes, though, the diltiazem dose-response differences between young and mid-adult rats strongly suggest that retinal α_{1D} L-VGCC expression increases with age. Western blots (Fig.11) further support that *in vivo* finding: Expression of the ~180 kDa isoform of α_{1D} increased with age, while no change in expression of either α_{1C} or the larger (>200 kDa) α_{1D} isoform was found.

Our interpretation of age-related increases in outer retinal Mn^{2+} uptake focuses mainly on dark-light differences because they are relatively easy to interpret: They are activity-dependent, L-VGCC sensitive, and specific to photoreceptors (rather than e.g., Müller cells). However, even when statistically controlling for the strong correlation between dark-light uptake differences and later CS declines, we found that Mn^{2+} uptake in the light-adapted outer retina remained a unique and significant predictor of CS declines. Since photoreceptors are relatively hyperpolarized in light, and ion flux presumably low, it's possible that this represents Mn^{2+} entry into Müller cells. If so, the present results for the light-adapted outer retina might support Bringmann et al. (2000)'s finding of age-related increases in ion influx through Müller cell L-VGCCs. On the

other hand, we found that light-adapted outer retinal Mn^{2+} uptake appears insensitive to L-VGCC blockade (Fig.8). We therefore speculate that Mn^{2+} is entering light-adapted photoreceptors though some cGMP- and voltage-*in*dependent route. If so, this could offer a partial explanation for why L-VGCC expression increases with age: Since Ca^{2+} influx controls neurotransmitter release by photoreceptors (Schmitz & Witkovsky, 1997), normal function could be severely compromised unless the difference between (or ratio of) dark versus light influx is preserved. Increased L-VGCC expression may therefore compensate for increased Ca^{2+} permeability in the *hyper*polarized photoreceptor, so as to proportionally increase Ca^{2+} permeability in the *de*polarized receptor. Although we found that magnitude dark-light differences increased with age, no change was noted in the ratio of dark to light Mn^{2+} uptake (Fig.4).

Within each group of rats, those with relatively low Mn^{2+} uptake at the start of the study later showed the largest age-related increases in Mn^{2+} uptake for the inner retina and dark-adapted outer retina (Fig.6; negative correlations between ΔR_1s in Table 4,pt.2). Those that started the study with relatively high Mn^{2+} uptake tended to show the smallest subsequent increases in Mn^{2+} uptake. This tendency may explain why Mn^{2+} influx is a strong predictor of CS declines over the ~4.5 mo following MRI scans, but a poor predictor of average CS declines from the start to the end of the study — a yearlong period for Group MO: After ~4.5 mo passes, the mechanism relating high ion influx to CS decline has affected those rats which started with high Mn^{2+} uptake, and insofar as Mn^{2+} uptake goes no higher, no further declines would be expected. In contrast, those rats starting with low Mn^{2+} uptake convert to a high uptake phenotype after ~4.5 mo (as seen for Group YM; Fig.6). They are then primed to experience the largest CS declines from ~4.5 to ~12 mo post-MRI. This pattern is shown in Figure 6 and Table 4,pt.1: Beginning the study with high Mn^{2+} uptake predicted the largest CS declines in the ~4.5

mo post-MRI, but beginning with low Mn^{2+} uptake predicted the largest CS declines from 4.5 to ~12 mo post-MRI.

In interpreting the present physiological data, three potential confounds need to be considered. (1) Since very high doses of Mn^{2+} can be toxic (Silva et al., 2004), there must be some assurance that the modest doses used here are non-toxic. Otherwise, the ability of Mn^{2+} uptake to predict later CS declines could be interpreted as a toxic effect of the Mn^{2+} ions themselves. Several lines of evidence argue against Mn^{2+} toxicity in the present study: We have previously demonstrated that the present dose (222 μmol Mn^{2+} / kg) is non-toxic to the rat retina, based on measurements of intraocular pressure, blood-retinal barrier integrity, retinal histology (Berkowitz et al., 2006), electroretinography, and dose-redose reproducibility of retinal Mn^{2+} enhancement (Berkowitz et al., 2007a). If Mn^{2+} exposure affected long-term visual function, it would be evident in comparisons of ~7 mo data from Groups YM and MO: At the time of the ~7 mo vision tests, the former but not the latter had previously been injected with Mn^{2+}. *Post-hoc*, we find that Group YM and Group MO have similar visual function at ~7 mo (for SFT, P=0.277; for CS, P=0.0908; two-tailed t-tests), further arguing against toxicity. Thus, available data overwhelmingly demonstrate that 222 μmol Mn^{2+} / kg is non-toxic to the rat retina. This is consistent with previous work related to the rat hippocampus, which showed no histological signs of toxicity following a 500 μmol Mn^{2+} / kg injection (Eschenko et al., 2010b), and normal performance on a memory task after a 200 μmol Mn^{2+} / kg injection (Jackson et al., 2011). (2) Longitudinally, we found that Mn^{2+} uptake increased with age. If Mn^{2+} efflux rates were slow enough, then the second measurement might be higher than the first merely because residual Mn^{2+} remains from the first injection. This seems very unlikely, given that the half-life for retinal Mn^{2+} efflux is less than one day (Tofts et al., 2010). In the present study, three rats were selected

from Group MO to measure baseline (no Mn^{2+}) R_1s in the retina at age ~19 mo. Since those values were similar to the never-injected rats at ages ~2.5 mo and ~7 mo, it is unlikely that residual Mn^{2+} was present one year (>365 efflux half-lives) after that first injection. Finally, the longitudinal finding of higher Mn^{2+} uptake in mid- than young-adult rats (Group YM) can be re-checked by comparing the once-injected ~2.5 mo rats from Group YM to the once-injected ~ 7 mo rats from Group MO: Those *post-hoc* comparisons yield significant differences for both inner and outer retina in both dark and light (each $P<0.0015$), consistent with longitudinal findings (Fig.4). Data collected while testing the effects of diltiazem (Fig.10) similarly suggest greater uptake in mid- than young-adult retinas. (3) Finally, any declines in blood-retinal barrier (BRB) integrity might alter neuronal Mn^{2+} exposure, and therefore uptake. We tested for vitreous enhancement following injection of the intravascular contrast agent Gd-DTPA, and found no signs of BRB compromise during healthy aging (see Supplemental Material in Appendix A for additional detail), consistent with previous work (Vinores et al., 1990).

6.3 Conclusions

Longitudinally, we documented age-related vision declines along with progressive increases in eye size and retinal Mn^{2+} uptake in adult rats. Measuring from the start to the end of our studies, the rate of CS decline was predicted by several measures of initial eye size, such as retinal surface area. Since the rats beginning our study with the largest eyes experienced the greatest CS declines, our data suggest that relatively rapid early eye growth — from postnatal to young-adult life — is somehow deleterious. Age-related increases in Mn^{2+} uptake also seem deleterious, since high retinal Mn^{2+} uptake was a strong predictor of CS declines in the ~4.5 mo following MRI scans. In the outer retina, the age-related increase in activity-dependent Mn^{2+} uptake is likely due to an increase in photoreceptor α_{1D} L-VGCC expression.

Prior studies of the anatomy and physiology of the aging retina have had little success explaining age-related declines in visual function (see Spear, 1993 for review). Our *in vivo* measurements of retinal morphology detected no signs of volume loss with age, suggesting that cross-sectional measurements aimed at detecting cell loss — based, for example, on retinal thickness — would be uninformative. Although lifespan patterns of eye growth predict eventual vision declines, a longitudinal experimental design is needed to detect this effect, and would be difficult with non-MRI methods. To-date, most *in vivo* studies of retinal physiology have been performed with some variant of the electroretinogram (ERG). However, ERG appears insensitive to the large alterations in L-VGCC-related ion physiology that we detected with MEMRI. *Ex vivo* electrophysiologic studies (e.g. patch clamp) may be sensitive to age-related increases in ion influx through L-VGCCs, but would be incompatible with longitudinal studies. MEMRI is capable of measuring both eye morphology and retinal ion physiology non-invasively — an essential feature when using those measures to predict and explain subsequent vision declines. We have previously shown that a clinically-relevant dose of Teslascan, an FDA-approved Mn^{2+}-based contrast agent, provides enough neuronal Mn^{2+} influx to detect dark-light differences in the rat retina (Tofts et al., 2010). It may therefore be possible to non-invasively test the strongest findings of the present rat studies in humans: whether Mn^{2+} uptake is greater in the retinas of old than young adults, and whether higher neuronal Mn^{2+} uptake predicts greater vision declines in healthy aging.

APPENDIX A

SUPPLEMENTAL MATERIAL

In this Supplemental Material, we provide additional details on (1) our tests of blood-retinal barrier integrity, (2) our validation of SFT measurements through test-retest comparisons on the in-house system, and comparisons of SFT on the in-house to the commercial system, and (3) use data from the main text and previously-published juvenile rat data to show lifespan growth curves for MRI measurements.

Blood-Retinal Barrier (BRB) Integrity:

In the Main Text, we reported that blood retinal barrier permeability surface area product (BRB PS) was not effected by age, and was consistent with previous control data (Berkowitz et al., 2004). Here, we illustrate these negative findings by showing sample images from a young and an old adult, and provide time-courses for each of the five subjects.

Loss of BRB integrity would be demonstrated by gradual leakage of Gd-DTPA into the vitreous, causing enhancement on T_1-weighted images. As seen in Figure A1, vitreous signal intensities appeared stable over time. Areas without a blood-structure barrier offer a positive internal control: the aqueous humor and large blood vessels clearly enhanced (higher signal intensity) after Gd-DTPA injection.

At the bottom of Figure A1, time-courses of vitreous signal intensity (vSI) are shown for each subject, after normalizing to the mean and standard deviation of pre-Gd-DTPA signal: The difference between vSI at a given time (vSI_t) and $vSI_{mean(pre\text{-}Gd\text{-}DTPA)}$, divided by the standard deviation vSI ($vSI_{sd(pre\text{-}Gd\text{-}DTPA)}$) from the five pre-Gd-DTPA images (i.e. (vSI_t - $vSI_{mean(pre\text{-}Gd\text{-}DTPA)}$) / $vSI_{sd(pre\text{-}Gd\text{-}DTPA)}$) from a rat produces a standardized vitreous signal intensity. Analogous to a z-score, values between -1.96 and 1.96 are within the 95% prediction interval of pre-Gd-

DTPA data. Only post-Gd-DTPA standardized values rising *and consistently remaining* above ~2 suggest vitreous enhancement. None of the five subjects showed signs of vitreous enhancement post-Gd-DTPA injection, arguing for an intact BRB.

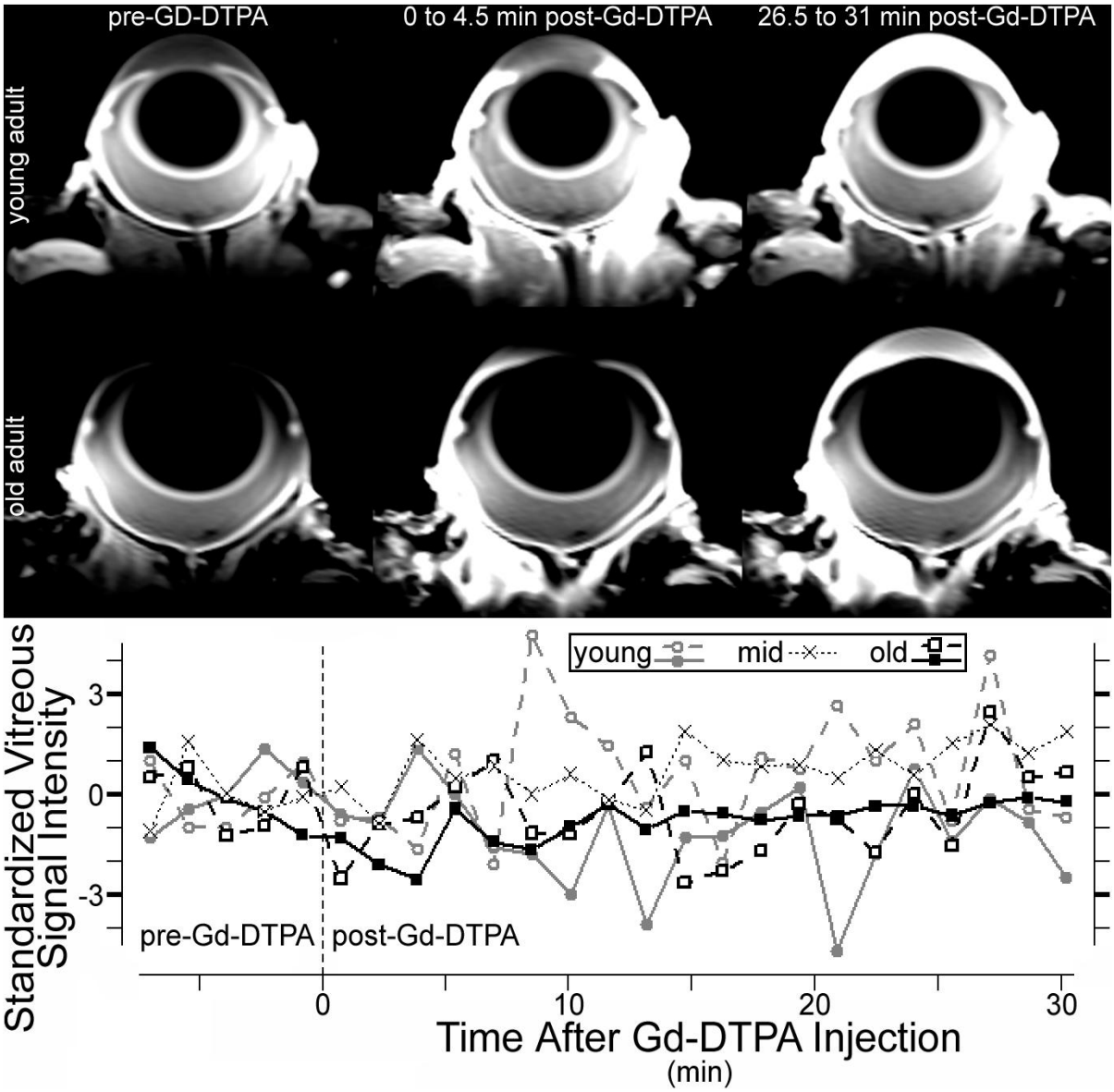

Figure A1: The blood-retinal barrier is intact throughout aging. *Top*: Representative time series of gadolinium enhancement in a young (aged 72 d) and an old (603 d) rat, showing averaged eye images before, just after, and a half hour after intravenous injection with Gd-DTPA. For each series of three, brightness and contrast are set identically to highlight any appearance of Gd-DTPA enhancement, which is demonstrated as an increase in signal intensity (black to grey to white) between pre- and post-Gd-DTPA images. Both series show rapid enhancement of vasculature and slower enhancement of the aqueous humor. However, neither shows enhancement of the vitreous, suggesting an intact blood-retinal barrier. *Bottom:* The time-course of standardized vitreous values is shown for all five subjects. Vitreous values regularly remained < 2 for the duration of the experiment, suggesting no enhancement at any age. In contrast, analogous measurements from the aqueous humor — which does not have a blood-structure barrier and visibly enhances (see *Top*) —produced standardized values >100 in all subjects (not shown). The absence of Gd-DTPA leakage into the vitreous strongly argues for an intact BRB throughout the present age range.

Validation of SFT Measurements:

We measured SFTs from young and old adult rats on our in-house system, and then measured SFTs from the same rats on a commercially-available system (OptoMotry; CerebralMechanics, Lethbride, Alberta, Canada; Douglas et al., 2005; Prusky et al., 2008). On both systems, the rat is surrounded by a virtual barrel displaying sine wave gratings with a set number of cycles per barrel degree (c/bd). For instance, a barrel showing 0.5 c/bd contains (360° * 0.5 cycles/° =) 180 cycles of the sine wave grating. On the commercial system, the display is dynamically altered based on eye position, such that the rat sees 0.5 cycles per degree visual angle when the machine is set to 0.5 c/bd. No such dynamic adjustments were possible on the in-house system, meaning that as rats moved closer to a screen, the number of cycles contained in each degree visual angle would decrease, becoming easier to see (e.g. a 0.5 c/bd may be seen as 0.45 cycles per degree visual angle). For this reason, the threshold c/bd values for the in-house system were expected to be higher than for the commercial system.

Consistent with expectations, young rats had SFTs of 0.564±0.005 c/bd on the commercial system and 0.676±0.010 c/bd on the in-house system. Old rats had SFTs of (mean±SEM) 0.524±0.004 c/bd on the commercial system and 0.627±0.010 c/bd on the in-house system. Importantly, as shown in Figure A2, measurements on our in-house system were well-correlated with those on the commercial system for young rats (r=0.70; P=0.0360), old rats (r=0.75; P=0.00301), and the combination of both age groups (r=0.82; P=3.56e-6). SFTs from the commercial system were in good agreement with the ~0.54 cycles per degree visual angle obtained from Long-Evans rats in previous studies (Douglas et al., 2005; Prusky et al., 2008).

A separate set of measurements used mid-adult rats to test the internal reliability of vision tests on the in-house system: SFT was measured twice in 13 rats, with measurements separated

by ~14 d. Good correlation between the first and second measurements would argue for the reliability of our SFT measurements. Consistent with expectations, we found that SFTs from the first to second measurement were well-correlated (Fig.A2; r=0.70; *P*=0.00748) and stable over time (respectively 0.640±0.016 and 0.626±0.017 c/bd; difference -0.014±0.013, *P*=0.296 on two-tailed paired t-test).

The data used to validate SFT measurements also show that age-related changes reported for Arm 1 are replicable: Although old adults tested here were part of Arm 1, the young and mid-adult rats were not. Using one-tailed t-tests, we again find that SFT was higher for young than mid-adulthood rats on the in-house system (*P*= 0.0492 or 0.0177, depending on whether the test or retest mid-adult data are used, respectively), but similar between mid- and old adults on the in-house system (*P*=0.250 or 0.479 depending on whether the test or retest data are used, respectively). As expected by the declines from young to mid-adulthood, we found significantly lower SFTs in old than young rats (*P*=0.00162). That pattern was also present in SFT data collected on the commercial OKT system (*P*=1.21e-6).

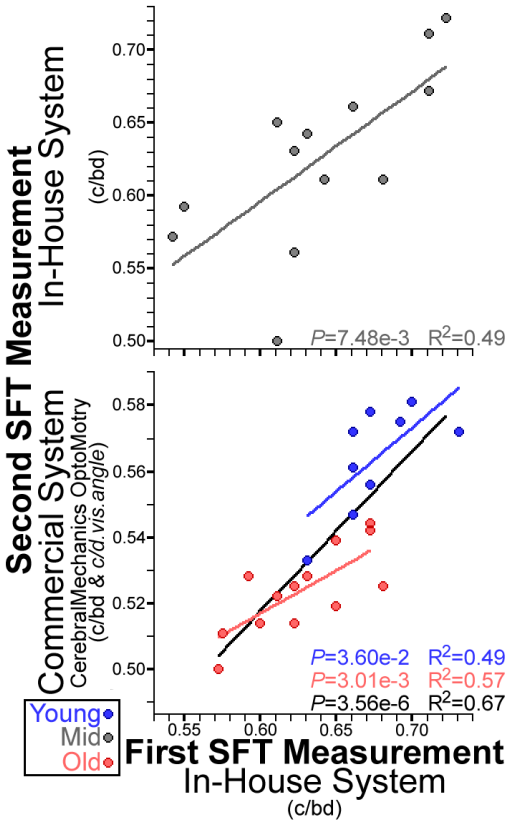

Figure A2: Validation of SFT measurements on the in-house system. *Top:* Measurements are internally validated by demonstrating reproducibility on the in-house system. We found a significant correlation between measurements taken ~14 d apart in mid-adult rats. *Bottom:* SFT measurements on the in-house system are externally validated against the commercial system (CerebralMechanics OptoMotry) in which the virtual barrel stimulus is dynamically adjusted based on the rat's position in the device arena. In that way, the number of cycles per barrel degree (c/bd) is made equivalent to the number of cycles per degree visual angle (c/deg.vis.angle) from the rat's perspective. The in-house system makes no adjustment for rat position, and thresholds therefore were expected to appear higher than in the commercial system: As a rat moves closer to a computer screen showing the stimulus, cycles appear larger from the subject's perspective. Portions of a 0.64 c/bd stimulus will appear 0.54 c/deg.vis.angle if the rat is sufficiently off-center. Despite the different approaches to stimulus presentation, values from the in-house and commercial systems are very-well correlated in young adults (blue), old adults (red), and the combination thereof (black): Between-device correlations are similar to the test-retest correlation. Importantly, regardless of the system, SFTs are noticeably higher in young than in old adults.

Based on the tight correlation between the two systems, the visual performance data from the in-house system (Main Text) are presented without correction to the commercial system.

Lifespan MRI Growth Curves

Growth curves are constructed using data from Arm 1 rats and from a small set of juvenile control rats. Most of the latter have contributed data to previous publications (Berkowitz et al., 2011; Chui et al., 2011): The left dark-adapted eye of postnatal/juvenile control rats was studied ~4 hr after Mn^{2+} injection under urethane anesthesia (4.1(1.5) ml/kg) at four different ages: 14 d (n = 6; weighing 23(1) g), 20-21 d (n = 6; 37(3) g), 32 d (n = 5; 95(3) g), and 53 d (n = 7; 207(36) g). Growth curves for Mn^{2+} uptake (ΔR_1) only used data from juveniles and the dark-adapted (patched) eyes in Arm 1 of the present work. (Although light ΔR_1s are available in Arm 1, we lack the juvenile ΔR_1 light data needed to produce a full growth curve.) Growth curves for morphological data (e.g., lens thickness, retinal volume) used data from juveniles and both the dark-adapted (patched) and light-exposed (unpatched) eyes of Arm 1 rats, for whom the left and right eye values were averaged to produce a single value (per rat per time point). When possible, Arm 1 rats were studied at two different ages. Those repeated measurements were several months apart, and considered independent of one another when fitting these growth curves.

For each dependent variable ("DV") — such as body weight, lens thickness, or outer retinal Mn^{2+} uptake — we began by fitting a logarithmic model (Eq.A1)

Eq.A1: $$DV = A * \ln(age) + B$$

wherein 'A' and 'B' are fitted parameters and age is given in days. 'B', the y intercept, is the extrapolated value for DV at birth. It is important to note that these intercept values are generally not useful since the earliest data in these model fits is from an age of 14 d: Due to the log

transform, extrapolation over the 2.64 natural log units between that age and the first day of life is at least as problematic as using only data from the beginning of adulthood (~50 d) to extrapolate values during senescence (~700 d; 2.64 natural log units after 50 d). The problem is exacerbated if the population growth curve is sigmoidal, with the possibility of extrapolating nonsensical values (e.g. negative body weight). 'A' is the slope relating the DV to log-transformed age such that a significant relationship between DV and age is demonstrated by when the 95% confidence interval ('95%CI') for 'A' does not include zero. We note that analyses in the Main Text also demonstrate age effects using a different approach (paired t-tests) which has fewer assumptions about the pattern of growth, and better-accommodates the repeated measures in our longitudinal data. Parameter estimates for logarithmic models are given with 95%CIs (calculated as estimate ± two standard errors) in Table A1.

Next, we fit a four-parameter Weibull model (Eq.A2) using the 'drc' package for R (http://www.r-project.org; e.g., 'model=drm(DV ~ age, fct= W2.4())').

Eq.A2: $$DV = a + (b - a) * (1 - \exp(-1 * \exp(c * (\ln(age) - \ln(d)))))$$

wherein 'a', 'b', 'c', and 'd' are fitted parameters and age is given in days. This function is asymmetrical about the inflection point, 'd' (when age = d, DV ≈ 0.37*a + 0.63*b). Parameter estimates for Weibull models are given with 95%CIs (calculated as estimate ± two standard errors) in Table A2.

In Figures A3 through A8, we show scatter plots of several measurements from control rats, as well as the best-fit lines (with 95%CI) for logarithmic and Weibull growth models, fit to those data as a function of age.

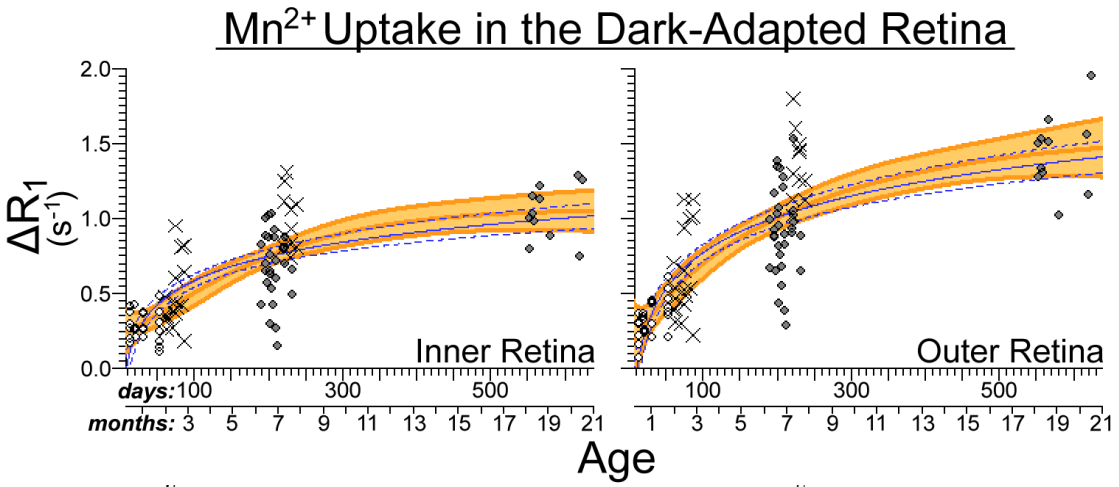

Figure A3: Mn^{2+} uptake increases with age in the dark-adapted retina. Mn^{2+} uptake is proportional to ΔR_1, which was measured in the inner retina (16-28%thick; left panel) and outer retina (48-68%thick; right panel) throughout the lifespan of the rat. Filled points represent data from Group MO of Arm 1. 'X's represent data from Group YM of Arm 1. Open points represent the data from juvenile rats described in this Appendix. The blue lines show the best-fit (solid line) and 95%CI (dashed lines) for the logarithmic model. The orange lines represent the best fit (middle dark orange line) and 95%CI (light orange fill, bordered by dark orange lines) for the Weibull model. This mapping of points and line colors is used in all of the remaining figures in this Appendix.

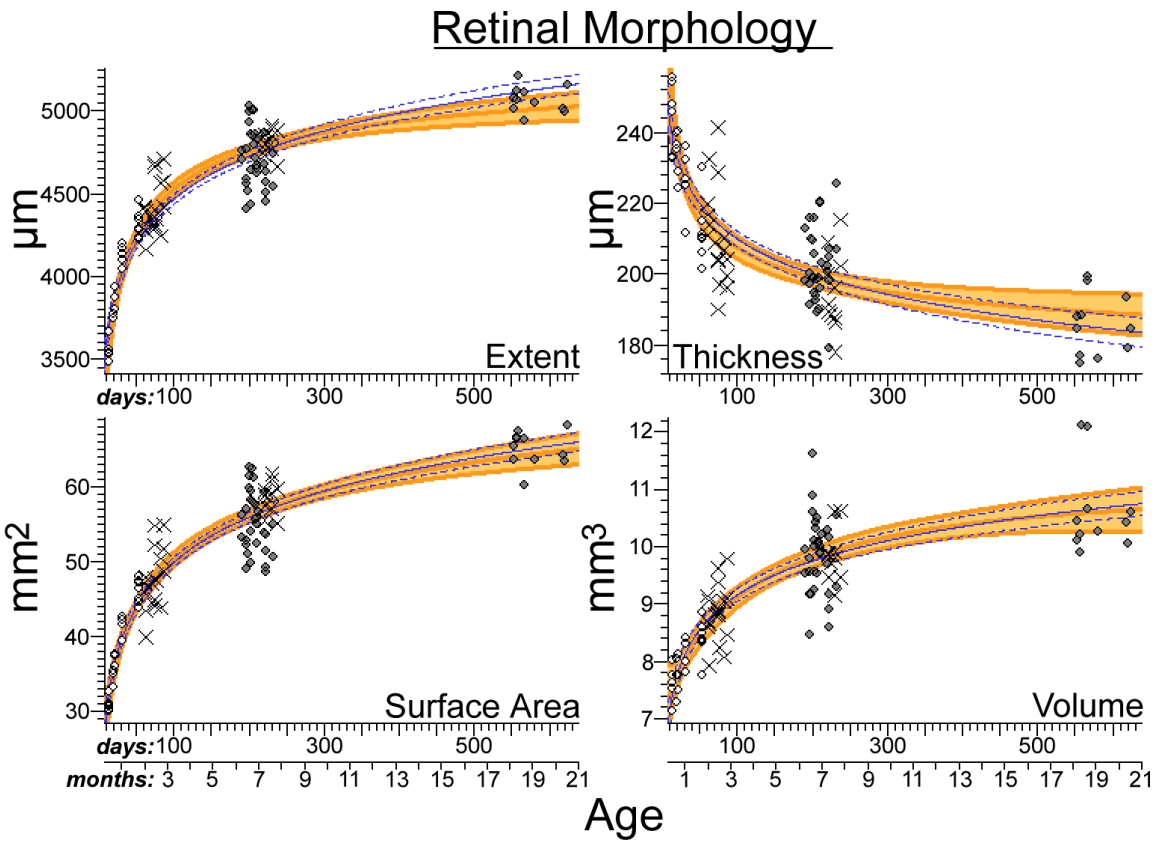

Figure A4: Retinal extent, surface area of the vitreoretinal border, and total retinal volume increase with age. Although the central retina thins with age, this may be partially explained by stretching of the retinal sheet during continued eye growth throughout adulthood. Despite retinal thinning, these data argue against age-related cell loss, since retinal volume increases with age. (See Fig.A3 Legend for explanation of lines and symbols.)

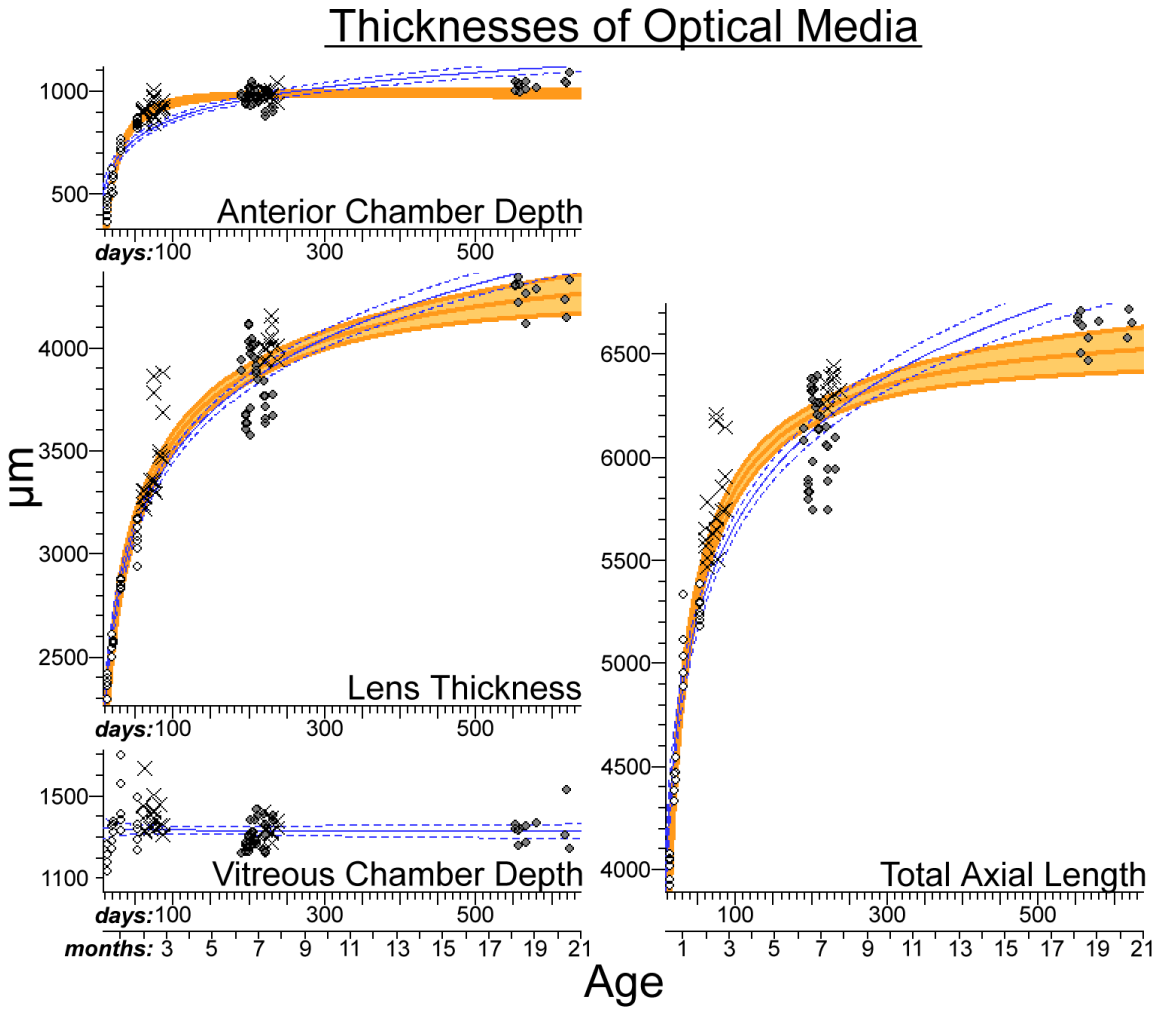

Figure A5: Anterior chamber depth and lens thickness increase with age. In contrast, vitreous chamber depth remains essentially constant (for this reason it was not possible to fit a Weibull model for that variable). Axial length — the sum of the chamber depths and lens thickness — increases with age. Note that the same y-axis distances are used on all four of these plots to facilitate visual structure-to-structure comparisons. (See Fig.A3 Legend for explanation of lines and symbols.)

Figure A6: Body weight increases with age. The pattern of growth closely follows a logarithmic curve throughout adulthood. (See Fig.A3 Legend for explanation of lines and symbols.)

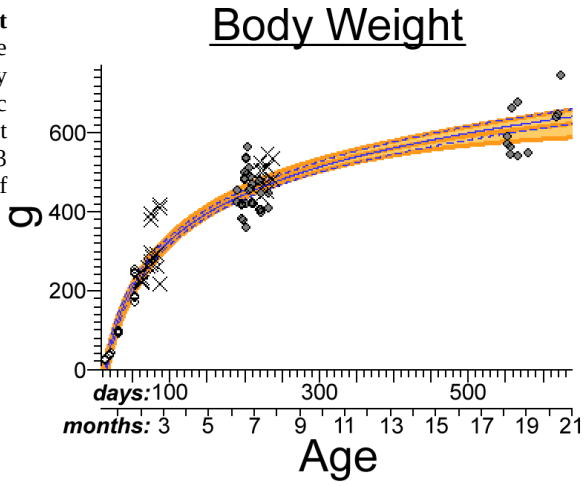

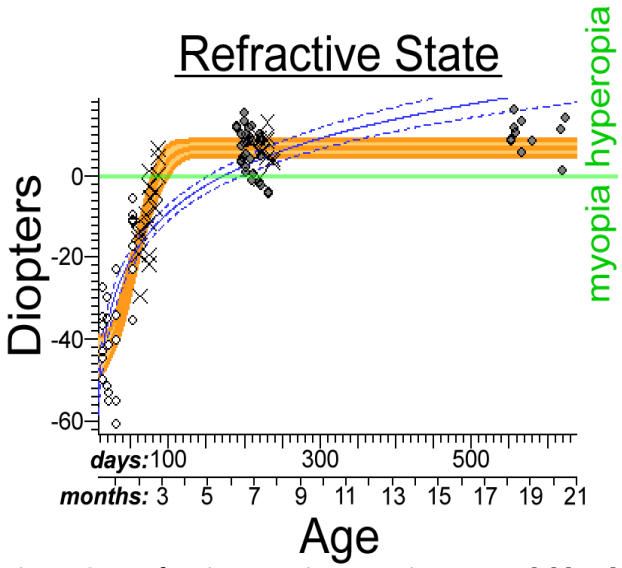

Figure A7: Refractive state increases in young adulthood, then plateaus. In early life, rats are myopic (nearsighted, refractive state < 0 D), but rapidly become mildly hyperopic (farsighted, > 0 D) in young adulthood. Refractive state is relatively stable from mid-adulthood onward. Note that even subtle differences in animal age may account for varying literature reports of myopia versus hyperopia in young adulthood: Behavioral testing by Wiesenfeld & Branchek (1976) implied myopia in young adulthood, and their reported body weights suggest that rats were between 70 and 95 d. The Weibull model produces mean estimates of -9.7 and +2.3 D at those ages. Hughes (1977), using both retinoscopy and single unit recordings from the optic nerve, found ~+9 D hyperopia in 115-130 d old rats. Our Weibull model gives hyperopic mean estimates of +5.8 D and +6.6 D at those ages. There is little literature information on changes beyond young adulthood: Meyer et al. (1997), using *v*isual *e*voked *p*otentials, found that both young and old rats are relatively emmetropic (refractive state near 0). However, this is based on peak responses after placement of an artificial lens, and it is unclear whether stimulus magnification by the lens was considered in the analysis. Also, refraction may differ from central versus peripheral field (Hughes 1977), a nuance not captured by VEP-based refraction. In a small sample, measured by ophthalmoscope and streak retinoscope, Massof & Chang (1972) found fairly consistent hyperopia , ~+15 D, between 90 to 200 d. (See Fig.A3 Legend for explanation of lines and symbols.)

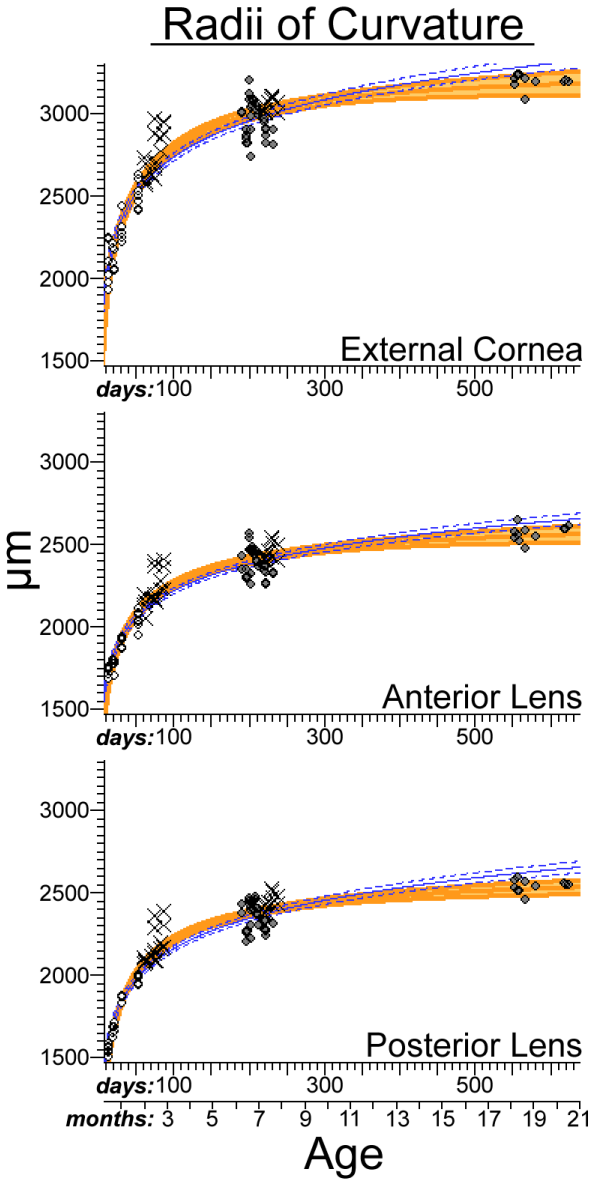

Figure A8: Age-related increases in radii of curvature. The radii of curvature for the external surface of the cornea, the anterior lens, and the posterior lens, all increase with age. (See Fig.A3 Legend for explanation of lines and symbols.)

Table A1: Parameter Estimates (with 95%CI) for logarithmic growth models. Estimates are bolded when significantly different from zero (based on 95%CI).

DV	units	logarithmic model *DV=A*ln(age)+B*			
		A		**B**	
		estimate	**95%CI**	**estimate**	**95%CI**
Body Weight	g	**169**	**(160 to 179)**	**-453**	**(-500 to -406)**
Using Patched (Dark-Adapted) Data					
Inner Retinal Mn^{2+} Uptake (ΔR_1)	s^{-1}	**0.233**	**(0.192 to 0.274)**	**-0.49**	**(-0.690 to -0.286)**
Outer Retinal Mn^{2+} Uptake (ΔR_1)	s^{-1}	**0.345**	**(0.292 to 0.398)**	**-0.82**	**(-1.078 to -0.558)**
Using Average of Patched and Unpatched Data					
Lens Thickness	*µm*	**517**	**(485 to 548)**	**1096**	**(944 to 1248)**
Anterior Chamber Depth	*µm*	**141**	**(125 to 146)**	**215**	**(129 to 290)**
Vitreous Chamber Depth	*µm*	-3.53	(-21.29 to 14.22)	**1349**	**(1262 to 1435)**
Axial Length	*µm*	**654**	**(606 to 702)**	**2659**	**(2426 to 2894)**
External Corneal Radius of Curvature	*µm*	**316**	**(294 to 339)**	**1282**	**(1171 to 1394)**
Anterior Lens Radius of Curvature	*µm*	**236**	**(220 to 253)**	**1133**	**(1052 to 1213)**
Posterior Lens Radius of Curvature	*µm*	**267**	**(249 to 284)**	**935**	**(850 to 1020)**
Refractive State	*Diopters*	**16.6**	**(14.7 to 18.4)**	**-85.3**	**(-94.4 to -76.3)**
Retinal Extent	*µm*	**377**	**(348 to 406)**	**2730**	**(2589 to 2871)**
Retinal Volume	mm^3	**0.862**	**(0.755 to 0.969)**	**5.19**	**(4.67 to 5.71)**
Retinal Surface Area	mm^2	**8.7**	**(8.06 to 9.33)**	**9.82**	**(6.73 to 12.91)**
Retinal Thickness	*µm*	**-14.3**	**(-16.3 to -12.2)**	**276**	**(266 to 286)**

Table A2: Parameter Estimates (with 95%CI) for Weibull growth models. Estimates are bolded when significantly different from zero (based on 95%CI). † Being relatively constant with age, a satisfactory Weibull model could not be fit for vitreous chamber depth. ‡ Since d is age of inflection point, the finding that d is significantly different from 0 argues that the population growth curve is at least somewhat sigmoidal over the age range analyzed. However, as exemplified by body weight (see Fig.A6), it may nevertheless be possible for a non-sigmoidal (e.g. logarithmic) curve to closely match a sigmoidal growth curve for most of postnatal life.

DV	four-parameter Weibull model $DV=a+(b-a)*(1-exp(-exp(c(ln(age)-ln(d)))))$							
	a		b		c		d‡	
	estimate	95%CI	estimate	95%CI	estimate	95%CI	estimate	95%CI
Body Weight	-428	(-1024 to 169)	**753**	**(483 to 1024)**	**0.417**	**(0.082 to 0.752)**	**95.2**	**(28.7 to 161.8)**
Using Patched (Dark-Adapted) Data								
Inner Retinal Mn^{2+} Uptake (ΔR_1)	**0.234**	**(0.058 to 0.411)**	**1.06**	**(0.88 to 1.24)**	**1.30**	**(0.34 to 2.25)**	**206**	**(135 to 276)**
Outer Retinal Mn^{2+} Uptake (ΔR_1)	0.104	(-0.373 to 0.580)	**1.58**	**(0.97 to 2.20)**	**0.871**	**(0.027 to 1.714)**	**216**	**(61 to 372)**
Using Average of Patched and Unpatched Data								
Lens Thickness	-1169	(-6709 to 4371)	**4507**	**(4041 to 4972)**	**0.309**	**(0.046 to 0.573)**	15.7	(-27.5 to 59.0)
Anterior Chamber Depth	-1901	(-5310 to 1509)	**991**	**(973 to 1009)**	**0.468**	**(0.198 to 0.738)**	4.98	(-5.51 to 15.47)
Vitreous Chamber Depth†	-	-	-	-	-	-	-	-
Axial Length	-5900	(-11880 to 80)	**6645**	**(6435 to 6856)**	**0.282**	**(0.204 to 0.360)**	2.78	(-1.11 to 6.66)
External Corneal Radius of Curvature	663	(-1333 to 2658)	**3243**	**(3059 to 3427)**	**0.424**	**(0.112 to 0.737)**	26.9	(-17.6 to 71.5)
Anterior Lens Radius of Curvature	183	(-2443 to 2809)	**2640**	**(2452 to 2828)**	**0.341**	**(0.032 to 0.650)**	16.2	(-28.9 to 61.2)
Posterior Lens Radius of Curvature	-1309	(-4019 to 1401)	**2614**	**(2497 to 2732)**	**0.291**	**(0.155 to 0.426)**	5.78	(-6.25 to 17.81)
Refractive State	**-44.6**	**(-50.1 to -39.1)**	**6.86**	**(4.83 to 8.90)**	**2.49**	**(1.57 to 3.41)**	**66.6**	**(60.5 to 72.6)**
Retinal Extent	-1234	(-4105 to 1636)	**5242**	**(4939 to 5545)**	**0.237**	**(0.152 to 0.322)**	3.59	(-2.16 to 9.33)
Retinal Volume	**6.71**	**(4.71 to 8.71)**	**10.89**	**(9.79 to 11.98)**	**0.653**	**(0.060 to 1.245)**	**127**	**(42 to 212)**
Retinal Surface Area	-76.9	(-194.1 to 40.2)	**88.0**	**(45.6 to 130.5)**	**0.157**	**(0.009 to 0.305)**	8.48	(-18.9 to 35.9)
Retinal Thickness	**168**	**(130 to 205)**	**393**	**(91 to 695)**	**-0.374**	**(-0.675 to -0.072)**	1.28	(-4.98 to 7.53)

APPENDIX B

LIST OF AUTHOR'S PUBLICATIONS DURING Ph.D TRAINING

Chui,T.Y.P., **Bissig,D.**, Berkowitz,B.A., Akula,J.D., 2012. Refractive development in the "ROP Rat". Journal of Ophthalmology. doi:10.1155/2012/956705

Li,X., McClellan,M.E., Tanito,M., Garteiser,P., Towner,R., **Bissig,D.**, Berkowitz,B.A., Fliesler,S.J., Woodruff,M.L., Fain,G.L., Birch,D.G., Khan,M.S., Ash,J.D., Elliott,M.H., 2012. Loss of caveolin-1 impairs retinal function due to disturbance of subretinal microenvironment. The Journal of Biological Chemistry, 287(20), 16424-16434.

Braun,R.D., **Bissig,D.**, North,R., Vistisen,K.S., Berkowitz,B.A., 2012. Human tumor cell proliferation evaluated using manganese-enhanced MRI. PLoS One, 7(2), e30572.

Berkowitz,B.A., **Bissig,D.**, Patel,P., Bhatia,A., Roberts,R., 2012. Acute systemic 11-cis-retinal intervention improves abnormal outer retinal ion channel closure in diabetic mice. Molecular Vision, 18, 372-376.

Berkowitz,B.A., **Bissig,D.**, Ye,Y., Valsadia,P., Kern,T.S., Roberts,R., 2012. Evidence for diffuse central retinal edema in vivo in diabetic male Sprague Dawley rats. PLoS One, 7(1), e29619.

Berkowitz,B.A., **Bissig,D.**, Bergman,D., Bercea,E., Kasturi,V.K., Roberts,R., 2011. Intraretinal calcium channels and retinal morbidity in experimental retinopathy of prematurity. Molecular Vision, 17, 2516-2526.

Bissig,D., Berkowitz,B.A., 2011. Same-session functional assessment of rat retina and brain with manganese-enhanced MRI, NeuroImage, 58(3), 749-760.

Holt,A.G., **Bissig,D.**, Mirza,N., Rajah,G., Berkowitz,B.A., 2010. Evidence of key tinnitus-related brain regions documented by a unique combination of manganese-enhanced MRI and acoustic startle reflex testing. PLoS One, 5(12), e14260.

Berkowitz,B.A., Roberts,R., **Bissig,D.**, 2010. Light-dependant intraretinal ion regulation by melanopsin in young awake and free moving mice evaluated with manganese-enhanced MRI. Molecular Vision, 16, 1776-1780.

Ivanova,E., Roberts,R., **Bissig,D.**, Pan,Z.H., Berkowitz,B.A., 2010. Retinal channelrhodopsin-2-mediated activity in vivo evaluated with manganese-enhanced magnetic resonance imaging. Molecular Vision, 16, 1059-1067.

Berkowitz, B.A., Gradianu, M., **Bissig,D.**, Kern, T.S., Roberts, R., 2009. Retinal ion regulation in a mouse model of diabetic retinopathy: Natural history and the effect of Cu/Zn superoxide dismutase overexpression. Investigative Ophthalmology & Visual Science, 50(5), 2351-2358.

Berkowitz, B.A., Roberts, R., Oleske, D.A., Chang, M., Schafer, S., **Bissig, D.**, Gradianu, M., 2009. Quantitative mapping of ion channel regulation by visual cycle activity in rodent photoreceptors in vivo, Investigative Ophthalmology & Visual Science, 50(4), 1880-1885.

Bissig, D., Berkowitz, B.A., 2009. Manganese-enhanced MRI of layer-specific activity in the visual cortex from awake and free-moving rats. NeuroImage, 44(3), 627-637.

Berkowitz,B.A., Roberts,R., Luan,H., **Bissig,D.**, Bui,B.V., Gradianu,M., Vingrys,A.J., 2007. Manganese-enhanced MRI studies of alterations of intraretinal ion demand in models of ocular injury, Investigative Ophthalmology & Visual Science 48(8): 3796-3804.

REFERENCES

Adriaens,E., Dhondt,M.M.M., Remon,J.P., 2005. Refinement of the Slug Mucosal Irritation test as an alternative screening test for eye irritation. Toxicology in Vitro, 19(1), 79-89.

Ahlijanian,M.K., Westenbroek,R.E., Catterall,W.A., 1990. Subunit structure and localization of dihydropyridine-sensitive calcium channels in mammalian brain, spinal cord, and retina. Neuron, 4(6), 819-832.

Alamouti,B., Funk,J., 2003. Retinal thickness decreases with age: an OCT study. The British Journal of Ophthalmology, 87(7), 899-901.

Anisimov,V.N., Arbeev,K.G., Popovich,I.G., Zabezhinksi,M.A., Arbeeva,L.S., Yashin,A.I., 2004. Is early life body weight a predictor of longevity and tumor risk in rats? Experimental Gerontology, 39(5), 807-816.

Anstey,K.J., Luszcz,M.A., Sanchez,L., 2001. Two-year decline in vision but not hearing is associated with memory decline in very old adults in a population-based sample. Gerontology, 47(5), 289-293.

Atchison,D.A., Markwell,E.L., Kasthurirangan,S., Pope,J.M., Smith,G., Swann,P.G., 2008. Age-related changes in optical and biometric characteristics of emmetropic eyes. Journal of Vision, 8(4):29, 1-20. doi: 10.1167/8.4.29

Bankson,D.D., Ellis,J.K., Russell,R.M., 1989. Effects of a vitamin-A-free diet on tissue vitamin A concentration and dark adaptation of aging rats. Experimental Gerontology, 24(2), 127-136.

Berkowitz,B.A., Bissig,D., Bergman,D., Bercea,E., Kasturi,V.K., Roberts,R., 2011. Intraretinal calcium channels and retinal morbidity in experimental retinopathy of prematurity. Molecular Vision, 17, 2516-2526.

Berkowitz,B.A., Bissig,D., Ye,Y., Valsadia,P., Kern,T.S., Roberts,R., 2012. Evidence for diffuse central retinal edema in vivo in diabetic male Sprague Dawley rats. PLoS One, 7(1):e29619.

Berkowitz,B.A., Roberts,R., Goebel,D.J., Luan,H., 2006. Noninvasive and simultaneous imaging of layer-specific retinal functional adaptation by manganese-enhanced MRI. Investigative Ophthalmology & Visual Science, 47(6), 2668-2674.

Berkowitz,B.A., Roberts,R., Luan,H., Bissig,D., Bui,B.V., Gradianu,M., Calkins,D.J., Vingrys,A.J., 2007a. Manganese-enhanced MRI studies of alterations of intraretinal ion demand in models of ocular injury. Investigative Ophthalmology & Visual Science, 48(8), 3796-3804.

Berkowitz,B.A., Roberts,R., Luan,H., Peysakhov,J., Mao,X., Thomas,K.A., 2004. Dynamic contrast-enhanced MRI measurements of passive permeability through blood retinal barrier in diabetic rats. Investigative Ophthalmology & Visual Science, 45(7), 2391-2398.

Berkowitz,B.A., Roberts,R., Oleske,D.A., Chang,M., Schafer,S., Bissig,D., Gradianu,M., 2009. Quantitative mapping of ion channel regulation by visual cycle activity in rodent photoreceptors in vivo. Investigative Ophthalmology and Visual Science, 50(4), 1880-1885.

Berkowitz,B.A., Roberts,R., Penn,J.S., Gradianu,M., 2007b. High-resolution manganese-enhanced MRI of experimental retinopathy of prematurity. Investigative Ophthalmology & Visual Science, 48(10), 4733-4740.

Bissig,D., Berkowitz,B.A., 2009. Manganese-enhanced MRI of layer-specific activity in the visual cortex from awake and free-moving rats. NeuroImage, 44(3), 627-635.

Bissig,D., Berkowitz,B.A., 2011. Same-session functional assessment of rat retina and brain with manganese-enhanced MRI. NeuroImage, 58(3), 749-760.

Boehm,A.G., Breidenbach,K.A., Pillunat,L.E., Bernd,A.S., Mueller,M.F., Koeller,A.U., 2003. Visual function and perfusion of the optic nerve head after application of centrally acting calcium-channel blockers. Graefe's Archive for Clinical and Experimental Ophthalmology, 241(1), 34-38.

Bose,S., Piltz,J.R., Breton,M.E., 1995. Nimodipine, a centrally active calcium antagonist, exerts a beneficial effect on contrast sensitivity in patients with normal-tension glaucoma and in control subjects. Ophthalmology, 102(8), 1236-1241.

Braekevelt,C.R., Hollenberg,M.J., 1970. The development of the retina of the albino rat. The American Journal of Anatomy, 127(3), 281-301.

Breton,M.E., Schueller,A.W., Lamb,T.D., Pugh,E.N.Jr., 1994. Analysis of ERG a-wave amplification and kinetics in terms of the G-protein cascade of phototransduction. Investigative Ophthalmolology & Visual Science, 35(1), 295-309.

Bringmann,A., Biedermann,B., Schnurbusch,U., Enzmann,V., Faude,F., Reichenbach,A., 2000. Age- and disease-related changes of calcium channel-mediated currents in human Müller glial cells. Investigative Ophthalmolology & Visual Science, 41(9), 2791-2796.

Calkins,D., Horner,P.J., Roberts,R., Gradianu,M., Berkowitz,B.A., 2008. Manganese-enhanced MRI of the DBA/2J Mouse Model of Hereditary Glaucoma. Investigative Ophthalmolology and Visual Science, 49(11), 5083-5088.

Callinan,L., McCarthy,T.V., Maulet,Y., Mackrill,J.J., 2005. Atypical L-type channels are down-regulated in hypoxia. Biochemical Society Transactions, 33(Pt 5), 1137-1139.

Campbell,L.W., Hao,S., Thibault,O., Blalock,E.M., Landfield,P.W., 1996. Aging changes in voltage-gated calcium currents in hippocampal CA1 neurons. The Journal of Neuroscience, 16(19), 6286-6295.

Capovilla,M., Caretta,A., Cervetto,L., Torre,V., 1983. Ionic movements through light-sensitive channels of toad rods. The Journal of Physiology, 343, 295-310.

Carabellese,C., Appollonio,I., Rozzini,R., Bianchetti,A., Frisoni,G.B., Frattola,L., Trabucchi,M., 1993. Sensory impairment and quality of life in a community elderly population. Journal of the American Geriatrics Society, 41(4):401-407.

Carlson,R.O., Masco,D., Brooker,G., Spiegel,S., 1994. Endogenous ganglioside GM1 modulates L-type calcium channel activity in N18 neuroblastoma cells. The Journal of Neuroscience, 14(4), 2272-2281.

Case,C.P., Plummer,C.J., 1993. Changing the light intensity of the visual environment results in large differences in numbers of synapses and in photoreceptor size in the retina of the young adult rat. Neuroscience, 55(3), 653-666.

Cervetto,L., Menini,A., Rispoli,G., Torre,V., 1988. The modulation of the ionic selectivity of the light-sensitive current in isolated rods of the tiger salamander. The Journal of Physiology, 406, 181-198.

Chang,B., Heckenlively,J.R., Bayley,P.R., Brecha,N.C., Davisson,M.T., Hawes,N.L., Hirano,A.A., Hurd,R.E., Ikeda,A., Johnson,B.A., McCall,M.A., Morgans,C.W., Nusinowitz,S., Peachey,N.S., Rice,D.S., Vessey,K.A., Gregg,R.G., 2006. The nob2 mouse, a null mutation in Cacna1f: anatomical and functional abnormalities in the outer retina and their consequences on ganglion cell visual responses. Visual Neuroscience, 23(1), 11-24.

Charng,J., Nguyen,C.T., Bui,B.V., Vingrys,A.J., 2011. Age-related retinal function changes in albino and pigmented rats. Investigative Ophthalmology & Visual Science, 52(12), 8891-8899.

Cheng,H., Nair,G., Walker,T.A., Kim,M.K., Pardue,M.T., Thule,P.M., Olson,D.E., Duong,T.Q., 2006. Structural and functional MRI reveals multiple retinal layers. Proceedings of the National Academy of Sciences of the United States of America, 103(46), 17525-17530.

Chuang,K., Koretsky,A.P., Sotak,C.H., 2009. Temporal changes in the T_1 and T_2 relaxation rates (ΔR_1 and ΔR_2) in the rat brain are consistent with the tissue-clearance rates of elemental manganese. Magn Reson Med, 61(6), 1528-1532.

Chui,T.Y.P., Bissig,D., Berkowitz,B.A., Akula,J.D., 2012. Refractive development in the "ROP Rat". Journal of Ophthalmology. doi:10.1155/2012/956705

Cohen,A.I., 1971. Electron microscope observations on form changes in photoreceptor outer segments and their saccules in response to osmotic stress. Journal of Cell Biology, 48(3), 547-565.

Cone,R.A., 1963. Quantum relations of the rat electroretinogram. The Journal of General Physiology, 46, 1267-1286.

Cross,D.J., Flexman,J.A., Anzai,Y., Sasaki,T., Treuting,P.M., Maravilla,K.R., Minoshima,S., 2007. In vivo manganese MR imaging of calcium influx in spontaneous rat pituitary adenoma. American Journal of Neuroradiology, 28(10), 1865-1871.

Crosson,C.E., Willis,J.A., Potter,D.E., 1990. Effect of the calcium antagonist, nifedipine, on ischemic retinal dysfunction. Journal of Ocular Pharmacology, 6(4), 293-299.

Cunea,A., Jeffery,G., 2007. The ageing photoreceptor. Visual Neuroscience, 24(2), 151-155.

Curcio,C.A., Millican,C.L., Allen,K.A., Kalina,R.E., 1993. Aging of the human photoreceptor mosaic: evidence for selective vulnerability of rods in central retina. Investigative Ophthalmology & Visual Science, 34(12), 3278-3296.

DiLoreto,D.,Jr., Ison,J.R., Bowen,G.P., Cox,C., del Cerro,M., 1995. A functional analysis of the age-related degeneration in the Fischer 344 rat. Current Eye Research, 14(4), 303-310.

Dittmer,A., Dittmer,J., (2006). β-actin is not a reliable loading control in Western blot analysis. Electrophoresis, 27(14), 2844-2845.

Douglas,R.M., Alam,N.M., Silver,B.D., McGill,T.J., Tschetter,W.W., Prusky,G.T., 2005. Independent visual threshold measurements in the two eyes of freely moving rats and mice using a virtual-reality optokinetic system. Visual Neuroscience, 22(5), 677-684.

Drapeau,P., Nachshen,D.A., 1984. Manganese fluxes and manganese-dependent neurotransmitter release in presynaptic nerve endings isolated from rat brain. The Journal of Physiology, 348, 493-510.

Duong,T.Q., Silva,A.C., Lee,S.P., Kim,S.G., 2000. Functional MRI of calcium-dependent synaptic activity: cross correlation with CBF and BOLD measurements. Magnetic Resonance in Medicine, 43(3), 383-392.

ECETOC (European Centre for Ecotoxicology and Toxicology of Chemicals), 1998. TR 048 : Eye Irritation: Reference Chemicals Data Bank (2nd Ed.). http://www.ecetoc.org

Elliott,D.B., Yang,K.C., Whitaker,D., 1995. Visual acuity changes throughout adulthood in normal, healthy eyes: seeing beyond 6/6. Optometry and Vision Science, 72(3), 186-191.

Eschenko,O., Canals,S., Simanova,I., Beyerlein,M., Murayama,Y., Logothetis,N.K., 2010a. Mapping of functional brain activity in freely behaving rats during voluntary running

using manganese-enhanced MRI: implication for longitudinal studies. NeuroImage, 49(3), 2544-2555.

Eschenko,O., Canals,S., Simanova,I., Logothetis,N.K., 2010b. Behavioral, electrophysiological and histopathological consequences of systemic manganese administration in MEMRI. Magnetic Resonance Imaging, 28, 1165-1174.

Feng,L., Sun,Z., Han,H., Zhou,Y., Zhang,M., 2007. No age-related cell loss in three retinal nuclear layers of the Long-Evans rat. Visual Neuroscience, 24, 799-803.

Freeman,E.E., Muñoz,B., Turano,K.A., West,S.K., 2005. Measures of visual function and time to driving cessation in older adults. Optometry and Vision Science, 82(8), 765-773.

Freund,P.R., Watson,J., Gilmour,G.S., Gaillard,F., Sauvé,Y., 2011. Differential changes in retina function with normal aging in humans. Documenta Ophthalmologica, 122(3), 177-190.

Foster,T.C., 2007. Calcium homeostasis and modulation of synaptic plasticity in the aged brain. Aging Cell, 6, 319-325.

Fox,D.A., Rubinstein,S.D., 1989. Age-related changes in retinal sensitivity, rhodopsin content and rod outer segment length in hooded rats following low-level lead exposure during development. Experimental Eye Research, 48(2), 237-249.

Genovese, C.R., Lazar, N.A., Nichols, T., 2002. Thresholding of statistical maps in functional neuroimaging using the false discovery rate. NeuroImage 15, 870-878.

Gonzalez,G.G., Garcia de la Rubia,P., Gallar,J., Belmonte,C., 1993. Reduction of capsaicin-induced ocular pain and neurogenic inflammation by calcium antagonists. Investigative Ophthalmology and Visual Science, 34(12), 3329-3335.

Guggenheim,J.A., Creer,R.C., Qin,X.J., 2004. Postnatal refractive development in the Brown Norway rat: limitations of standard refractive and ocular component dimension measurement techniques. Current Eye Research, 29(4-5):369-376.

Hagins,W.A., Penn,R.D., Yoshikami,S., 1970. Dark current and photocurrent in retinal rods. Biophysical Journal, 10(5), 380-412.

Hariri,S., Moayed,A.A., Dracopoulos,A., Hyun,C., Boyd,S., Bizheva,K., 2009. Limiting factors to the OCT axial resolution for *in-vivo* imaging of human and rodent retina in the 1060 nm wavelength range. Optics Express, 17(26), 24304-24316.

Harman,A.M., Abrahams,B., Moore,S., Hoskins,R., 2000. Neuronal density in the human retinal ganglion cell layer from 16-77 years. The Anatomical Record, 260, 124-131.

Harman,A.M., MacDonald,A., Meyer,P., Ahmat,A., 2003. Numbers of neurons in the retinal ganglion cell layer of the rat do not change throughout life. Gerontology, 49(6), 350-355.

Hell,J.W., Westenbroek,R.E., Warner,C., Ahlijanian,M.K., Prystay,W., Gilbert,M.M., Snutch,T.P., Catterall,W.A., 1993. Identification and differential subcellular localization of the neuronal class C and class D L-type calcium channel α1 subunits. The Journal of Cell Biology, 123(4), 949-962.

Hemond,P., Jaffe,D.B., 2005. Caloric restriction prevents aging-associated changes in spike-mediated Ca2+ accumulation and the slow afterhyperpolarization in hippocampal CA1 pyramidal neurons. Neuroscience, 135(2), 413-420.

Henkel,A.W., Bieger,S.C., 1994. Quantification of proteins dissolved in an electrophoresis sample buffer. Analytical Biochemistry, 223(2), 329-331.

Herman,J.P., Chen,K., Booze,R., Landfield,P.W., 1999. Up-regulation of α_{1D} Ca^{2+} channel subunit mRNA expression in the hippocampus of aged F344 rats. Neurobiology of Aging, 19(6), 581-587.

Hughes,A., 1972. A schematic eye for the rabbit. Vision Research, 12(1), 123-138.

Hughes,A., 1977. The refractive state of the rat eye. Vision Research, 17(8), 927-939.

Hughes,A., 1979. A schematic eye for the rat. Vision Research, 19(5), 569-588.

Inouye,S.K., 2000. Prevention of delirium in hospitalized older patients: risk factors and targeted intervention strategies. Annals of Medicine, 32(4), 257-263.

Iwamoto,M., Hagishita,T., Shoji-Kasai,Y., Ando,S., Tanaka,Y., 2004. Age-related changes in the levels of voltage-dependent calcium channels and other synaptic proteins in rat brain cortices. Neuroscience Letters, 366(3), 277-281.

Jackson,G.R., Owsley,C., McGwin,G.Jr., 1999. Aging and dark adaptation. Vision Research, 39(23), 3975-3982.

Jackson,S.J., Hussey,R., Jansen,M.A., Merrifield,G.D., Marshall,I., MacLullich,A., Yau,J.L., Bast,T., 2011. Manganese-enhanced magnetic resonance imaging (MEMRI) of rat brain after systemic administration of $MnCl_2$: hippocampal signal enhancement without disruption of hippocampus-dependent behavior. Behavioural Brain Research, 216(1), 293-300.

Kamphuis,W., Hendriksen,H., 1998. Expression patterns of voltage-dependent calcium channel α_1 subunits (α_{1A}- α_{1E}) mRNA in rat retina. Molecular Brain Research, 55(2), 209–220.

Kasthurirangan,S., Markwell,E.L., Atchison,D.A., Pope,J.M., 2008. In vivo study of changes in refractive index distribution in the human crystalline lens with age and accommodation. Invest Ophthalmol Vis Sci., 49(6), 2531-2540.

Karst, H., Werkman, T.R., Struik,M., Bosma,A., Joëls,M., 1997. Effects of adrenalectomy on Ca^{2+} currents and Ca^{2+} channel subunit mRNA expression in hippocampal CA1 neurons of young rats. Synapse, 26, 155-164.

Katz,M.L., Kutryb,M.J., Norberg,M., Gao,C.L., White,R.H., Stark,W.S., 1991. Maintenance of opsin density in photoreceptor outer segments of retinoid-deprived rats. Investigative Ophthalmology & Visual Science, 32(7), 1968-1980.

Katz,M.L., Robison,W.G.Jr., 1986. Evidence of cell loss from the rat retina during senescence. Experimental Eye Research, 42(4), 293-304.

Keller,J., Strasburger,H., Cerutti,D.T., Sabel,B.A., 2000. Assessing spatial vision - automated measurement of the contrast-sensitivity function in the hooded rat. Journal of Neuroscience Methods, 97(2), 103-110.

Kolesnikov,A.V., Fan,J., Crouch,R.K., Kefalov,V.J., 2010. Age-related deterioration of rod vision in mice. The Journal of Neuroscience, 30(33), 11222-11231.

Koschak,A., Reimer,D., Huber,I., Grabner,M., Glossmann,H., Engel,J., Striessnig,J., 2001. α1D (Cav1.3) subunits can form L-type Ca^{2+} channels activating at negative voltages. The Journal of Biological Chemistry, 276(25), 22100-22106.

Koulen,P., Kuhn,R., Wässle,H., Brandstätter,J.H., 1999. Modulation of the intracellular calcium concentration in photoreceptor terminals by a presynaptic metabotropic glutamate receptor. Proceedings of the National Academy of Sciences of the United States of America, 96(17), 9909-9914.

Krauter,E.E., Wallace,J.E., Campbell,B.A., 1981. Sensory-motor function in the aging rat. Behavioral and Neural Biology, 31(4), 367-392.

Lin,Y.J., Koretsky,A.P., 1997. Manganese ion enhances T1-weighted MRI during brain activation: an approach to direct imaging of brain function. Magnetic Resonance in Medicine, 38(3), 378-388.

Lindner,M.D., Gribkoff,V.K., 1991. Relationship between performance in the Morris water task, visual acuity, and thermoregulatory function in aged F-344 rats. Behavioural Brain Research, 45(1), 45-55.

Mansour,H., Chamberlain,C.G., Weible,M.W.2nd, Hughes,S., Chu,Y., Chan-Ling,T., 2008. Aging-related changes in astrocytes in the rat retina: imbalance between cell proliferation and cell death reduces astrocyte availability. Aging Cell, 7(4), 526-540.

Marottoli,R.A., de Leon,C.F.M., Glass,T.A., Williams,C.S., Cooney,L.M.Jr., Berkman,L.F., 2000. Consequences of driving cessation: decreased out-of-home activity levels. The Journals of Gerontology, B, Psychological Sciences and Social Sciences, 55(6), S334-S340.

Massof,R.W., Chang,F.W., 1972. A revision of the rat schematic eye. Vision Research, 12(5), 793-796.

Melena,J., Osborne,N.N., 2001. Voltage-dependent calcium channels in the rat retina: involvement in NMDA-stimulated influx of calcium. Experimental Eye Research, 72(4), 393-401.

Meyer,G.E., Salinsky,M.C., 1977. Refraction of the rat: estimation by pattern evoked visual cortical potentials. Vision Research, 17(7), 883-885.

Morgans,C.W., Gaughwin,P., Maleszka,R., 2001. Expression of the α_{1F} calcium channel subunit by photoreceptors in the rat retina. Molecular Vision, 7, 202-209.

Morita,H., Ogino,T., Seo,Y., Fujiki,N., Tanaka,K., Takamata,A., Nakamura,S., Murakami,M., 2002. Detection of hypothalamic activation by manganese ion contrasted T_1-weighted magnetic resonance imaging in rats. Neuroscience Letters, 326(2), 101-104.

Morjaria,B., Voaden,M.J., 1979. The uptake of [^{3}H]2-deoxy glucose by light- and dark-adapted rat retinas *in vivo*. Journal of Neurochemistry, 32, 1881-1883.

Mutti,D.O., Zadnik,K., Johnson,C.A., Howland,H.C., Murphy,C.J., 1992. Retinoscopic measurement of the refractive state of the rat. Vision Research, 32(3), 583-586.

Nachman-Clewner,M., St Jules,R., Townes-Anderson,E., 1999. L-type calcium channels in the photoreceptor ribbon synapse: localization and role in plasticity. The Journal of Comparative Neurology, 415(1), 1-16.

Norris,C.M., Halpain,S., Foster,T.C., 1998. Reversal of age-related alterations in synaptic plasticity by blockade of L-type Ca^{2+} channels. Journal of Neuroscience, 18(9), 3171-3179.

Obin,M., Pike,A., Halbleib,M., Lipman,R., Taylor,A., Bronson,R., 2000. Calorie restriction modulates age-dependent changes in the retinas of Brown Norway rats. Mechanisms of Ageing and Development, 114(2), 133-147.

Olsen,Ø., Kristoffersen,A., Thuen,M., Sandvig,A., Brekken,C., Haraldseth,O., Goa,P.E., 2010. Manganese transport in the rat optic nerve evaluated with spatial- and time-resolved magnetic resonance imaging. Journal of Magnetic Resonance Imaging, 32(3), 551-60.

Owsley,C., Sekuler,R., Siemsen,D., 1983. Contrast sensitivity throughout adulthood. Vision Research, 23(7), 689-699.

Pan,Z.H., Lipton,S.A., 1995. Multiple GABA receptor subtypes mediate inhibition of calcium influx at rat retinal bipolar cell terminals. The Journal of Neuroscience, 15(4), 2668-2679.

Parmer,R., Sheikh,K.H., Dawson,W.W., Toskes,P.P., 1982. A parallel change of taurine and the ERG in the developing rat retina. Comparative Biochemistry and Physiology, C, 72(1), 109-111.

Payne,L.J., Slagle,T.M., Cheeks,L.T., Green,K., 1990. Effect of calcium channel blockers on intraocular pressure. Ophthalmic Research, 22(6), 337-341.

Penn,J.S., Williams,T.P., 1986. Photostasis: Regulation of daily photon-catch by rat retinas in response to various cyclic illuminances. Experimental Eye Research, 43(6), 915-928.

Protti,D.A., Llano,I., 1998. Calcium currents and calcium signaling in rod bipolar cells of rat retinal slices. The Journal of Neuroscience, 18(10), 3715-3724.

Prusky,G.T., Silver,B.D., Tschetter,W.W., Alam,N.M., Douglas,R.M., 2008. Experience-dependent plasticity from eye opening enables lasting, visual cortex-dependent enhancement of motion vision. Journal of Neuroscience, 28(39), 9817-9827.

Prusky,G.T., West,P.W., Douglas,R.M., 2000. Behavioral assessment of visual acuity in mice and rats. Vision Research, 40(16), 2201-2209.

Ragland,D.R., Satariano,W.A., MacLeod,K.E., 2005. Driving cessation and increased depressive symptoms. The Journals of Gerontology, A, Biological Sciences and Medical Sciences, 60(3), 399-403

Rubin,G.S., West,S.K., Muñoz,B., Bandeen-Roche,K., Zeger,S., Schein,O., Fried,L.P., 1997. A comprehensive assessment of visual impairment in a population of older Americans. The SEE Study. Salisbury Eye Evaluation Project. Investigative Ophthalmology & Visual Science, 38(3):557-568.

Samuel,M.A., Zhang,Y., Meister,M., Sanes,J.R., 2011. Age-related alterations in neurons of the mouse retina. The Journal of Neuroscience, 31(44), 16033-16044.

Segarra,J., Santafé,J, Garrido,M., Martínez de Ibarreta,M.J., 1993. The topical application of verapamil and nifedipine lowers intraocular pressure in conscious rabbits. General Pharmacology, 24(5), 1163-1171.

Schmitz,Y., Witkovsky,P., 1997. Dependence of photoreceptor glutamate release on a dihydropyridine-sensitive calcium channel. Neuroscience, 78(4), 1209-1216.

Shah,G.M., Kaufmann,S.H., Poirier,G.G., 1995. Detection of poly(ADP-ribose) polymerase and its apoptosis-specific fragment by a nonisotopic activity-western blot technique. Analytical Biochemistry, 232(2), 251-254.

Silva,A.C., 2012. Using manganese-enhanced MRI to understand BOLD. NeuroImage [in press] doi:10.1016/j.neuroimage.2012.01.008

Silva,A.C., Lee,J.H., Aoki,I., Koretsky,A.P., 2004. Manganese-enhanced magnetic resonance imaging (MEMRI): methodological and practical considerations. NMR in Biomedicine, 17(8), 532-543.

Southall,J.P.C., (1918). *Mirrors, Prisms and Lenses* (pp. 366-375; §129 to §131). New York: The Macmillan Company.

Spear,P.D., 1993. Neural bases of visual deficits during aging. Vision Research, 33(18), 2589-2609.

Srinivasan,V.J., Ko,T.H., Wojtkowski,M., Carvalho,M., Clermont,A., Bursell,S.E., Song,Q.H., Lem,J., Duker,J.S., Schuman,J.S., Fujimoto,J.G., 2006b. Noninvasive volumetric imaging and morphometry of the rodent retina with high-speed, ultrahigh-resolution optical coherence tomography. Investigative Ophthalmology & Visual Science, 47(12), 5522-5528.

Srinivasan,V.J., Wojtkowski,M., Fujimoto,J.G., Duker,J.S., 2006a. *In vivo* measurement of retinal physiology with high-speed ultrahigh-resolution optical coherence tomography. Optics Letters, 31(15), 2308-2310.

Smyth,H.F.J., Carpenter,C.P., Weil,C.S., 1950. The toxicology of the polyethylene glycols. Journal of the American Pharmaceutical Association, 39(6), 349-354.

Tarabova,B., Lacinova,L., Engel,J., 2007. Effects of phenylalkylamines and benzothiazepines on $Ca_v1.3$-mediated Ca^{2+} currents in neonatal mouse inner hair cells. European Journal of Pharmacology, 573(1-3), 39-48.

Thibault,O., Hadley,R., Landfield,P.W., 2001. Elevated postsynaptic $[Ca^{2+}]_i$ and L-type calcium channel activity in aged hippocampal neurons: relationship to impaired synaptic plasticity. The Journal of Neuroscience, 21(24), 9744-9756.

Thibault,O., Landfield,P.W., 1996. Increase in single L-type calcium channels in hippocampal neurons during aging. Science, 272(5264), 1017-1020.

Thibault,O., Porter,N.M., Chen,K.C., Blalock,E.M., Kaminker,P.G., Clodfelter,G.V., Brewer,L.D., Landfield,P.W., 1998. Calcium dysregulation in neuronal aging and Alzheimer's disease: history and new directions. Cell Calcium, 24(5-6), 417-433.

Thomas,B.B., Shi,D., Khine,K., Kim,L.A., Sadda,S.R., 2010. Modulatory influence of stimulus parameters on optokinetic head-tracking response. Neuroscience Letters, 479(2), 92-96.

Tofts,P.S., Porchiac,A., Jin,Y., Roberts,R., Berkowitz,B.A., 2010. Toward clinical application of manganese-enhanced MRI of retinal function. Brain Research Bulletin, 81, 333-338.

Tombaugh,G.C., Rowe,W.B., Rose,G.M., 2005. The slow afterhyperpolarization in hippocampal CA1 neurons covaries with spatial learning ability in aged Fisher 344 rats. The Journal of Neuroscience, 25(10), 2609-2616.

van Alphen,B., Winkelman,B.H., Frens,M.A., 2009. Age- and sex-related differences in contrast sensitivity in C57BL/6 mice. Investigative Ophthalmology & Visual Science, 50(5), 2451-2458.

Veng,L.M., Browning,M.D., 2002. Regionally selective alterations in expression of the α_{1D} subunit ($Ca_v1.3$) of L-type calcium channels in the hippocampus of aged rats. Molecular Brain Research, 107(2), 120-127.

Veng,L.M., Mesches,M.H., Browning,M.D., 2003. Age-related working memory impairment is correlated with increases in the L-type calcium channel protein α_{1D} subunit ($Ca_v1.3$) in area CA1 of the hippocampus and both are ameliorated by chronic nimodipine treatment. Molecular Brain Research, 110(2), 193-202.

Vinores,S.A., McGehee,R., Lee,A., Gadegbeku,C., Campochiaro,P.A., 1990. Ultrastructural localization of blood-retinal barrier breakdown in diabetic and galactosemic rats. The Journal of Histochemistry and Cytochemistry, 38(9), 1341-1352.

Watanabe,T., Michaelis,T., Frahm,J., 2001. Mapping of retinal projections in the living rat using high-resolution 3D gradient-echo MRI with Mn^{2+}-induced contrast. Magnetic Resonance in Medicine, 46, 424-429.

Westenbroek,R.E., Babcock,D.F., 1999. Discrete regional distributions suggest diverse functional roles of calcium channel α1 subunits in sperm. Developmental Biology, 207(2), 457-469.

Whitlock,M.C., 2005. Combining probability from independent tests: the weighted Z-method is superior to Fisher's approach. Journal of Evolutionary Biology, 18(5), 1368–1373.

Wiesenfeld,Z., Branchek,T., 1976. Refractive state and visual acuity in the hooded rat. Vision Research, 16(8):823-827.

Wright,C.E., Williams,D.E., Drasdo,N., Harding,G.F., 1985. The influence of age on the electroretinogram and visual evoked potential. Documenta Ophthalmologica, 59(4), 365-384.

Xu,H.P., Zhao,J.W., Yang,X.L., 2002. Expression of voltage-dependent calcium channel subunits in the rat retina. Neuroscience Letters, 329(3), 297-300.

Xu,W., Lipscombe,D., 2001. Neuronal $Ca_v1.3\alpha_1$ L-type channels activate at relatively hyperpolarized membrane potentials and are incompletely inhibited by dihydropyridines. The Journal of Neuroscience, 21(16), 5944-5951.

Yau,K.W., 1994. Phototransduction mechanism in retinal rods and cones. The Friedenwald Lecture. Investigative Ophthalmology & Visual Science, 35(1), 9-32.

Yu,X., Wadghiri,Y.Z., Sanes,D.H., Turnbull,D.H., 2005. In vivo auditory brain mapping in mice with Mn-enhanced MRI. Nature Neuroscience, 8(7), 961-968.

ABSTRACT

PREDICTING VISION LOSS IN HEALTHY AGING WITH MANGANESE-ENHANCED MRI OF THE RAT EYE

by

DAVID BISSIG

May 2014

Advisor: Dr. Bruce A. Berkowitz

Major: Anatomy and Cell Biology

Degree: Doctor of Philosophy

In healthy aging, visual function declines throughout adulthood. Age-related changes in neuronal ion homeostasis — specifically, increased Ca^{2+} influx through L-type voltage gated calcium channels (L-VGCCs) — are believed to contribute to certain functional declines, but this possibility has not yet been tested in the neural retina. In young, mid- and old adult Long-Evans rats, we compared visual function (optokinetic tracking), as well as retinal physiology and eye morphology (Mn^{2+}-enhanced MRI (MEMRI), which uses neuronal Mn^{2+} uptake as a marker of Ca^{2+} influx). We documented significant age-related decreases in visual performance and increases in retinal ion influx. We confirmed that Mn^{2+} uptake was regulated by L-VGCC using systemic and topical application of the L-VGCC antagonist nifedipine, and discovered an age-related change in sensitivity to L-VGCC blocker diltiazem. Based on Western blot studies, we find this sensitivity change to be consistent with the age-dependant appearance of drug-insensitive L-VGCC isoforms. Longitudinally, rats starting the study with relatively high retinal Mn^{2+} uptake, compared to other cohort members, experienced significantly greater declines in contrast sensitivity in the ~4.5 mo following MRI. Independent of that relationship, rats starting the study with relatively large eyes experienced significantly greater declines in contrast

sensitivity. The latter finding suggests that particularly rapid juvenile or young-adult growth is a risk factor for particularly rapid senescence. Longitudinally, we found no evidence of retinal volume loss, and found that changes in retinal volume were not correlated with changes in visual function — suggesting that age-related vision declines cannot be explained by neuron loss. In summary, our longitudinal studies identify two previously-unknown risk factors for age-related vision declines: rapid eye growth in early life, and age-related changes in L-VGCC-dependent retinal ion physiology.

AUTOBIOGRAPHICAL STATEMENT

DAVID BISSIG
7327 Scott Hall, 540 E. Canfield
Detroit, MI 48201
dbissig@med.wayne.edu

Education

2006-present MD/PhD Program (expected data of graduation: May 2014)
Wayne State University School of Medicine
Detroit, MI

2001-2005 Bachelor of Science, Psychology
Bachelor of Science, Philosophy
University of Michigan
Ann Arbor, MI

Honors and Awards

National Institute of Aging F30 grant (score:10, submission Dec. 2009), AG034752
NeuroImage Editor's Choice Award (for Bissig & Berkowitz, NeuroImage, 44(3)), 2009
Board of Governors Medical Scholarship, Wayne State University, 2006-2008

First (and co-First) Author Publications

Chui,T.Y.P., **Bissig,D**., Berkowitz,B.A., Akula,J.D., 2012. Refractive development in the "ROP Rat". Journal of Ophthalmology, doi:10.1155/2012/956705. PMCID: PMC3307090

Bissig,D., Berkowitz,B.A., 2011. Same-session functional assessment of rat retina and brain with manganese-enhanced MRI, Neuroimage, 58(3), 749-760. PMID: 21749922

Bissig, D., Berkowitz, B.A., 2009. Manganese-enhanced MRI of layer-specific activity in the visual cortex from awake and free-moving rats. NeuroImage, 44(3), 627-637. PMCID: PMC2642584

Bissig,D., Lustig,C., 2007. Who benefits from memory training? Psychological Science, 18(8):720-726. PMID: 17680944